

**Generation and Characterization of Ultrafine Particles
in Laboratory Studies and Their Mass Deposition at the
Air-Liquid Interface**

Cumulative Dissertation

To attain the academic degree

doctor rerum naturalium (Dr. rer. nat.)

from the Faculty of Mathematics and Natural Science

of the University of Rostock

submitted by

Anusmita Das

Born on August 26, 1994, in Guwahati, India

Rostock, May 2025

Reviewer:

Prof. Dr. Ralf Zimmermann, University of Rostock, Institute of Chemistry

Prof. Dr. Konstantinos Eleftheriadis, Ethniko Kentro Ereunas Physikou Epistemon
Demokritos, Athens, GR

Year of submission: 2025

Year of defense: 2025

মা-দেউতাৰ পবিত্ৰ সোঁৱৰণত - একাজলি শ্ৰদ্ধাঞ্জলি।

CONTRIBUTIONS TO PEER-REVIEWED PUBLICATIONS

FIRST-AUTHORSHIPS

Anusmita Das is the first author of the following manuscripts, which have been published in peer-reviewed journals. The specific contributions of Anusmita Das to each manuscript are detailed below.

GENERATION, CHARACTERIZATION, AND TOXICOLOGICAL ASSESSMENT OF REFERENCE ULTRAFINE SOOT PARTICLES WITH DIFFERENT ORGANIC CONTENT FOR INHALATION TOXICOLOGICAL STUDIES

Das A, Pantzke J, Jeong S, Hartner E, Zimmermann E J, Gawlitta N, Offer S, Shukla D, Huber A, Rastak N, Meščeriakovas A, Ivleva N P, Kuhn E, Binder S, Gröger T, Oeder S, Delaval M, Czech H, Sippula O, Schnelle-Kreis J, Di Bucchianico S, Sklorz M, Zimmermann R.

Journal: Science of the Total Environment (*Impact factor: 8.2, 2024*)

Year: 2024

DOI: 10.1016/j.scitotenv.2024.175727

Anusmita Das designed the study, generated the two ultrafine particle (UFP) types, and conducted comprehensive physical and chemical characterization of the aerosol particles. This included using aerosol online characterization instruments to measure parameters such as size distribution, geometric mean diameter, mass concentration, and equivalent carbon concentration. She also performed particle-phase sampling and quantified polycyclic aromatic hydrocarbons (PAHs) using thermal desorption gas chromatography-mass spectrometry (TD-GC-MS). Additionally, she was responsible for evaluating and interpreting aerosol data and drafting and revising the manuscript.

INCREASED PARTICLE MASS DEPOSITION ON LUNG TISSUE DUE TO INDUSTRIAL AND WASTE-BURNING ACTIVITIES

Das A, Karg E W, Ferron G A, Schnelle-Kreis J, Mandariya A K, Habib G, Wiedensohler A, Pöhlker M L, Zimmermann R, Ahlawat A.

Journal: Environmental International (*Impact factor: 10.3, 2024*)

Year: 2025

DOI: *Under Review*

Anusmita Das contributed to the investigation and analysis of the data, including conceptualizing the manuscript, performing statistical analysis, interpreting the data, and producing all illustrations.

DETERMINATION OF ULTRAFINE PARTICLE NUMBER AND MASS DEPOSITION AT THE AIR-LIQUID INTERFACE IN AN *IN VITRO* AEROSOL EXPOSURE SYSTEM

Das A, Delaval M, Ihalainen M, Schnelle-Kreis J, Huber A, Zimmermann E J, Di Bucchianico S, Sippula O, Czech H, Sklorz M, Zimmermann R.

Journal: Journal of Aerosol Science (*Impact factor: 3.9, 2024*)

Year: 2025

DOI: Submitted

Anusmita Das generated ultrafine particles (UFP) from two different sources: the miniCAST and the spark discharge generator. She collected, quantified, and analyzed the deposited mass of UFP at the air-liquid interface (ALI) in the Automated Exposure Station. Moreover, she evaluated and interpreted the data, contributing to the drafting and revision of the manuscript.

CO-AUTHORSHIP

TOXICOLOGICAL EFFECTS OF LONG-TERM CONTINUOUS EXPOSURE TO AMBIENT AIR ON HUMAN BRONCHIAL EPITHELIAL CALU-3 CELLS EXPOSED AT THE AIR-LIQUID INTERFACE

E, Zimmermann E J, **Das A**, Huber A, Gawlitta N, Kuhn E, Schlager C, Gutmann B, Krebs T, Schnelle-Kreis J, Delaval M, Zimmermann R.

Journal: Environmental Research (*Impact factor: 7.7, 2024*)

Year: 2025

DOI: 10.1016/j.envres.2025.120759

Anusmita Das was responsible for setting up the online aerosol characterization instruments and conducting data interpretation and analysis. She also collected particulate-phase samples and quantified polycyclic aromatic hydrocarbons (PAHs) using thermal desorption gas chromatography-mass spectrometry (TD-GC-MS). She was also involved in writing and revising the manuscript.

ACKNOWLEDGEMENTS

This work would not have been possible without the support and encouragement of many incredible people. I want to thank my supervisors, coworkers, collaborators, friends, and family for their unwavering support throughout this journey.

First and foremost, I want to express my deepest gratitude to **Prof. Dr. Ralf Zimmermann** for allowing me to join his interdisciplinary team and pursue my PhD.

To my supervisor, **Martin Sklorz**, thank you for your constant guidance in and out of the lab. Your challenges pushed me to think critically, set up experiments independently and grow as a scientist. I am still in awe of the depth of your knowledge, and I feel incredibly fortunate to have had the opportunity to learn from you. And, of course, thank you for bringing the most delicious *Nussecke*! To **Jürgen Schnelle-Kreis**, I am deeply grateful for your insightful discussions, unwavering support, and guidance during the most challenging phases of this journey. Thank you for your patience in teaching me DTD-GC-MS and for making brainstorming sessions productive and enjoyable. To **Hendryk Czech**, I cannot thank you enough for your incredible support during the most challenging moments. Your willingness to discuss science anytime and help with last-minute revisions was invaluable.

Thank you to all my colleagues at **CMA** for the motivation, teamwork, project discussions, and opportunities to grow personally and scientifically. A special thank you to **Anja** and **Mathilde** for consistently bringing warmth, care, and support and for their assistance with the Automated Exposure System. To **Sandra** and **Nadine**, thank you for sharing countless moments of joy, including singing all the Taylor Swift songs with me. To **Svenja**, **Seongho**, **Deeksha**, **Lukas**, and **Elias**, thank you for always being there for a chat, offering support, and being the best colleagues, complete with hugs! I want to thank **Tom** and **Marina** for their incredible dedication during the challenging CMA closing period. Your efforts in maintaining the office's essence and ensuring it continued functioning as one were commendable. Thank you for guiding me through the labyrinth of bureaucracy with patience and care, especially when I struggled to navigate it independently. In addition to all my colleagues at the JMSC, I sincerely thank all project partners, including BAY-UFP, ULTHRAS, aeroHEALTH and other funding bodies, for their support, expertise, and enjoyable collaborations.

To my best friend, **Rakhi**, thank you for always being there to listen, whether I was crying, frustrated, or ranting about this journey. Your support, belief in me, and ability to laugh at the silliest things helped me forget the hardships and made this journey much brighter. To **Atrayee** and **Angshuman**, thank you for bringing me food when I was too absorbed in the lab and letting me crash at your place when experiments didn't go as planned. Your kindness, the moments of relaxation, and the movie marathons in Munich made me feel at home, even though I was far from home. It was indeed a blessing during this journey.

To my biggest supporter, **Roberto**, your presence made everything better. You helped me pick myself up and come back stronger after harsh draft comments, failed experiments, and moments when I cried like a baby. Your love, support and care, whether through cooking, long walks, drives, pizza dates, or motivating me to go to the gym, kept me going. You were my rock through it all, and I couldn't have made it through this journey without you by my side.

I owe my deepest gratitude to my family. This journey would not have been possible without your unwavering support and love.

To my **brother**, thank you for calling me every day and checking in, even when words couldn't fully express what I was going through. Your consistent presence and support, in your unique ways, have meant more to me than you'll ever know. I am genuinely grateful for the bond we share and the love you've given me, no matter the distance.

To my dear **grandma**, thank you for always being there for me and offering your love and support through every step of this journey. Your constant encouragement and belief in me have been a source of strength. To **Bhaitee Mama** and **Baban Mama**, thank you for being my pillars of support from Barpeta, especially when I needed someone who truly understood my emotions. Your patience and listening willingness have provided comfort and strength throughout this journey. I always felt I could turn to you both, no matter the circumstance, and that made all the difference. Bhaitee Mama, I am particularly grateful for your continued help with math, even now! Your dedication to guiding me, both academically and emotionally, has been invaluable. I am truly fortunate to have such caring and supportive uncles who have always been there for me, and I will be forever grateful for everything you've done.

Mum and Dad, thank you for everything you did to get me where I am today. Your endless love and unconditional support have shaped me in ways words cannot express. Although you are no longer with me, your presence and guidance inspire and drive me daily.

ZUSAMMENFASSUNG

Luftverschmutzung, insbesondere Feinstaub, wird mit erhöhter Morbidität und Mortalität in Verbindung gebracht. Der Beitrag von ultrafeinen Partikeln (UFP, $D_p \leq 100$ nm) zur globalen Krankheitslast, der *burden of disease*, und die Wirkmechanismen sind jedoch wenig erforscht. Es ist unklar, ob ihre physikalischen Eigenschaften in erster Linie für die Toxizität von UFP verantwortlich sind oder ob sie als Träger für biologisch reaktive Chemikalien dienen, die für schädliche biologische Wirkungen verantwortlich sind. Zur Beantwortung dieser Fragen sind robuste Methoden zur Erzeugung und Kontrolle von UFP erforderlich, die eine präzise Beeinflussung ihrer physikalischen und chemischen Eigenschaften ermöglichen.

Methoden zur Zellexposition an der Luft-Flüssigkeits-Grenzfläche (*air-liquid-interface*, ALI) sind wichtige Instrumente für die möglichst realistische Bewertung der Toxizität von Aerosolen aus der Luft und von technisch hergestellten Nanomaterialien *in vitro*. Diese Systeme bieten verbesserte Möglichkeiten, Kapazitäten und Flexibilität, indem sie Aerosole direkt auf lebende Zellkulturen aufbringen. Die Bestimmung der genauen Aerosoldosis oder -abscheidung auf den Zellkulturen bleibt jedoch eine Herausforderung, insbesondere bei UFP.

In dieser Studie wurden zwei UFP aus einem Rußpartikelgenerator mit ähnlicher elementaren Kohlenstoffstruktur und physikalischen Eigenschaften, aber unterschiedlicher chemischer Zusammensetzung (organische Belastung) hergestellt und charakterisiert. Menschliche Zellen aus dem Alveolarepithel (A549) wurden gegen UFP unter ALI-Bedingungen exponiert, um ihre toxikologischen Auswirkungen zu bewerten. Die Ergebnisse zeigten, dass beide UFP, unabhängig von der organischen Belastung, ähnliche Reaktionen auf die Stoffwechselaktivität auslösten. Ein höherer Gehalt an polyzyklischen aromatischen Kohlenwasserstoffen (PAK) korrelierte jedoch mit einem erhöhten Xenobiotika-Stoffwechsel, was die Rolle der chemischen Zusammensetzung bei biologischen Reaktionen unterstreicht. Dieser Ansatz ermöglichte eine präzise Modifizierung der chemischen Eigenschaften von UFP als Referenzruß bei gleichzeitiger Beibehaltung der physikalischen Merkmale, so dass eine reproduzierbare toxikologische Bewertungen erleichtert wird.

Zur Bewertung der Massenabscheidung von UFP im ALI-System wurden Ruß-UFP mit hoher chemischer Beladung und Kupfer-UFP, die durch Funkenentladung erzeugt wurden, verwendet. Die physikalischen Eigenschaften beider UFP wurden eng aneinander angepasst, um ihr Ablagerungsverhalten zu untersuchen. Die Ergebnisse zeigten, dass beide Arten von UFP für die Bewertung der Abscheidungseffizienz in ALI-Systemen geeignet sind. Darüber hinaus übertraf die gemessene UFP-Massenabscheidung die von herkömmlichen Modellen vorhergesagten Werte.

Zusammenfassend lässt sich sagen, dass in dieser Dissertation eine robuste Methode zur Erzeugung von UFP mit kontrollierten physikalischen und chemischen Eigenschaften entwickelt wurde, um deren Rolle in der *in-vitro*-Toxizität zu untersuchen. Darüber hinaus verbessert sie das Verständnis über die Massenabscheidung von UFP in ALI-Systemen und trägt damit zu einer verbesserten Expositionsbewertung in toxikologischen Studien bei.

ABSTRACT

Air pollution, particularly particulate matter, is linked to increased morbidity and mortality. However, the contribution of ultrafine particles (UFP, $D_p \leq 100$ nm) to the global disease burden remains uncertain. It is unclear to what extent their physical characteristics primarily drive UFP toxicity or if they serve as carriers for biologically reactive chemicals responsible for adverse biological effects. Addressing these questions requires robust methods for generating and controlling UFP, allowing precise manipulation of their physical and chemical properties.

Air-Liquid Interface (ALI) cell exposure systems are critical tools for the most realistic assessment of the toxicity of airborne aerosols and engineered nanomaterials *in vitro*. These systems offer enhanced capability, capacity, and flexibility by directly depositing aerosols onto living cell cultures. However, determining the precise aerosol dose or deposition remains challenging, particularly for UFP.

In this study, two soot UFPs with similar elemental carbon cores and physical properties but differing in chemical composition (organic load) were generated and characterized. The approach enabled precise modification of the chemical properties of reference soot UFP while maintaining consistent physical characteristics, facilitating reproducible toxicological assessments. To assess their toxicological effects, human alveolar epithelial cells (A549) were exposed to these UFP under ALI conditions. Results indicated that UFP, regardless of organic load, induced similar metabolic activity responses. However, higher polycyclic aromatic hydrocarbon (PAHs) content correlated with increased xenobiotic metabolism, highlighting the role of chemical composition in biological responses.

Soot UFP with high chemical loads and copper UFP generated via spark discharge were utilized to evaluate UFP mass deposition in the ALI system. The physical properties of both UFP were closely matched to investigate their deposition behavior. Findings revealed that both types of UFPs are suitable for assessing deposition efficiency in ALI systems. Moreover, measured UFP mass deposition exceeded values predicted by conventional models.

This dissertation presents a robust method for generating UFP aerosols with controlled physical and chemical properties to investigate their role in *in vitro* toxicity. It also provides insights into UFP mass deposition in ALI systems, contributing to improved exposure assessment in toxicological studies.

TABLE OF CONTENTS

Contribution to peer-reviewed publications.....	IV
Acknowledgements.....	VI
Zusammenfassung.....	VIII
Abstract.....	IX
Table of contents.....	X
Abbreviations.....	XII
List of figures.....	XIV
1 Introduction.....	1
1.1 Aerosols in the atmosphere	1
1.2 Ultrafine particles (UFP)	2
1.2.2 UFP and Adverse Health Effects.....	4
1.2.2 Challenges associated with monitoring and characterizing UFP.....	6
1.3 Controlled Laboratory Generation of UFP.....	7
1.3.1 Mimicking Atmospheric Soot and Metal Emissions.....	7
1.4 Exposures to UFP.....	10
1.4.1 Air-Liquid Interface (ALI) Exposure Systems.....	11
2 Scope of the Thesis.....	13
3 Methodology.....	14
3.1 Laboratory generation of Soot Aerosol: CAST.....	14
3.2 Catalytic stripping.....	14
3.3 Charcoal Denuder.....	15
3.4 Laboratory Generation of Metal Aerosol.....	16
3.5 Experimental setups.....	16
3.5.1 Soot UFP.....	16
3.5.2 Copper UFP.....	18
3.6 Aerosol Online Characterization.....	19
3.7 Aerosol Offline Characterization.....	20
3.7.1 Particle-associated Sampling.....	20
3.7.2 Analyzes of Particle-associated PAHs in UFP.....	21
	X

3.7.3 Analyzes of copper UFP.....	22
3.7.4 Morphology of UFP.....	22
3.8 Analyzes for the Mass deposition of the UFP.....	23
4 Results and Discussions.....	24
4.1 Characterization of Laboratory-generated soot UFP.....	24
4.1.1 Online Characterization.....	24
4.1.2 Offline Characterization.....	26
4.1.3 Toxicological effects.....	28
4.1.4 Indicators of UFP Toxicity.....	30
4.2 Characterization of Laboratory-generated Copper UFP.....	30
4.2.1 Online Characterization.....	30
4.2.2 Offline Characterization.....	31
4.3 Toward Reliable UFP Models for Toxicological Assessment.....	31
4.4 Dosimetry in ALI Systems.....	32
4.4.1 Measured Mass Deposition.....	33
4.4.2 Estimated Mass Deposition.....	34
4.4.3 Comparing ALLI Experiments with Human Exposure Models.....	36
4.5 Endpoints/ Analytes for integrating Environmental and ALI Monitoring.....	36
5 Summary and Outlook.....	38
6 References.....	40
7 Appendix.....	53
Curriculum Vitae.....	53
Contribution to conferences.....	54

ABBREVIATIONS

AAE	absorption Ångström exponent
AAS	atomic absorption spectrometer
AES	automated exposure station
ALI	air-liquid interface
BC	black carbon
CCN	cloud condensation nuclei
CFD	computational fluid dynamics
CS	catalytic stripper
CPC	condensation particle counter
Cu-UFP	copper UFP
DMA	differential mobility analyzer
DTD	direct thermal desorption
eBC	equivalent black carbon
EBC	exhaled breath condensate
EC	elemental carbon
ESI-FTICRMS	electron spray ionization-fourier-transform ion cyclotron resonance mass spectrometry
GCMS	gas chromatography-mass spectrometry
GMD_{mob}	geometric mean mobility diameter
GSH	glutathione
GSSG	oxidized glutathione
LA	laser ablation
LDH	lactate dehydrogenase
LOQ	limits of quantification
MAC	mass absorption cross-section
MDA	malondialdehyde
miniCAST	mini combustion aerosol standard
NP	nanoparticles
NPF	new particle formation
OC	organic carbon
PAHs	polycyclic aromatic hydrocarbons
PFA	perfluoroalkoxy
PM	particulate matter
PNC	particle number concentration

PNSD	particle number size distribution
POA	primary organic aerosol
PTD	porous tube diluter
QFF	quartz fiber filters
ROS	reactive oxygen species
SOA	secondary organic aerosol
SDG	spark discharge generators
SIM	single-ion monitoring
SMPS	scanning Mobility Particle sizer
SVOCs	semi-volatile organic compounds
TD-GC × GC-TOFMS	thermal desorption comprehensive two-dimensional gas chromatography hyphenated with time-of-flight mass spectrometry
TEM	transmission electron microscopy
TEOM	tapered element oscillating microbalance
Ultrafine particles	UFP
UFP-H	UFP soot with high organic load
UFP-L	UFP soot with low organic load
VOCs	volatile organic carbon

LIST OF FIGURES

Figure 1. Particle-size distribution of atmospheric PM.....	1
Figure 2. Sources of UFP and the associated environmental processes.....	3
Figure 3. UFP exhibiting the ' <i>Trojan Horse Mechanism</i> '.....	5
Figure 4. Formation of soot.....	7
Figure 5. States of particle formation in SDG.....	8
Figure 6. Air- Liquid Exposure.....	11
Figure 7. Formation of soot in a CAST.....	14
Figure 8. Catalytic stripper.....	15
Figure 9. Experimental set-up of UFP soot generation.....	17
Figure 10. Experiment set-up of copper-UFP.....	18
Figure 11. A simplified diagram of a gas chromatograph-mass spectrometer.....	21
Figure 12. Size distribution of UFP soot.....	24
Figure 13. Chemical characterization of UFP soot by DTD-GC × GC-TOFMS.....	26
Figure 14. Targeted quantification of UFP soot by DTD-GMS.....	27
Figure 15. TEM imaging of UFP soot.....	28
Figure 16. Cytotoxicity and % cell viability.....	28
Figure 17. Oxidative stress-associated potential.....	29
Figure 18. Induction of the resorufin intensity.....	29
Figure 19. Percentage of DNA in tail and Fpg sites (% DNA in tail).....	30
Figure 20. Size distribution of copper-UFP.....	31
Figure 21. Deposited PAH from UFP-H in the ALI insert.....	33
Figure 22. Deposited Cu-UFP in the ALI insert.....	34

1 INTRODUCTION

1.1 AEROSOLS IN THE ATMOSPHERE

Particles of liquids, such as water, and solids, such as dust, suspended in the atmosphere constitute atmospheric aerosols. There are numerous kinds of aerosol sources, but they can be primarily divided into two categories: natural and anthropogenic. Natural sources include sea salt spray, wind-borne dust, volcanic eruptions, forest fires, and biogenic aerosols (from living organisms). Meanwhile, anthropogenic sources include road transport, industrial emissions, biomass burning, and waste burning. Due to the variability in different sources and formation mechanisms, aerosol particles can range in size from a few nanometers to several tens of micrometers.

The ambient aerosol particle size distribution results from direct emissions, in situ particle formation, interactions among particles or between particles and gaseous compounds, and deposition processes. Nucleation-mode particles (3 to 20 nm) freshly form via the nucleation of gaseous molecules and ions and are later grown by coagulating with other nucleated particles and condensing other gaseous molecules¹. Aitken-mode (20 to 100 nm) and accumulation-mode (100 to 1000 nm) particles are commonly linked to primary emissions from combustion sources and the condensation of secondary materials². Coarse-mode particles (≥ 1000 nm) primarily originate from mechanical processes like aerodynamic resuspension and surface abrasion. Figure 1 shows a typical particle size distribution. Due to their high diffusivity, nucleation-mode particles are rapidly removed through coagulation³. However, during new particle formation (NPF) events, they can grow into the Aitken mode. Aitken-mode particles, in turn, can contribute to forming

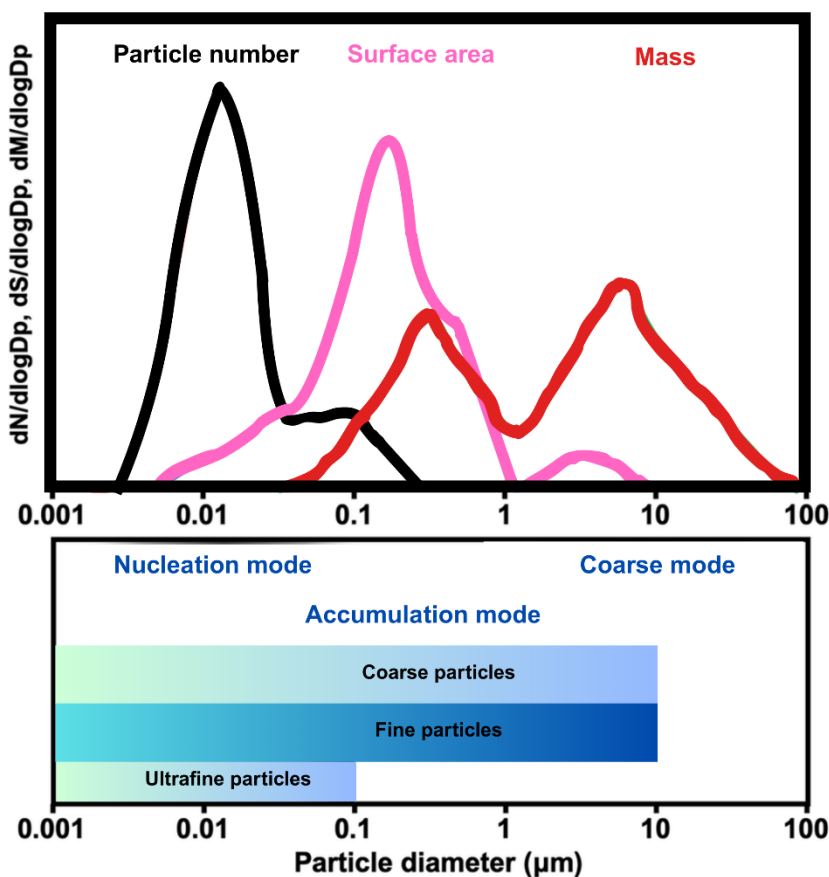


Figure 1. Particle-size distribution of atmospheric particulate matter (PM). This schematic illustrates a typical ambient particle-size distribution for number concentration, surface area concentration, and mass concentration, plotted as $dN/d\text{Log}D_p$ (particle number per cubic millimeter), $dS/d\text{Log}D_p$ (particle surface area per cubic millimeter), and $dM/d\text{Log}D_p$ (particle mass per cubic millimeter), respectively. Vertical scaling is adjusted independently for each distribution. The distribution highlights three primary aerosol modes: nucleation, accumulation, and coarse.

accumulation-mode particles through coagulation and condensation⁴. Accumulation-mode particles persist in the atmosphere for extended periods due to their low gravitational settling velocities and low coagulation rates⁵. In urban areas, the number particle size distribution is typically dominated by nucleation and Aitken mode particles due to the abundance of primary emission sources such as soot from power plants, traffic, and industrial activities⁶. The contribution of anthropogenic non-combustion nucleation and Aitken mode particles is also increasing in the urban scenario, with sources like brake pad wear, tire abrasions, friction between wheels and roads/rails, and catenary sparking⁷.

Aerosol particles can be emitted directly into the atmosphere (primary aerosol) or formed when emitted gases undergo complex aging processes and condense into particles (secondary aerosol). Primary aerosols are directly generated from the sources without undergoing significant chemical transformation processes in the atmosphere. They typically undergo the bulk-to-particle (b-to-p) conversion process, which leads to their formation. Sea spray, soil and rock debris (mineral dust), biogenic aerosols, forest fires, and volcanic debris constitute primary aerosols from natural surface sources⁵. Atmospheric aerosols also constitute a significant portion of primary aerosols from anthropogenic sources, such as diesel emissions and road dust. However, primary organic aerosols (POA) can undergo further aging in the atmosphere through heterogeneous oxidation (reaction with gas-phase oxidants, such as OH, O₃, or NO₃) or within-particle chemical reactions, forming aged POA⁸. This aging process alters their chemical composition, volatility, and optical properties, making them more similar to secondary organic aerosols (SOA). Aged-POA can be a significant oxidized organic aerosol mass source and influence cloud condensation nuclei (CCN) properties. Secondary aerosols are generated directly in the atmosphere through chemical and physical processes, converting gases to particles (g-to-p). They are mainly composed of tiny particles or liquid droplets formed by the condensation of gaseous precursors. Anthropogenic SOA comprise sulfates and nitrates formed through the condensation of sulfur- and nitrogen-containing gases and carbonaceous molecules^{9,10}. At the same time, urban and industrial transportation emissions, which release SO₂, NO_x, and volatile organic carbon (VOCs), are sources of anthropogenic secondary aerosols. Approximately 90% of global VOCs and 50% of SOA emissions are biogenic. Secondary aerosols significantly impact the global aerosol budget due to their comparably high number concentration at locations worldwide and the substantial contribution from anthropogenic gaseous emissions.

1.2 ULTRAFINE PARTICLES (UFP)

Ultrafine particles (UFP; Particulate matter (PM_{0.1})) are particles with an aerodynamic diameter of 0.1 μm or smaller. Many natural sources, such as volcanic activities, forest fires, and sea spray, produce UFP, while anthropogenic sources are from combustion processes, such as emissions from transport, industries, power plants, trash burning, cigarette smoking, and biomass burning^{11–13}. Atmospheric aerosol in urban environments constitutes a significant portion of UFP as both singlet and aggregated particles¹⁴. The effect of UFP and its interaction with other climate system components is complex. UFP can reflect, scatter and absorb solar radiation¹⁵. Nucleation significantly contributes to the worldwide tropospheric particle number concentration and is an essential factor in the CCN budget^{11,16}. Nucleation processes also contribute to an increase in aerosol radiative forcing¹⁷. Radiation-dominated NPF events are directly influenced by solar radiation, affecting the concentration of UFP in the atmosphere. As the Earth's temperature rises, extreme weather events will exacerbate various plant stressors, affecting the NPF events by influencing the precursor emissions¹⁸. UFP also

impacts cloud properties, resulting in modified rainfall patterns and disparate precipitation. This could increase the frequency and intensity of extreme weather events, leading to significant losses from natural calamities¹⁹.

Particle concentrations can be expressed in terms of surface area, particle number, or mass, encompassing a wide range of particle types and related properties. Number and mass concentration are the most commonly used metrics to describe aerosols or particulate matter (PM). Mass concentrations commonly characterize fine PM (PM_{2.5}; aerodynamic diameter ≤ 2.5 μm) and coarse particulate matter (PM₁₀; aerodynamic diameter ≤ 10 μm). UFP is usually measured by its number concentrations, for it has a negligible mass but is a dominant contributor to the total number of particles in the atmosphere¹³. However, many health-related studies of UFP use particle surface area as their metric to associate UFP and health effects^{20–22}.

The rapid conversion of UFP, particularly of their smallest fractions (<20 nm), is a significant property. These particles exhibit Brownian motion, moving through diffusion along concentration gradients. In areas with high particle number concentrations near emission sources, UFP frequently collides with nearby particles, leading to coagulation and accumulation into larger particles or deposition onto available surfaces¹¹ and making the fraction of UFP <20 nm have very short atmospheric lifetimes. This usually lasts approximately a few hours, and their concentrations rapidly decline as the distance from the emission source increases²³. Processes like coagulation and condensation of volatile organic compounds (VOCs) and semi-volatile organic compounds (SVOCs) on the surface of UFP are other contributors to particle growth²⁴. These processes vary from those that occur in larger particles, as these undergo faster changes in number, size, shape, surface area and volume^{25,26}. After formation, the UFP can stay suspended in the air longer than larger particles²⁷ before being removed through dry or wet deposition processes²⁸.

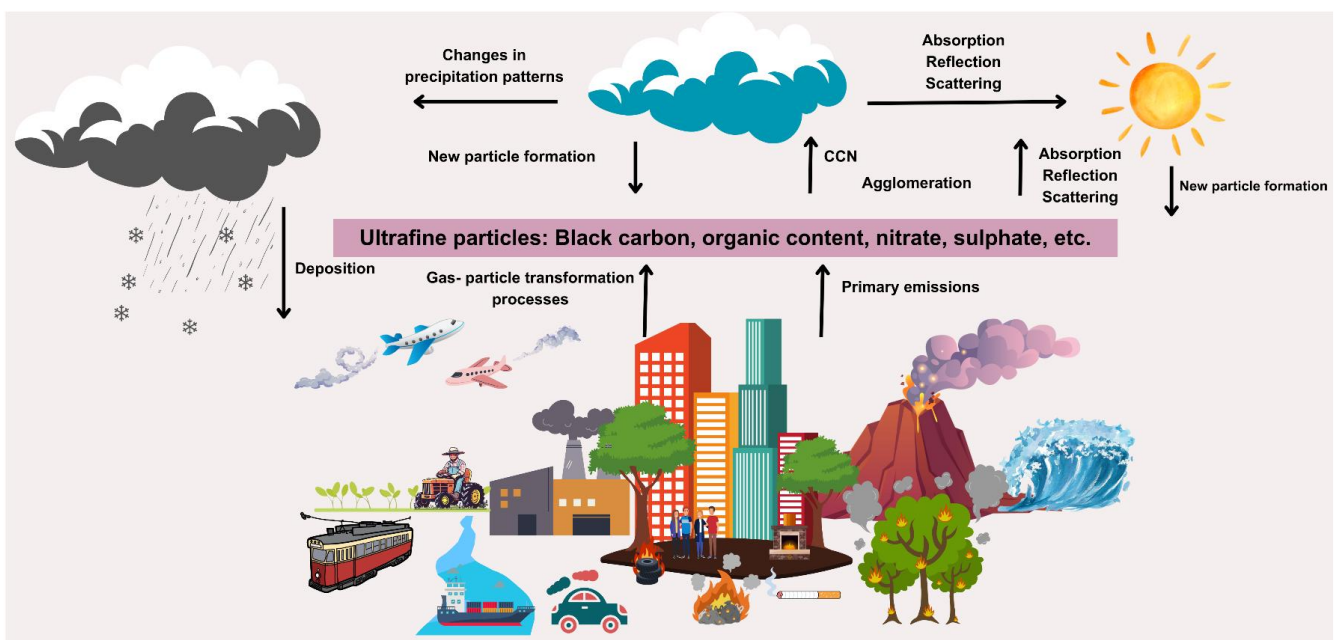


Figure 2 . Sources, environmental processes, and climate interactions of UFP originating from a variety of natural and anthropogenic sources

Elemental carbon (EC), organic compounds, nitrate ions, sulfates and trace metal oxides constitute most UFP²⁹. The EC and organic compounds contain 80-90% of UFP, black carbon (BC), and organic carbon (OC)³⁰. These can serve as nuclei, absorbing other chemical species³¹. The mass associated with UFP comprises carbonaceous material with a minor fraction contributed by inorganic ions, highlighting combustion processes as the primary source of UFP in the ambient environment³⁰. BC is a primary aerosol product usually formed during the incomplete combustion of biomass or fossil fuels from anthropogenic activities like industrial and automobile emissions, biomass and solid waste burning³²⁻³⁴. Due to its physicochemical characteristics, BC can serve as a substrate for various chemical reactions and absorb both primary and secondary contaminants, which may be deposited on the skin or inhaled, ultimately reaching the lungs and affecting respiratory tissues. Polycyclic aromatic hydrocarbons (PAHs) are among the most significant organic components of PM³⁵. These are compounds composed solely of carbon and hydrogen atoms arranged in structures ranging from simple rings to more complex configurations. PAHs are primarily emitted into the atmosphere during combustion processes. They are considered hazardous, persistent organic pollutants that harm the environment and human health, as they are often mutagenic, carcinogenic, and/or detrimental to reproduction^{36,37}. Additionally, the PAHs can initiate several atmospheric physical and chemical reactions that produce PAHs derivatives, such as N-PAHs and O-PAHs³⁸. Their concentration in ambient aerosol can be very low, but their toxicity is often higher than that of their parent compounds³⁹. Sulfates and nitrates can be found in the ambient UFP fraction as pure solid or aqueous particles or as a surface layer on other solids, like carbon particles or ash^{40,41}. They can act as nuclei for the absorption of various chemical species, potentially causing harm³¹. In the finer fraction of PM, numerous recognized sources of metals, such as Na, Ca, Al, K, Fe, Se, and Ti, as well as potentially toxic elements like Hg, Pb, Cr, Cd, and As, exist⁴². Exhaust emissions and non-exhaust emissions (e.g., brake pads and tires) also contain elevated levels of Pb, Zn, Cu, Cd, Cr, Ni, V, and As, including several ultra-trace metals like Pt, Pd, and Rh abundantly in the ultrafine fraction, as suggested in many roadside studies^{43,44}. Other metal contamination sources include Cu from catenaries, Cr and Mn from wheels and rails in subway environments⁴⁵.

1.2.1 UFP AND ADVERSE HEALTH EFFECTS

UFP has been linked to a wide range of health consequences, such as cancer and cardiovascular and respiratory disorders. Its capacity to induce oxidative stress, inflammation, and its genotoxicity- the latter crucial in carcinogenicity - has been linked to several health effects⁴⁶. Oxidative stress can arise through various mechanisms, such as the reactive surface of UFP generating reactive oxygen species (ROS) through interactions with mitochondria or inflammatory cells. The formation of DNA adducts with various PAHs or ROS-mediated DNA strand breaks can also result in genotoxic consequences⁴⁷. If damage to cellular DNA surpasses the repair capacity, mutations can arise, playing a critical role in cancer development. In general, UFP possess a larger and often more reactive surface area than larger particles, making them more likely to induce toxic effects. The association of UFP-induced cancer, such as adenocarcinoma in the lungs and malignant brain cancer, has been studied⁴⁸⁻⁵⁰. Cardiovascular disorders from increased arterial stiffness and blood pressure following short-term and long-term UFP exposures at individual levels are accompanied by changes in many proteins, lipids, and metabolites^{51,52}. Different human and animal studies also suggest that the UFP induces the pathogenesis of airway inflammation and exacerbates respiratory disorders^{46,53,54}. One toxicological study highlighted the significance of UFP size and composition, suggesting that these characteristics can elicit distinct cellular responses⁵⁵.

Other studies have emphasized that particle chemistry is the primary determinant of toxicity³¹. Laboratory synthesis of UFP with well-defined properties offers valuable insights into the toxicity associated with specific characteristics. For instance, a study utilized standardized techniques to generate UFP under two mini Combustion Aerosol Standard (miniCAST) operating conditions, varying their chemical compositions⁵⁶. However, inconsistent cellular responses underscored the need for further optimization and controlled delivery methods.

The amount of PM in the air that will deposit in the lungs varies depending on several parameters, including the particle's size, shape, hygroscopicity and the individual's breathing pattern⁴⁷. UFP sizes ranging from 10 to 100 nm deposits are most effective in the alveolar region⁵⁷ and are not cleared as efficiently by the body's clearance mechanisms⁴⁷. A fraction of the UFP may also cross the epithelium and translocate to the bloodstream and the body's various organs^{58,59}. The particle's size, surface charge, agglomeration, and chemical composition can all affect this translocation⁶⁰. After particles are transported and translocated to different organs, the contaminants within them may preferentially accumulate in adipose tissue and/or interact with other substances, thereby enhancing their toxicity through a *Trojan Horse Mechanism*⁶¹ (Figure 3). This depends on the particle's chemical properties, reactivity, and affinity. For example, hydrophobic organic compounds have an affinity to accumulate in the body's lipid tissues and organs, leading to liver diseases⁶². Similarly, elevated genotoxicity and immunosuppression are observed when organic-coated BC is exposed to *in vitro* experiments⁶³. Particle size, chemical composition, morphology, crystallinity, surface area, roughness, porosity, agglomeration, hydrophobicity, hydrophilicity, and electromagnetism can all be implicated in the health

effects of UFP exposure³⁰. Thus, this will depend on the source of contamination and would consist of different types of pollutants, like inorganic ions, elemental carbon, trace metals, and carbonaceous organic matter⁶⁴. According to some researchers, the particle's toxicity depends primarily on its chemical rather than physical characteristics³¹. However, the physical and chemical characteristics of UFP are greatly dependent on its geographic location, weather, and source of emissions. They are present in the ambient air with varying levels of pollutants, making it complex to identify and predict which characteristics of UFP are responsible for its toxicity.

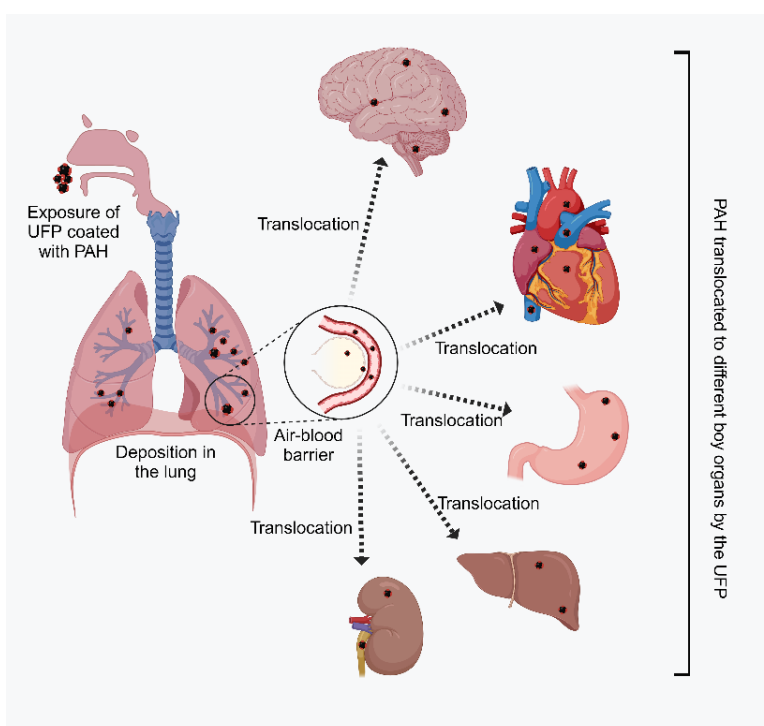


Figure 3. UFP exhibits the 'Trojan Horse Mechanism', which translocates PAH from the ambient environment to various body organ systems.

effects of UFP exposure³⁰. Thus, this will depend on the source of contamination and would consist of different types of pollutants, like inorganic ions, elemental carbon, trace metals, and carbonaceous organic matter⁶⁴. According to some researchers, the particle's toxicity depends primarily on its chemical rather than physical characteristics³¹. However, the physical and chemical characteristics of UFP are greatly dependent on its geographic location, weather, and source of emissions. They are present in the ambient air with varying levels of pollutants, making it complex to identify and predict which characteristics of UFP are responsible for its toxicity.

1.2.2 CHALLENGES ASSOCIATED WITH MONITORING AND CHARACTERIZING UFP

Monitoring UFP presents several challenges due to its distinct physical and chemical properties. UFP often consists of semi-volatile compounds that evaporate or condense depending on temperature and concentration gradients⁶⁵. It can be challenging to precisely detect and capture their actual size distribution and chemical constituents. Additionally, their high surface area-to-volume ratio provides a sufficient surface for gas-particle interactions, allowing semi-volatile compounds to absorb onto or desorb from particles readily. Thus, measurements of particle-phase vs gas-phase species may be altered by this dynamic partitioning, which can change during sampling, particularly in response to temperature or pressure fluctuations⁶⁶. Furthermore, UFP are vulnerable to diffusion losses in sampling lines because of their high diffusivity and small sizes. Even minor adjustments to the length or bends of the tubing can result in significant particle losses, which could understate the accurate concentrations⁶⁷. Many particle counters struggle to detect the smallest UFP (less than 10 nm), and it often requires multiple instruments to measure particle number concentrations reliably across a wide range of sizes (e.g., Scanning Mobility Particle sizer (SMPS) for size distribution, Condensation Particle Counter (CPC) for total number concentration)⁶⁸.

The two most widely used metrics for characterizing the PM are number concentration and mass concentration. UFP contribute negligibly to the particle mass and is usually undermined¹¹. Thus, a better way to monitor and characterize UFP is by their counts or the number concentration⁶⁹. However, most regulatory bodies and systems use mass-based PM metrics as they are relatively easy and economical and thus suited for widespread monitoring. Many parts of the world have significantly improved air quality and decreased air pollution-related morbidity and mortality due to efficient particle mass-based regulation of air pollutant emissions and concentrations⁷⁰. Nevertheless, these particle mass-based controls are insufficient to guard against the possible negative consequences of UFP exposure, at least to the extent that they do not correlate with fine particle mass, and the mass concentrations exhibit inconsistent correlations with the concentration of UFP^{11,48}. Thus, the effect of UFP on human health and its contribution to diseases have been historically undervalued. There is no consensus on a standardized method for measuring/ reporting ambient UFP, nor are there clear guidelines defining acceptable UFP levels.

Sampling of UFP is possible; however, their physical and chemical characterization is highly challenging due to the samples' extremely low mass, often falling below the detection limits of most mass-based analytical instruments. The analysis becomes even more complex because most UFP released during fossil fuel combustion are condensable particulate matter. These particles originate in the vapor phase during combustion and rapidly condense upon cooling in ambient air, forming solid salts or liquid droplets, which may later evaporate when diluted in the atmosphere.

1.3 CONTROLLED LABORATORY GENERATION OF UFP

1.3.1 MIMICKING ATMOSPHERIC SOOT AND METAL EMISSIONS

Soot formation results from incomplete combustion, which has various physical and chemical characteristics. Several chemical and physical processes are involved in the complicated

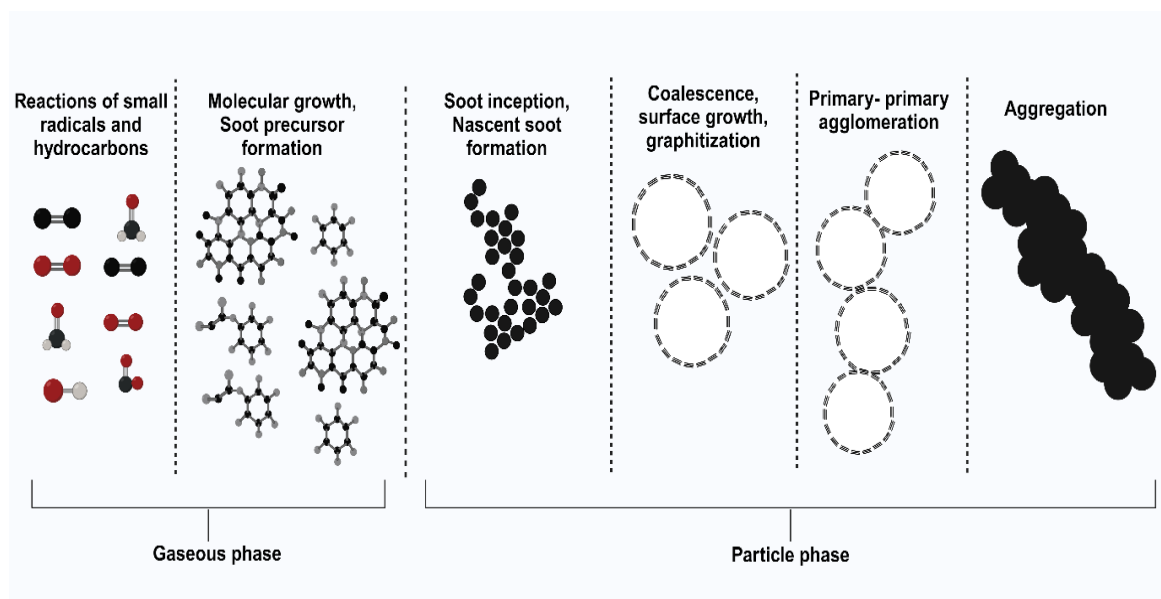


Figure 4. *Formation of soot and its characteristics from the gaseous phase.* Soot forms through the reaction of radicals and hydrocarbons in the gas phase, leading to soot inception, coalescence, agglomeration, and aggregation.

(Adapted from Ajita et al., 2022.)

process of soot production during combustion (Figure 4). While the process is complex and varies with the type of fuel and combustion conditions, a general reaction pathway for soot formation can be described. At high temperatures, chain reactions involving resonance-stabilized radicals and hydrocarbons lead to initial PAHs forming in the pyrolysis zone⁷¹. This is followed by molecular growth and the formation of soot precursors. Then, dimerization and oligomerization of PAHs occur. The following stage is called "soot inception," during which the nascent soot evolves in a gas-to-particle conversion (*nucleation*)⁷². The soot nuclei then grow through the coagulation process, forming a graphitic molecular structure that resembles an onion and keeps its spherical shape. The developed soot's fractal geometry is the product of the original particle's final aggregation and subsequent graphitization. Soot's physical and chemical properties undergo dynamic changes during its formation. The C/H ratio increases from around 1 (nascent soot) to 10–20 (fractal aggregates), while density rises from $\approx 1.3 \text{ g/cm}^3$ to $1.8 - 2 \text{ g/cm}^3$ ⁷³. As soot particles evolve, the surface reactivity decreases, and the optical characteristics shift significantly⁷⁴.

Soot evolution during combustion is simulated in laboratory settings using a mixture of reduced fuel components and oxidant gas under various experimental configurations. Typically, a

hydrocarbon fuel (e.g., propane) is mixed with synthetic air in well-defined setups, such as premixed, co-annular, counterflow, and inverse diffusion flames. The fuel composition and flame configuration significantly influence soot formation and evolution. Regardless of the flame type, soot inception occurs at approximately 1400 K, while particle burnout ceases around 1300 K. Soot forms through the pyrolysis of hydrocarbons in the combustion zone, where oxidation reactions generate heat and establish a well-defined temperature and oxidation distribution. Along the vertical axis of the flame, soot precursors form at the flame front, followed by molecular growth, coagulation, and aggregation as particles rise through the flame. However, due to the oxidation layer at the flame's surface, most soot particles are burned off before exiting the flame. Soot particles can escape only if the combustion process is quenched at a specific flame height, effectively "freezing" them at a given stage of evolution. By adjusting the quenching height, the properties of soot fractal aggregates can be controlled. Modifying the fuel and oxidant flow also alters the flame height, influencing the particle size distribution at a given quenching position.

Another approach to generating soot and metal aerosol particles in laboratory settings involves using spark discharge generators (SDGs). SDGs are versatile devices capable of producing nanoparticles through spark ablation of electrodes, making them suitable for mimicking atmospheric soot and metal aerosol particles. This method generates an electric spark and, consequently, plasma within the gap between two conductive electrodes while an inert gas

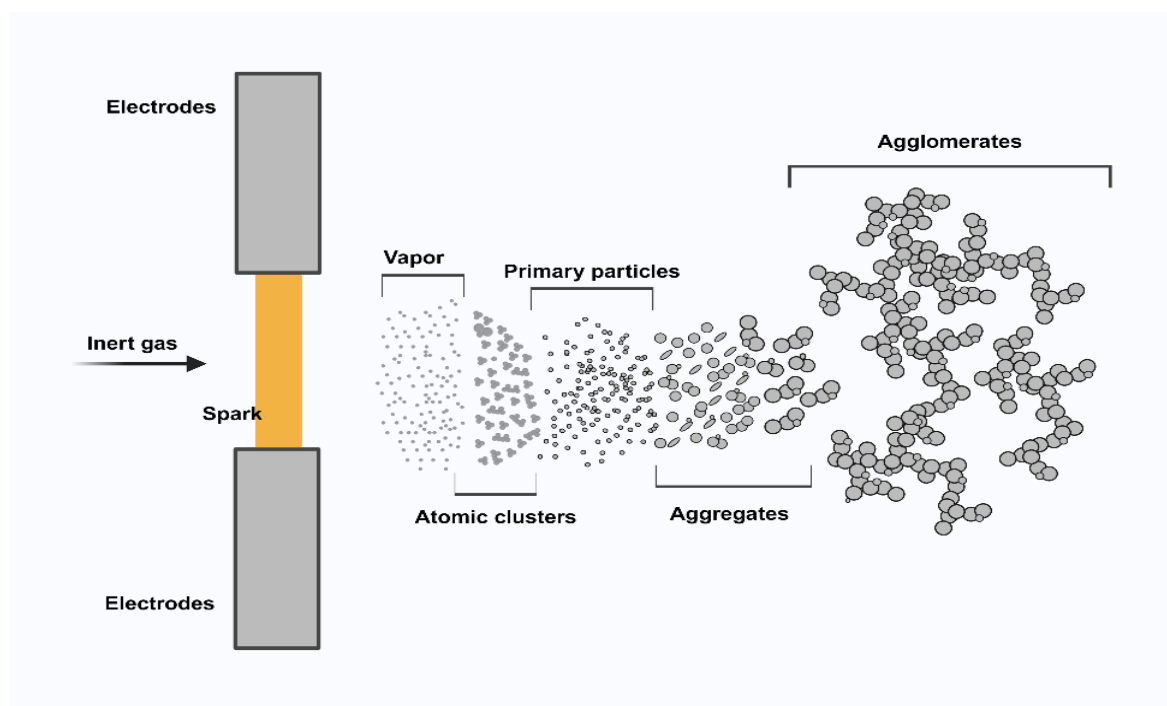


Figure 5. *Formation of atomic clusters, nanoparticles, and agglomerates from the vapor phase.*

Controlling the concentration of evaporated material during the initial stages of particle formation, the resulting product can be tuned from individual atoms to nanoparticles and their agglomerates.

(Adapted from Pfeiffer et al. 2014)

flows through the system. These electrodes are connected in parallel to a high-voltage power source and a capacitor, which is charged by a constant current supply, thereby gradually increasing the voltage between them. To ensure consistency in results, periodic discharges and a stable gas flow are maintained. When the voltage reaches the breakdown threshold of

the gas, ionization occurs, leading to plasma formation. The plasma's ions and electrons move in opposite directions until they collide with the electrodes. For a brief period, the local surface temperature of the electrodes can reach approximately 20,000 K, causing material sublimation and vapor generation. This vapor is carried away by the gas flow, which undergoes cooling and condensation, initially forming atomic clusters that aggregate into "primary" nanoparticles and eventually larger particles⁷⁵. The characteristics of the resulting particles or aggregates depend on factors such as the electrode material, gas flow conditions, particle concentration, and gas properties⁷⁶. The primary particle size is influenced by several parameters, including the breakdown voltage, spark energy (determined by the capacitor and circuit elements), carrier gas type, and flow rate⁷⁷. Higher gas flow rates enhance cooling and dilution, leading to smaller primary particles. Additionally, the electrode material properties, such as boiling point and evaporation enthalpy, impact particle size⁷⁸. The energy of the spark, influenced by the electrode gap distance and capacitance, also affects the mean particle diameter, with more significant gaps and capacitance producing larger particles⁷⁸. Depending on the type of electrodes used, various metals, such as copper (Cu), nickel (Ni), and iron (Fe), can be aerosolized using this method. SDG techniques are also applied to non-metallic conductive materials, and the electrode shape and arrangement influence the morphology of the final products⁷⁹. A schematic of the particle formation in SDG is presented in Figure 5.

In addition to flames and spark discharges, laser ablation (LA) generates particles under carefully controlled laboratory conditions. Laser excitation can generate carbon aerosols or aerosol standards. The LA system comprises two primary components: a pulsed laser serving as the light source and an ablation chamber housing a solid target. Key laser parameters such as wavelength, pulse duration, fluence, and the target's thermo-optical properties influence the physicochemical characteristics of the resulting particles⁸⁰. When nanoseconds or longer pulses are used, dominant physical processes include nucleation, condensation, coagulation, and aggregation. The applicability of the laser ablation method for the controlled production of surrogate atmospheric soot was first demonstrated using a KrF excimer laser with a wavelength of 248 nm and a pulse duration of 18 ns⁸¹. Maintaining a stable yield requires consistent laser fluence, achieved by placing a quartz plate in the beam path to reflect 4% of the energy onto an energy meter. A high-purity monolithic graphite disc (3 cm in diameter, 5 cm in thickness) serves as the target. Soot generation depends on the laser's wavelength, power, and the graphite's thermo-optical properties. Soot is not produced below a specific energy threshold, whereas exceeding it causes photon absorption, leading to erosion and evaporation⁸⁰. Focusing the beam maximizes fluence and creates a deep ablation crater ($\sim 10^{-7}$ m wide), but repeated pulses reduce yield from the same area. The graphite target is mounted on a rotating holder to ensure consistent particle concentration. The rotation speed is synchronized with the laser's repetition rate and the irradiated area, enabling uniform etching and stable yields over several hours. The laser ablation technique can also be applied to aerosolize metals by selecting an appropriate solid metal target, such as Cu, Ni, Fe, and others, to generate metal aerosol particles of a controlled size and composition.

Another method for generating metal aerosol particles in controlled laboratory conditions is through atomization techniques, such as ultrasonic or pneumatic systems, which can produce metal-containing aerosols by dispersing metal precursors (e.g., metal salts) dissolved in a liquid. These precursors are atomized into fine droplets, and subsequent drying or thermal decomposition produces metal or metal oxide aerosols⁸². Other methods to generate metal aerosols in laboratory settings include nebulization, electrospray, etc⁸².

The development of aerosol particle generators that simulate atmospheric soot and metal emissions has enabled researchers to replicate emission scenarios under controlled laboratory conditions, allowing for the study of specific aerosol properties. These systems

produce aerosols with diverse characteristics, which are crucial for evaluating their impact on climate and human health. One key application of these techniques is the study of UFP, particularly in toxicological research, where aerosol properties can be modified to investigate their impact on various biological mechanisms.

1.4 EXPOSURES TO UFP

Current knowledge regarding the health effects of UFP is predominantly derived from epidemiological studies and toxicological studies conducted using *in vitro* and *in vivo* exposure methods. Numerous studies have utilized UFP and nanoparticles (NP), such as soot, metals, cerium, and titanium dioxide, to investigate their health impacts. Unlike UFP, NP is purposely made with specific sizes, shapes, surfaces, and features, which can be used in numerous physical, biological, biomedical and pharmaceutical applications⁸³. Epidemiological research also highlights the potential risks associated with UFP exposure. However, the most recent comprehensive review of epidemiological studies on UFP-related health effects, published in 2019, concluded that the evidence linking UFP exposure to mortality and morbidity remains inconsistent or insufficient^{47,84}. This review emphasized that a critical challenge in evaluating UFP-related health effects lies in the quality of exposure assessment⁸⁴. While essential for assessing human exposure under realistic conditions, epidemiological studies often face limitations in accurately estimating actual exposure levels. These studies typically rely on sparse measurements taken at monitoring sites distant from the affected populations or use modeling approaches with inherent assumptions. As a result, toxicological studies are crucial in providing precise measurements of exposure concentration and duration. They are instrumental in determining the relative contributions of different pollutant mixture components and disentangling independent biological responses to UFP exposure⁴⁷.

Controlled human exposure experiments are valuable for understanding the biological mechanisms triggered by exposure to pollutants. Studies have consistently shown increased oxidative stress and pulmonary inflammation biomarkers following UFP exposure, although the inflammatory response can vary depending on individual susceptibility, as seen in asthmatic subjects⁸⁵. Associations have also been found between traffic-related UFP and genomic damage in exhaled breath condensate (EBC), though these experiments are limited by small sample sizes, high costs, and safety considerations, making it difficult to establish clear exposure-response relationships or clinically significant effect thresholds⁸⁶.

In vivo experiments, also known as animal studies, are widely used for realistic exposure scenarios. Inhalation studies directly assess UFP toxicity. Research indicates that UFP exposure can lead to cardiovascular and systemic effects, including increased susceptibility to cardiac arrhythmia, atherosclerotic lesions, and systemic oxidative stress, with variations depending on particle size, composition, and underlying genetic susceptibility^{87,88}. However, decisions about exposure methods, doses, and endpoints are critical and challenging when studying UFP.

In contrast, *in vitro* techniques provide a promising alternative to human or animal exposure studies. *In vitro* methods involve a variety of considerations, such as the choice of cell type (human or animal), primary cells versus cell lines, single-cell cultures versus mixed cultures, and the selection of media (e.g., with or without serum)⁸⁹. *In vitro* techniques are crucial for understanding cause-and-effect relationships (*a mechanistic approach*), particularly in identifying which particle properties trigger toxicological effects. This is especially significant for UFP, which remains poorly understood and presents a considerable research challenge.

Moreover, critical decisions regarding exposure methods, doses, and endpoints remain particularly challenging when studying UFP toxicity. While traditional *in vitro* models are simple and limited in their ability to mimic the complexity of *in vivo* systems, advancements in co-culture and triple-culture techniques have emerged. These innovations have significantly enhanced the physiological relevance of *in vitro* studies.

Submerged assessments are commonly chosen for the *in vitro* technique. This assessment involves the test substances being dosed into the culture medium and the cultured cells being immersed in the medium; thus, it is not realistic^{90,91}. Over the past few years, however, new techniques that utilize advanced exposure systems have emerged, more closely resembling the physiological aspects of airway exposure to airborne particles, thereby being more biomimetic. Air-Liquid Interface (ALI) exposure systems in respiratory toxicology are increasingly used to expose aerosols by deploying *in vitro* cell cultures^{92,93}.

1.4.1 AIR-LIQUID INTERFACE (ALI) EXPOSURE SYSTEMS

The primary advantage of the ALI exposure systems is that they function similarly to realistic exposure, which involves delivering particles in mixtures with the surrounding air and directly depositing them onto tissue-cell cultures^{94,95}. Figure 6 shows a simplified demonstration of an air-liquid exposure. Modern multi-well *in vitro* aerosol exposure systems make exposing and evaluating aerosols easier in high-performance systems with great flexibility, efficiency, and capability⁹⁶. These systems often allow for the adjustment of the conditions of aerosol exposure (e.g., dilution of the pollutants to influence the dose deposited on the cell cultures)⁹⁶. These systems' growing intricacy and complexity demand a thorough understanding of their capabilities and the conditions under which they can consistently deliver reliable, repeatable, and reproducible outcomes⁹⁶. According to a computer model approach, aerosols extending in size from 40 to 450 nm deposition in the ALI exposure system are similar to those in the lung areas⁹⁷.

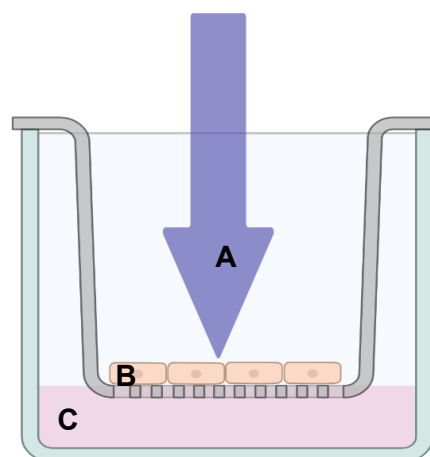


Figure 6. Air/ liquid interface cultivation and exposure using an exposure module. (A) Direct and controlled exposure of the test atmosphere to cells at the air/liquid interface; (B) cells are cultured on a membrane support; (C) nutrient medium is maintained below the membrane. This setup ensures minimal losses, prevents reactions of key components with the culture medium, and allows high sensitivity in cellular response detection.

(Adapted from Vitrocell)

The modular design of most ALI exposure systems facilitates the sequential processes of aerosol input and delivery, transport, dilution, sampling, and deposition, followed by exhaust. Depending on the system design and aerosol, its properties (concentration, size, and phase partitioning) may be continuously altered throughout the process⁹⁶. The flow conditions, the geometry of the system and aerosol characteristics can affect the losses and deposition in the ALI as physical interaction mechanisms, including impaction, sedimentation, interception, and diffusion, govern them^{98,99}. Changes in the particle size distribution, thereby altering the

aerosol properties, can also occur through particle growth, clustering, or shrinkage resulting from evaporation, condensation, and coalescence. Numerous factors influence these changes, including flow rate, particle number density, multi-component composition, and polydispersity of the aerosols under investigation¹⁰⁰. A flowing aerosol usually enters the exposure system after being diluted to a recommended dosage, causing biological effects while preserving the survival of biological tissue. The dilution step is generally done by mixing the aerosol with conditioned air at a specific temperature and humidity. This may impact the characteristics of aerosols, particularly liquid aerosol particles, where vapor/ liquid partitioning plays a crucial role. Furthermore, introducing diluting air increases the volumetric flow rate, which, in turn, raises the velocity of the diluted aerosol. Depending on the distribution of particle sizes, this increase in velocity may alter the aerosol sampling efficiency¹⁰¹, particle deposition, and system losses⁹⁹.

After the dilution step, only a portion of the entering aerosol is deposited in the exposure well chamber. The primary factors influencing aerosol sampling from the main pipe are the aerosol particle's size-dependent inertia and shape. It is generally advised to avoid further disruptions of the flow and recirculation zones along the whole transport path to reduce the possibility of changes in aerosol properties or losses⁹⁶. Finally, depending on the flow, geometry, and aerosol properties (such as size distribution and particle number density), the sampled aerosol approaches the tissue where maximum deposition is necessary. Therefore, it is crucial to comprehend the aerosol dynamics in the exposure systems when performing exposure studies and consider potential aerosol changes¹⁰². Much work has previously been done to define different components and phenomena in the exposure systems, both computationally and experimentally, to achieve steady and consistent aerosol delivery to biological cell cultures^{103,104}.

Deposition efficiency is a critical factor in ALI exposure systems. The physical properties of aerosol components, such as particle size distribution and particle number density, closely interact with the thermodynamic properties of liquid mixtures (e.g., vapor-liquid phase partitioning) to influence deposition⁹⁶. Various ALI aerosol-cell exposure devices have been designed based on the mechanisms facilitating aerosol deposition onto cells. Earlier methods primarily depended on aerosol particle diffusion and sedimentation⁹². The use of electrostatic and thermophoretic enhancements has been shown to improve deposition efficiency and delivery rates, thereby reducing the exposure duration required to achieve biologically relevant target doses¹⁰⁵. Cloud-enhanced gravitational settling has also been introduced to increase aerosol deposition rates and material delivery efficiency by utilizing dense particle clouds with faster settling speeds than individual aerosol particles¹⁰⁶. Yet, due to the complex physical processes regulating aerosol transport and deposition, it is impossible to precisely determine aerosol delivery to biological test systems based on aerosol mass flows. Furthermore, several aerosol characteristics can vary beyond relative humidity, temperature, and concentration. These include the particle number-size distribution, total particle mass, partitioning of semi-volatile compounds between particulate matter and the gas-vapor phase, and even the aerosol's chemical composition^{107,108}. Additionally, exposure systems may not always perform with complete reproducibility, as aerosol dilution can lead to inaccurate dosing, and non-uniform aerosol distribution across replica cell culture inserts may occur¹⁰⁹.

Recent years have focused on creating theoretical models to predict deposition in ALI systems. However, only a few models have been concurrently adapted and validated with experimental data. As a result, dose-estimation models often remain specific to the exposure system used, lacking generalizability across studies¹¹⁰. One study investigating deposition in ALI systems used fine and ultrafine aerosol particles, such as EC-90 and polystyrene particles, with median diameters of 90 nm and 196 nm, respectively¹¹¹. These studies were not

conducted in multi-well systems and did not explore material-dependent deposition efficiency. Another study examined material-dependent deposition using liquid SiO₂ and polystyrene suspensions¹⁰². Theoretical models have also been developed to predict size-dependent aerosol deposition efficiency⁹⁶. This thesis will experimentally determine the deposition efficiency of various UFP in a multi-well system, focusing on the relationship between particle characteristics and deposition behavior.

2 SCOPE OF THE THESIS

UFP being complex, alters the atmosphere's physical and chemical properties during their lifetime. The source-specific characteristics of the UFP in the vicinity of its emission sources change rapidly as it moves away from its source, and the physical and chemical aging masks the initial emission characteristics⁸⁰. Thus, to minimize the uncertainties associated with determining UFP exposure, the controlled generation of UFP in laboratory settings with simulated atmospheric processes is considered helpful. These controlled generations of UFP, combined with the advanced exposure techniques, may also help provide reference-based values for its toxicity. The laboratory UFP aerosol generation methods can also help ascertain if one characteristic of UFP is more harmful than another, as they can be controlled relatively easily.

This PhD thesis aims to develop different types of UFP aerosols, specifically soot UFP with varying organic loads (UFP-H and UFP-L) and copper UFP (Cu-UFP), using extensively researched laboratory generators such as the miniCAST soot generator and the spark discharge generator, respectively. These UFP were generated with the focus to facilitate its use for investigating UFP toxicity in the ALI, with sufficient particle mass required in such analyzes. All the UFP aerosols had similar size distributions and particle mass concentrations, which would aid in future work to understand the effect of chemical composition compared to their physical characteristics. Although ALI exposures have many advantages, significant dosimetric problems arise when investigating the action of aerosol particles on airway epithelial cells through *in vitro* experiments, which require direct access of the gas medium to the cells. Thus, quantitative analyzes were also investigated in the framework of this thesis for deposition determination and compared with model studies. The main research questions within the scope of this thesis were:

- 1) Can a robust method be developed to produce UFP aerosols with consistent physical properties and variable chemical compositions?
- 2) How do the physical and chemical properties of soot UFP contribute to *in vitro* toxicity?
- 3) Is it possible to establish a reliable method for determining the deposited mass concentration of UFP in the ALI system?
- 4) What are good endpoints/ analytes for bringing environmental and ALI monitoring together?

3 METHODOLOGY

3.1 LABORATORY GENERATION OF SOOT AEROSOL: CAST

Soot evolution during combustion is simulated in laboratory settings using a mixture of reduced fuel components and oxidant gas under various experimental configurations. A mixture of a hydrocarbon substance (propane) and synthetic air is used in multiple well-defined experimental configurations, including premixed flames, normal, and inverse co-annular or counter-flowing diffusion, to create soot in flames under controlled laboratory conditions.

The fuel structure and experimental configuration primarily influence the evolution of soot. In combustion flames, such as those in a miniCAST soot generator¹¹². Soot particles form through the pyrolysis of hydrocarbons within the combustion zone (Figure 7). Oxidation reactions occurring within the flame contribute to heating the combustion zone. The specific flame design ensures a symmetrical distribution of temperature and oxidation throughout its geometry⁸¹. The flame's vertical axis is where particle formation and growth occur. At the flame front, molecules grow, and soot precursors are formed. Soot nuclei form and grow in the lower regions of the flame, gradually coagulating and aggregating as they rise to higher flame positions. However, as soot particles burn up when they pass through the oxidation layer at the flame's surface, very few or none survive. Only when the combustion process is quenched at a specific height can the soot particle escape the flame¹¹³. When the combustion process is stopped, quenching stops the chemical reaction and "freezes" the soot particle at that point in its evolution. Therefore, the distinctive characteristics of the soot fractal aggregates can be changed by adjusting the vertical position of quenching. Alternatively, the height of the flame can be adjusted by altering the flow of the oxidizing air and fuel gas, which will also impact the size distribution at a particular quenching position.

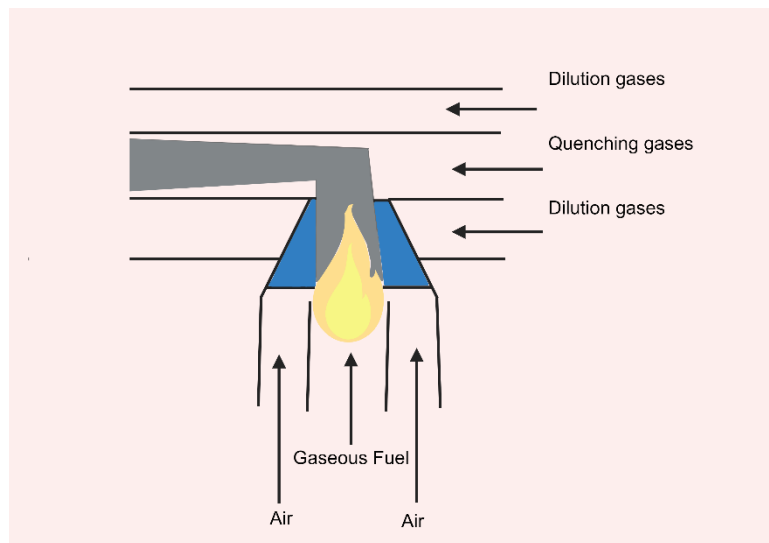


Figure 7. Soot generation using the CAST. The incomplete combustion of propane produces soot particles in a diffusion flame. Initially formed during pyrolysis, the particles become coated with exhaust gases before exiting the combustion chamber, where they are mixed with quenching gas to stabilize their properties.

(Adapted from www.sootgenerator.com)

Soot nuclei form and grow in the lower regions of the flame, gradually coagulating and aggregating as they rise to higher flame positions. However, as soot particles burn up when they pass through the oxidation layer at the flame's surface, very few or none survive. Only when the combustion process is quenched at a specific height can the soot particle escape the flame¹¹³. When the combustion process is stopped, quenching stops the chemical reaction and "freezes" the soot particle at that point in its evolution. Therefore, the distinctive characteristics of the soot fractal aggregates can be changed by adjusting the vertical position of quenching. Alternatively, the height of the flame can be adjusted by altering the flow of the oxidizing air and fuel gas, which will also impact the size distribution at a particular quenching position.

3.2 CATALYTIC STRIPPING

A catalytic stripper (CS) can efficiently remove the semi-volatile component particles from internally and externally mixed aerosols. They are primarily utilized to detect raw exhaust

particles from combustion engines. The CS is a heated catalytic component designed to oxidize and eliminate the semi-volatile fraction, leaving the solid fraction for further assessment. Hydrocarbon and sulfate species removal by oxidation and trapping are two catalytically driven processes combined in a CS system. The initial version of the CS used a commercial oxidation catalyst heated to 300°C, and a downstream cooling coil was used to lower the temperature to ambient levels¹¹⁴. However,

high particle losses hindered the effective removal of hydrocarbons and ammonium sulfate particles. The second version combined the CS with a vortex tube diluter to reduce thermophoretic losses¹¹⁵. The evaporation tube was recently replaced with a smaller CS, which suggested another CS variation in conjunction with a sulfur trap upstream of the primary oxidation catalyst¹¹⁶. The goal was to improve oxidation performance by capturing sulfate material before it reached the oxidation catalyst. This system determined the non-volatile fraction of vehicular emissions¹¹⁷ and performed better than the traditional thermodenuder systems¹¹⁸.

The CS version used in this study (Catalytic Instruments; Model CS015; Germany) removes the semi-volatile fraction of a sample by evaporating the semi-volatile component (350°C), oxidizing the organic species, and allowing the solid aerosol fraction to pass through to be detected by any particle detector¹¹⁹. By passing an aerosol stream through a CS before a particle instrument, only the solid fraction of the particle remains, leading to adaptivity in changing the aerosol chemical loads (Figure 8). This approach enabled the evaluation of varying chemical compositions of the UFP, which were subsequently analyzed for their toxicological impacts.

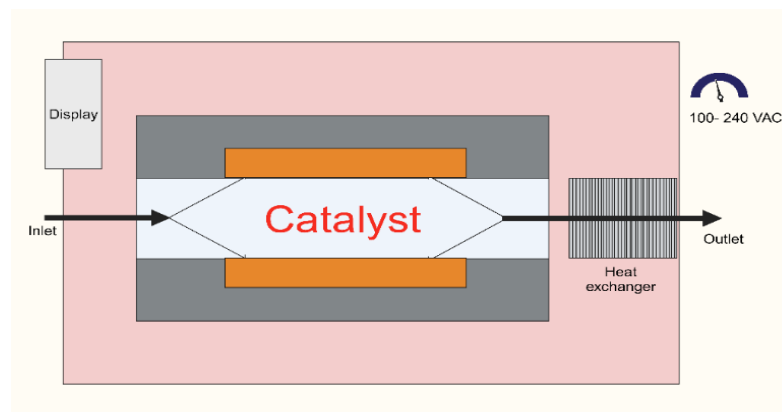


Figure 8. *Principle of a Catalytic Stripper*. It is a heated catalytic device that removes particle- and gas-phase semi-volatile components from an aerosol, enabling the measurement of non-volatile particle fractions.

(Adapted from www.catalytic-instruments.com)

3.3 CHARCOAL DENUDER

Denuding is an approach used in aerosol sampling to remove volatile organic compounds (VOCs) and atmospheric oxidants from the gas phase, thereby preventing them from interfering with the analysis of carbonaceous aerosols collected on particle-phase filters. In the denuder approach, an organic denuder is placed upstream of a quartz filter, where gaseous organics are removed by diffusion to an adsorbent surface, such as activated carbon or a polystyrene-divinylbenzene resin¹²⁰. This study used a square multichannel charcoal denuder with 325 squared channels, measuring 0.9 mm × 0.9 mm (Helsatech, Germany), to remove gas-phase organics from the UFP soot. The setup also included a copper UFP¹²¹.

3.4 LABORATORY GENERATION OF METAL AEROSOL

The first spark discharge device for generating nanoparticles was developed in 1988¹²². The Spark Discharge Aerosol Generation (SDG) technique creates an electric spark, generating plasma in the gap between two conductive electrodes, with a gas flowing through this region. The voltage across the electrodes is increased by connecting a high-voltage source in parallel with a capacitor, which is charged by a steady current source. When the potential difference reaches the gas's breakdown voltage, the gas ionizes, producing plasma. During discharge, the electrode's local surface temperature increases to approximately 20,000 K, causing the material to sublime and generate vapor. This vapor is carried away by the gas flow, where it rapidly cools and condenses, forming the initial atomic clusters and the "primary" nanoparticles. These nanoparticles then aggregate, combining into larger particles^{75,123} (Figure 6). Within the plasma, ions and electrons move in opposite directions until they collide with the electrodes. Several factors influence the characteristics of the resulting particles or aggregates, including the electrode material, flow conditions, primary particle concentration, and gas properties⁷⁸. Periodic discharges and a steady gas flow are used to ensure reproducible results.

The breakdown voltage that produces the spark, the energy supplied by the circuit (capacitor, etc.), the type of carrier gas, the movement of the gas between the electrodes, and other factors all affect the size of the primary particles^{75,76}. Increasing the gas flow rate enhances cooling and dilution rates, resulting in smaller primary particles. Their sizes are influenced by the properties of the electrode material, including its evaporation enthalpy and boiling point⁷⁸. The spark's energy is influenced by the gap distance between the electrodes and capacitance; increasing these parameters results in larger particle mean diameters. While the shape and arrangement of the electrode influence the morphology of the final product, spark discharge techniques can also be used in non-metallic conductive materials⁷⁹.

The SDG used in this study (Palas, model GFG 1000, Germany) was employed with cylindrical copper electrodes to produce the copper ultrafine particles (Cu-UFP). The carrier gas used was argon (Ar), as the breakdown voltage for argon is higher than for helium (He), which will give a higher energy per spark in Ar⁷⁶. The generated Cu-UFP enabled the analyzes of the toxicological implications of metal UFP.

3.5 EXPERIMENTAL SETUPS

3.5.1 SOOT UFP

This study generated two types of soot UFP. These laboratory-generated UFP sources were a miniature combustion aerosol standard soot generator (miniCAST, model 5201C; Jing Ltd; Switzerland). The miniCAST creates a diffusion flame by introducing the oxidizing air coaxially into a stream of propane¹¹². A very high concentration of UFP rich in organics can be created by quenching the flame with nitrogen, internally diluting it, and cooling it to roughly 50°C inside the miniCAST¹²⁴. Flows were optimized for a fuel-rich condition to create UFP with high organic content ($\lambda = 0.80$, $\Phi = 1.25$). The corresponding flow rates for the burner air, dilution air, propane, and quench-N₂ were 1.05 L/min, 0.055 L/min, 7 L/min, and 20 L/min, respectively. The miniCAST's working conditions remained consistent across all of the experiments. A homemade porous tube diluter (PTD) with an adjustable dilution ratio and an ejector diluter with a fixed 1:10 dilution ratio (VKL 10; Palas, Germany) were used to

immediately dilute the miniCAST's exhaust, preventing coagulation and the production of larger agglomerates. To maintain consistent characteristics (particle number and mass concentrations) of the UFP throughout the experiments, the dilution in the PTD was adjusted at the start of each experiment and then slightly readjusted over the four hours. The particle's organic loading varied by passing the diluted UFP aerosol through a catalytic stripper (CS, Model CS015; Catalytic Instruments; Germany) at different temperatures, along with a charcoal denuder. The particle and gas-phase semi-volatile organic compounds (SVOCs) fractions are removed from the UFP by heating the CS to 350°C. For 50 nm particles, the diffusional losses in the CS in this investigation were around 10%. On the other hand, no SVOCs were removed from the UFP when the CS was kept at room temperature, resulting in an organic load higher than that of the UFP stripped at 350 °C. To ensure UFP-only exposures, it was necessary to eliminate the organic gas phase. Consequently, the CS was followed by a square multi-channelled charcoal denuder (Helsatech, Germany) featuring 325 square channels, each measuring 0.9 mm × 0.9 mm, to remove gas-phase organics. While the particle losses in the charcoal denuder were lower than those in the CS, they were included even when the CS was heated to ensure that potential artifacts and losses remained comparable between experiments conducted with and without CS heating.

From this point forward, these two UFP varieties were referred to as UFP-H (high-organic-load UFP) and UFP-L (low-organic-load UFP). Following the denuders, a second 1 in 10 ejector diluter guided the UFP through a subsequent dilution phase, continuously taking 1.65 L/min. Subsequently, various instruments were used for online characterization, UFP collection for offline aerosol analysis, and cell exposure in the Automated Exposure Station (AES; Vitrocell GmbH; Germany).

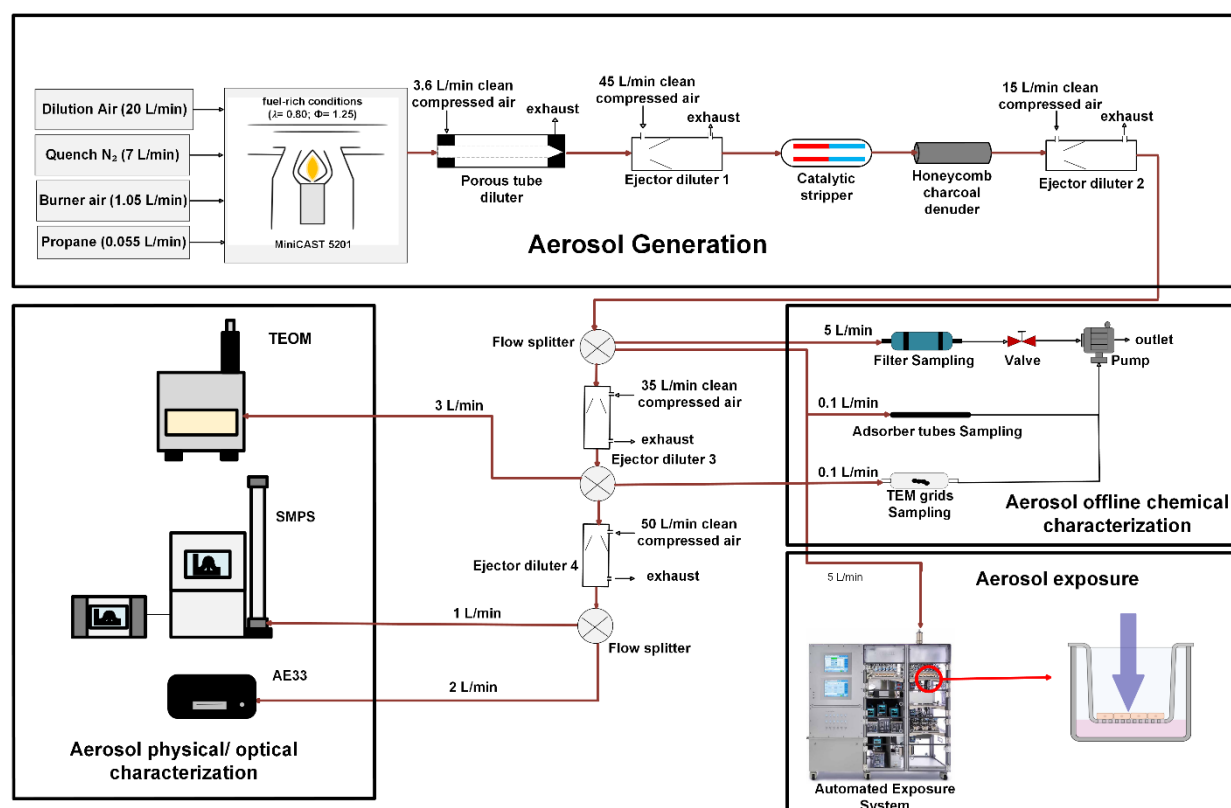


Figure 9. Experimental set-up of soot generation, characterization, sampling methods and exposure in the ALI. TEOM - Tapered Element Oscillating Microbalance, SMPS - Scanning Mobility Particle Sizer, AE33 – Aethalometer, TEM – Transmission Electron Microscopy. (Adapted from Das et al. 2024)

A schematic of the experimental setup is shown in Figure 9. To reduce particle losses and chemical reactions throughout the system, conductive perfluoroalkoxy (PFA) tubing was used. This material prevents static charge buildup, which can cause particle losses, ensuring high transmission efficiency¹²⁵. Based on flow rates, PFA tubing with inner diameters of 4 mm or 10 mm was selected to maintain laminar flow and minimize turbulence-related losses. All instruments and the AES were positioned close to the miniCAST to limit UFP diffusion losses. However, some diffusional particle losses and coagulation during transport remain unavoidable.

3.5.2 COPPER UFP

The metal UFP was generated using a spark discharge generator (Palas, model GFG 1000, Germany). Copper electrodes were used, and the inert gas was argon, supplied at a pressure of 1.3 bars and a flow rate of 4.75 L/min. The cylindrical copper electrodes were positioned 2 mm apart at a spark frequency ranging from 800 to 999 Hz. From this point forward, the copper UFP produced is referred to as Cu-UFP. The Cu-UFP was then neutralised by a Palas neutraliser (Palas; model XRC 049; Germany) and passed through a 5 L vessel and a perfluoroalkoxy (PFA) coil of 3 m in length and 10 mm internal diameter to achieve the desired particle mobility diameter. The Cu-UFP was passed through a square, multi-channelled charcoal denuder with 325 squared channels, 0.9 mm x 0.9 mm (Helsatech; Germany), to remove gas-phase organics that might originate from the vessel. The Cu-UFP was then diluted with an ejector diluter using a fixed 1:10 dilution ratio (VKL 10; Palas Germany) to achieve the desired particle number concentration. The Cu-UFP were then split into the Air Liquid Interface System for exposure, Particle phase filter sampling, and another ejector diluter fixed at a 1:10 dilution ratio. This diluter was then connected to the aerosol online characterization

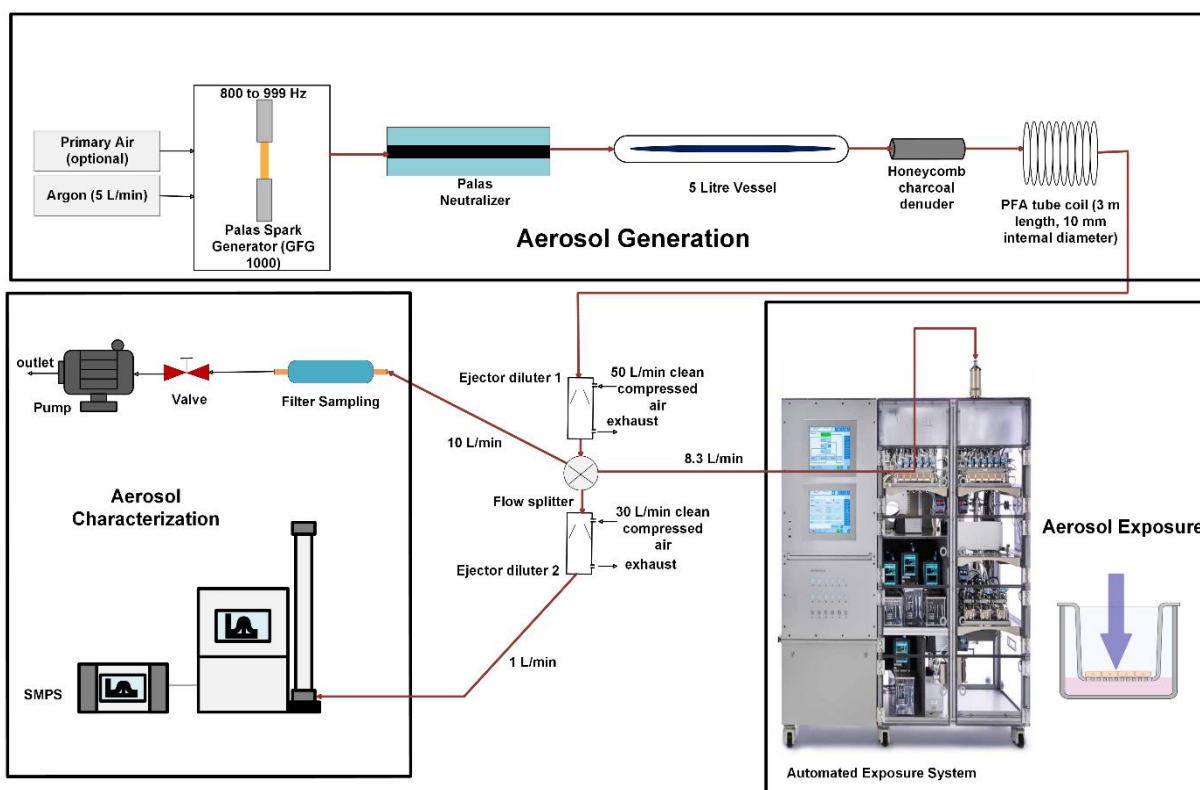


Figure 10. Experimental set-up of Cu-UFP, characterization, sampling methods and exposure in the ALI. SMPS - Scanning Mobility Particle Sizer.

instruments and the exposure system in the Automated Exposure Station (AES; Vitrocell GmbH, Germany).

Figure 10 shows a schematic of the experimental setup. PFA tubing was utilized to minimize particle losses and chemical reactions within the system. This tubing prevents static charge accumulation, which can lead to particle losses, thereby ensuring high transmission efficiency¹²⁵.

3.6 AEROSOL ONLINE CHARACTERIZATION

Online aerosol characterization refers to the real-time measurement of aerosols (in situ). Several real-time methods exist to assess aerosols, including optical methods, electrical mobility, and mass spectrometry. These methods help characterize dynamic aerosols, enabling us to understand their properties, behavior, impact on climate, air quality, and health.

Online particle number size distribution (PNSD) measurements are commonly conducted using electrical mobility analyzers, with the Scanning Mobility Particle Sizer (SMPS) being the most widely used instrument¹²⁶. An SMPS comprises an impactor to remove large particles, a neutralizer to charge particles predictably, a differential mobility analyzer (DMA) to classify particles, and a condensation particle counter (CPC). The core of an SMPS is the DMA, which classifies particles based on electrical mobility. The most common DMA design features two concentric cylindrical electrodes. Aerosol enters near the outer electrode and is carried upward by the flow. A particle-free sheath flow surrounds the inner electrode, preventing contact with the aerosol unless a voltage is applied. When voltage is applied, particles of one polarity are attracted toward the inner electrode, while those of opposite polarity are repelled outward. The radial migration velocity depends on the applied voltage and the particles' electrical mobility, as expressed in the Equation:

$$Z_p = \frac{n \cdot e \cdot C_c \cdot (d_m)}{3 \cdot \pi \cdot \eta \cdot d_m} \quad (1)$$

In this equation, n denotes the number of elementary charges (e), d_m the mobility diameter, η the gas viscosity, and C_c the Cunningham slip correction factor¹²⁷. The latter accounts for the reduced drag forces on smaller particles due to non-specular molecular reflections, which deviate from Stokes' law. Particles with specific electrical mobility exit through a narrow slit near the upper end of the inner electrode. The instrument can cover a full range of particle sizes by ramping the DMA voltage.

Black carbon (BC) measurement is another crucial target for aerosol characterization, and its definition highly relies on the measurement techniques employed. Optical instruments commonly indirectly determine equivalent black carbon (eBC) mass concentrations, and filter absorption photometers, such as aethalometers, are widely used. The aethalometer provides online and continuous BC data by measuring light attenuation from particles collected on a filter at specific wavelengths¹²⁸. The measured attenuation is converted to an absorption coefficient (b_{abs}) and then into eBC mass concentrations using predefined mass absorption cross-section (MAC) values provided by the instrument manufacturers¹²⁹. When employing light absorption methods, the term equivalent black carbon (eBC) should be used instead of BC as a proxy for b_{abs} ¹³⁰.

$$eBC = \frac{S \cdot (\Delta ATN_1 / 100)}{F_1(1-\zeta) \cdot \delta_{abs} \cdot (1-k\Delta ATN_1) \cdot \Delta t} \quad (2)$$

where S denotes the filter surface area loaded with the sample; F_1 the volumetric flow of spot 1; ζ the lateral airflow leakage; δ_{abs} the mass-absorption cross-section; k the loading factor parameter; and ΔATN_1 the variation in attenuation of light of the filter tape loaded with the sample of spot 1, ATN_1 , during the measurement timestamp Δt .

Another aerosol optical property describing the wavelength variation in aerosol absorption is the Absorption Ångström Exponent (AAE)¹³¹. The AAE is defined as

$$C_{\text{abs}}(\lambda) = C_0 \lambda^{-\text{AAE}} \quad (3)$$

Where λ , C_{abs} , and C_0 denote wavelength, the aerosol absorption coefficient, and a wavelength-independent constant (equal to the absorption coefficient at a wavelength of 1 μm)¹³². The AAE is widely used in aerosol characterization studies, as it is considered a distinct property of each aerosol species¹³³. For example, black carbon (BC) aerosols typically have an AAE of around 1.0, while organic aerosols and dust exhibit higher values. An AAE close to 1.0 indicates BC-rich aerosols, often linked to fossil fuel combustion^{132,133}. In contrast, higher AAE values suggest aerosols from biomass, biofuel burning, or dust sources¹³².

3.7 AEROSOL OFFLINE CHARACTERIZATION

Online characterization alone is insufficient for comprehensively assessing aerosols' physical and chemical properties. Therefore, offline characterization is crucial in evaluating and quantifying various aerosol components. A widely used approach for this purpose is aerosol filter sampling, which enables collecting, analysing, and quantifying different aerosol components.

3.7.1 PARTICLE-ASSOCIATED SAMPLING

Aerosols are commonly sampled using filter materials, including Teflon, glass fiber, cellulose, quartz, and polycarbonate. The choice of filter material is guided by its suitability for subsequent PM analysis. Quartz fiber filters (QFFs), widely used in various applications, are favored for their high particle collection efficiency, high-temperature tolerance, and low pressure drop. Within this thesis, sampling was conducted solely on QFFs. In general, QFFs belong to the group of fibrous filters and consist of many individual fibers randomly oriented in two dimensions. Several mechanisms, including diffusion, interception and inertial impaction, cause deposition. Regarding the sampling environment, various samplers can be used for particle sampling. In the current work, a home-built sampler collected the laboratory-generated UFP with a flow rate of 10 L/min for the entire experiment. Before the sampling, the QFF were preheated at 550 °C for five hours. After each experiment, filter samples collected for PAHs analysis were stored at -20°C until further analyzes, while samples for copper analysis were kept in a desiccator. Field blanks were included for correction purposes.

3.7.2 ANALYZES OF PARTICLE-ASSOCIATED PAHS IN UFP

Various pretreatment methods and analytical instruments are available for measuring particle-associated PAHs in different matrices, and extraction techniques are widely applied, particularly for samples with complex matrices. Direct thermal desorption (DTD) is a two-stage process applicable to analyze SVOCs to reduce the time-consuming sample preparation steps required for extraction-based analyzes¹³⁴. Targeted quantification of PAHs was carried out using gas chromatography-mass spectrometry (Shimadzu GC-MS-QP2010 Ultra, DTD-20 Shimadzu, Japan). The analyzes were done with the DTD technique using OPTIC-4 inlet (GL Sciences B.V., The Netherlands)¹³⁵. A simplified diagram of a gas chromatograph-mass spectrometer system is presented in Figure 11. Firstly, the QFF aliquots are taken and placed inside the GC injector. Subsequently, the injector is heated to 350°C, and analytes are desorbed. The desorbed analytes are carried by an inert gas, typically helium, through a capillary column to separate the PAHs. The separation depends on the PAH's interaction with the column's stationary phase, which could be based on polarity, size, and boiling point. Once separated, the PAHs are passed into the mass spectrometer, where they are ionized (typically by electron ionization), fragmented, and then analyzed based on their mass-to-charge ratio (m/z). A calibration curve needs to be created for the targeted quantification of PAHs. It is usually produced by injecting a known target PAHs standard concentration. Then, the areas of each targeted PAHs are measured, and the calibration curve is made. Internal standards are usually used to correct for matrix effects or variation from sample to sample. In this thesis, eleven mainly particle-associated PAHs (≥ 5 aromatic rings) and two intermediate PAHs (3-4 aromatic rings) were quantified by DTD-GC-MS.

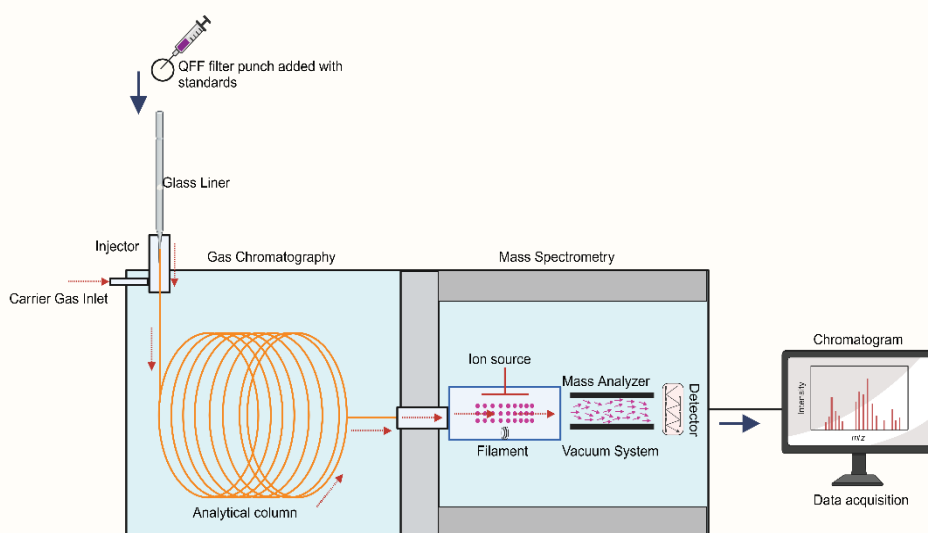


Figure 11. A simplified diagram of a gas chromatograph-mass spectrometer illustrating the following components: (1) injector, (2) analytical column, (3) ion source, (4) mass analyzer and (5) data acquisition

3.7.3 ANALYZES OF COPPER UFP

Atomic absorption spectrometry is a widely used technique for detecting and quantifying metals, including copper, in different sample types. The analysis in this thesis was conducted using an Atomic Absorption Spectrometer (AAS ZEE nit 600s, Analytik Jena, Germany) equipped with Zeeman effect background correction and a graphite furnace atomizer. The AAS was fitted with a hollow cathode lamp (copper type), and the method parameters were set in the instrument software, including the analytical line at 324.8 nm, a spectral bandpass of 0.5 nm, and a working lamp current of 2 mA.

Calibration was performed with a certified copper AAS standard solution (ROTI®Star, 1,000 mg/L Cu in 2% HNO₃) at a series of 2, 5, 10, 15 and 20 ppb. A 10% HNO₃ solution was measured as a blank, followed by a 10 ppb control standard (Analytik Jena, copper AAS standard, 2 mg/L in 0.2% HNO₃), which was prepared by diluting 0.125 mL of the 2 ppm solution in 25 mL. The calibration curve was generated with a 95.4% confidence interval, ensuring reliable quantification of copper concentrations. For copper extraction, the QFF was treated with 10 mL of 10% HNO₃ (nitric acid, ROTIPURAN® Supra, 69%). The samples were centrifuged for 5 minutes at 3000 rpm to separate particulates. The supernatant was filtered through a 0.45 µm nylon filter to remove any remaining debris. A 1:200 pre-dilution was performed before the AAS measurement to bring the copper concentration within the calibration range.

Eppendorf pipettes and corresponding tips were used for all liquid handling steps to ensure precise and accurate sample preparation.

3.7.4 MORPHOLOGY OF UFP

Transmission electron microscopy (TEM) is a powerful imaging technique that uses a beam of high-energy electrons to visualize the internal structure of solids. It is widely applied in aerosol characterization, providing detailed insights into the characteristics of aerosol particles. It enables the physical and morphological analysis of individual particles collected on a specialized support, specifically, a TEM grid. Due to this capability, extensive research has focused on optimizing direct particle deposition onto these grids, minimizing the need for additional sample preparation. It is important to note that TEM analysis at this stage provides qualitative rather than quantitative insights. Commercially available TEM grids are circular metallic supports typically composed of copper, nickel, gold, or molybdenum. They have a diameter of approximately 3 mm and are subdivided into hundreds of small squares. These grids are generally coated with a thin, translucent electron beam membrane, often made of carbon, just a few nanometers thick, which enhances the contrast of deposited particles. Various grid types and mesh sizes exist, tailored to different applications.

Several sampling techniques utilize TEM grids, relying on diffusion, thermophoresis, or electrostatic precipitation mechanisms¹³⁶. In this study, TEM grid samples were collected by passing a small volume (0.1 L/min) of aerosol for durations ranging from 7.5 to 30 minutes through a perforated carbon film on a copper carrier mesh grid (200 mesh copper; Plano GmbH, Germany). After sampling, the grids were stored in a low-humidity silica desiccator at room temperature until analysis using a TEM (JEM-2100F, JEOL Ltd., Japan) operating at 200 kV.

3.8 ANALYZES FOR THE MASS DEPOSITION OF THE UFP

The Automated Exposure Station (AES; Vitrocell GmbH; Germany) was used for air-liquid interface (ALI) exposures to quantify UFP mass deposition. The generated UFP-H and Cu-UFP were used to assess the deposition of UFP within the ALI system. The flow rate per insert was maintained at 100 mL/min, with each trumpet positioned 2 mm above the collection point. All experiments were conducted under isothermal conditions at a temperature of $37.0^{\circ}\text{C} \pm 0.1^{\circ}\text{C}$ and a relative humidity of $87\% \pm 3\%$. Before each experiment, the aerosol supply and exit lines were sealed, and the system was pressurized to xxx mm H₂O to ensure leak-free operation, following the manufacturer's guidelines. Each UFP type underwent four independent experiments, each lasting four hours, in alignment with previous ALI exposure studies^{137,138}.

Emfab air monitoring filters (TX40HI20WW, 47 mm; Pall Corporation, NY, USA) were cut to fit into Transwell inserts to collect the UFP-H. Instead of culture media, the underlying reservoir was filled with deionized water¹³⁹. After each exposure, filters were collected and stored at -20°C until analysis. Each filter was halved for separate analysis using the direct thermal desorption gas chromatography-mass spectrometry (DTD-GCMS) described in the previous section. To avoid obstructing carrier flow, filter halves were carefully rolled and placed in the GC injection liner. Thermal desorption was performed at 270°C . Four particle-associated PAHs (with ≥ 5 aromatic rings) were selected as markers for UFP-H: Sum Benzo[b,j,k]fluoranthene, Benzo[e]pyrene, Benzo[a]pyrene, and Benzo[ghi]perylene, which were quantified using single ion monitoring (SIM) mode via DTD-GC-MS.

For analyzing the Cu-UFP, empty Transwell inserts were subjected to a four-hour exposure under identical conditions, with deionized water in place of media. Following exposure, the membranes were excised, collected, and stored in a silica desiccator before analysis. For copper quantification, membranes were extracted using 1 mL of 10% HNO₃ (ROTIPURAN® Supra, 69%), vortexed at 3000 rpm for 2 minutes, and subjected to a 1:20 pre-dilution before atomic absorption spectrometry (AAS) measurement. Copper concentrations were then determined from the inserts using AAS analysis.

4 RESULTS AND DISCUSSIONS

4.1 CHARACTERIZATION OF LABORATORY-GENERATED SOOT UFP

4.1.1 ONLINE CHARACTERIZATION

The miniCAST generator generated the UFP reference soot aerosol particles, UFP-H (high organic load) and UFP-L (low organic load). They have similar physical but different chemical characteristics (Table 1).

Size distribution measurements and geometric mean mobility diameter (GMD_{mob}) of the ultrafine soot particles were obtained with a TSI Scanning Mobility Particle Sizer (SMPS) (Type 3082 TSI Incorporated, USA). The SMPS was connected at a dilution of 100 from the exposure, and subsequently, the data were corrected. The SMPS was operated at a 10:1 sheath-to-aerosol flow ratio, and the size range selected was 5.94 nm to 224.7 nm. The diffusion losses were accounted for by checking the Aerosol Instrument Manager software, version 10.3. The size distributions were fitted to lognormal functions, and all the results presented in the subsequent sections are based on fitted data.

The size distributions of UFP-H and UFP-L were similar, displaying a unimodal profile with a geometric mean diameter (GMD) of approximately 40 nm (Figure 12A). The mass size distributions for UFP-H and UFP-L were also nearly identical (Figure 12B). As the CS removes a significant portion of volatiles and semi-volatiles, the stripping of organics from soot aggregates likely contributes to the slightly smaller GMD_{mob} observed for UFP-L. The dilution in the porous tube diluter (PTD) was adjusted to maintain comparable particle number size concentrations. This adjustment was necessary because the higher temperatures in the CS for UFP-L could lead to increased losses in smaller particle size ranges. Consequently, the standard deviations of the size distributions may have increased.

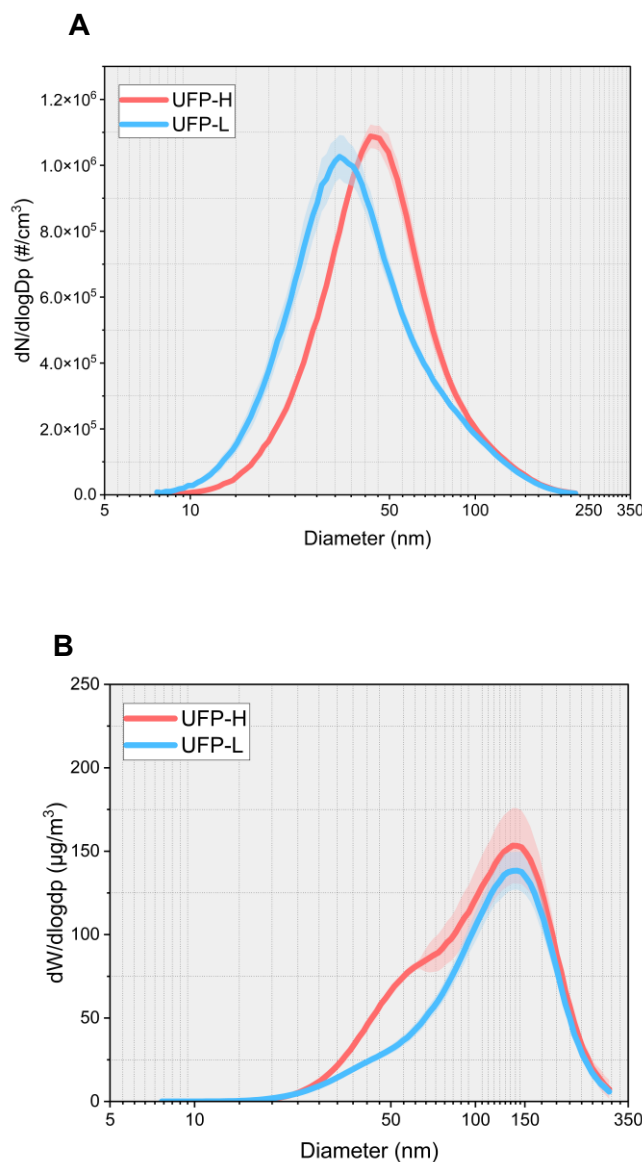


Figure 12. (A) Number size distribution and (B) Mass size distribution of UFP-H (red) and UFP-L (blue) for all the experiments ($N=11$ for UFP-H; $N=8$ for UFP-L). The shaded area represents the standard deviation of the number concentration ($\#/cm^3$) and mass concentration ($\mu g/m^3$) in each size bins, respectively.

The total mass concentration was measured with a Tapered Element Oscillating Microbalance (TEOM 1400a, Ambient Particle Monitor, Rupprecht & Patashnick Co., Inc.). The TEOM is a gravimetric instrument that continuously quantifies particulate mass concentration using a tapered-element oscillating microbalance. The TEOM takes the sample through a filter and constantly weighs it, thereby measuring the mass concentration. The TEOM was modified to operate at a flow rate of 3 L/min. The mass concentrations measured by the TEOM for UFP-H and UFP-L were similar, with a slightly lower value for UFP-L, consistent with the GMD_{mob} results. To further verify the mass concentrations, both UFP samples were cross-checked using the SMPS (assuming a density of 1 g/cm³), which yielded values of 80 µg/m³ for UFP-H and 70 µg/m³ for UFP-L.

Equivalent black carbon (eBC) and Ångström Exponent (AAE) were measured using a dual-spot Aethalometer (AE33, Magee Scientific, Berkeley, USA). The AE33 measures light transmission at seven different wavelengths (370, 470, 520, 590, 660, 880, and 950 nm) through two sample spots with varying flow rates and particle loading relative to the reference spot. The total aerosol flow in the aethalometer was set at 2 L/min. The manufacturer's wavelength-independent multiple scattering correction factor, $C = 1.39$, was applied to the built-in filter tape. The eBC, a primary tracer for combustion emissions, is estimated as an equivalent mass concentration from the change in optical attenuation at channel 6 (880 nm). Two wavelength pairs, AAE 370/880 and AAE 470/950, were used to calculate the AAE. For the two soot UFP samples analyzed, UFP-L shows a higher eBC compared to UFP-H. This increase may stem from the overestimation of using identical mass absorption cross-section (MAC) values (7.77 m²/g at 880 nm, as provided in the AE33 manual) for both types of UFP soot. Studies suggest that miniCAST-generated soot, when thermally processed and with particle sizes smaller than 100 nm, could have MAC values around 4.5 m²/g. Therefore, uncertainties in MAC values should be considered when interpreting eBC measurements¹⁴⁰. The AAE, which describes the wavelength dependence of light absorption, is a key optical property of aerosols. Each aerosol type has a distinct AAE, with BC typically exhibiting an AAE of around 1.0¹³². Due to the internal mixing of organics and BC, forming soot core-shell structures that influence the AAE, and the presence of light-absorbing compounds in organic aerosols, higher AAE values often indicate a higher organic content¹⁴¹. In this study, the AAE values for the UFP generated in our setup ranged from 1.7 (UFP-L) to 2.0 (UFP-H) across both wavelength pairs. The UFP produced by the miniCAST generator is rich in aromatic structures, as reflected by its high AAE values. The decrease in AAE from 2.0 (UFP-H) to 1.7 (UFP-L) suggests that the catalytic stripper (CS) reduced the organic matter content.

Table 1. Online characterization- Mass concentration (µg/m³), particle number concentration (PNC) (#/cm³), geometric mean diameter (GMD_{mob}) (nm), equivalent black carbon (eBC) (µg / m³) and absorption Ångström exponent (AAE) (370/880), AAE (470/950) of UFP-H and UFP-L are reported. The results are presented as four-hour averages ± standard deviations, calculated from the averages of each experiment.

Type	Mass concentration (µg / m ³)	PNC (# / cm ³)	GMD_{mob} (nm)	eBC (µg / m ³)	AAE (370/880)	AAE (470/950)
UFP-H (N= 11)	110 ± 10	50*10 ⁴ ± 2*10 ⁴	45 ± 1	47 ± 2	2.0 ± 0.1	2.0 ± 0.1
UFP-L (N=8)	90 ± 10	50*10 ⁴ ± 3*10 ⁴	40 ± 1	51 ± 3	1.7 ± 0.0	1.7 ± 0.0

4.1.2 OFFLINE CHARACTERIZATION

Particle-phase samples from both UFP aerosols were analyzed offline using a quartz fiber filter (QFF) for chemical characterization.

An untargeted screening of UFP-H and UFP-L particle-phase samples was conducted using thermal desorption comprehensive two-dimensional gas chromatography hyphenated with time-of-flight mass spectrometry (TD-GC × GC-TOFMS). Figure 13 presents bubble plots of the prominent peaks detected in the chromatograms for UFP-H (top) and UFP-L (bottom). Compared to UFP-L, UFP-H exhibited a significantly higher number of PAHs with m/z 178–300, including parent and alkylated four-, five-, and six-ring PAHs. Oxygenated PAHs were observed in relatively low concentrations exclusively for UFP-H. Similar results, indicating higher PAHs content in UFP-H, were reported using Electron Spray ionization-Fourier-transform Ion

Cyclotron Resonance Mass Spectrometry (ESI-FTICRMS)¹⁴². The authors noted the presence of larger PAHs (≥ 6 rings) with m/z values of up to 800. However, as these molecules fall beyond the volatility range detectable by GC × GC-ToFMS, our measurements could not identify them. After correcting for a filtered air sample, only trace amounts of Benz[a]anthracene, phenanthrene, and pyrene were detected in the UFP-L sample. The Environmental Protection Agency (EPA) has identified sixteen High Priority PAHs¹⁴³. In the targeted analysis using direct thermal desorption hyphenated gas chromatography-mass spectrometry (DTD-GCMS), two intermediate PAHs (containing three to four aromatic rings) and eleven predominantly particle-bound PAHs (≥ 5 aromatic rings) were measured for UFP-H and UFP-L. The PAHs in UFP-H accounted for approximately 2.5% of the total UFP mass, indicating significantly high concentrations of PAHs. Among the PAHs quantified in high concentrations in UFP-H was Benzo[a]pyrene, one of the most hazardous and well-characterized PAHs in terms of toxicity. It accounted for approximately 2 mg per gram of the total mass of UFP. Figure 14 illustrates the concentrations of all targeted PAHs, corrected for the exposure system. A semi-quantitative study using a miniCAST exhaust without a catalytic

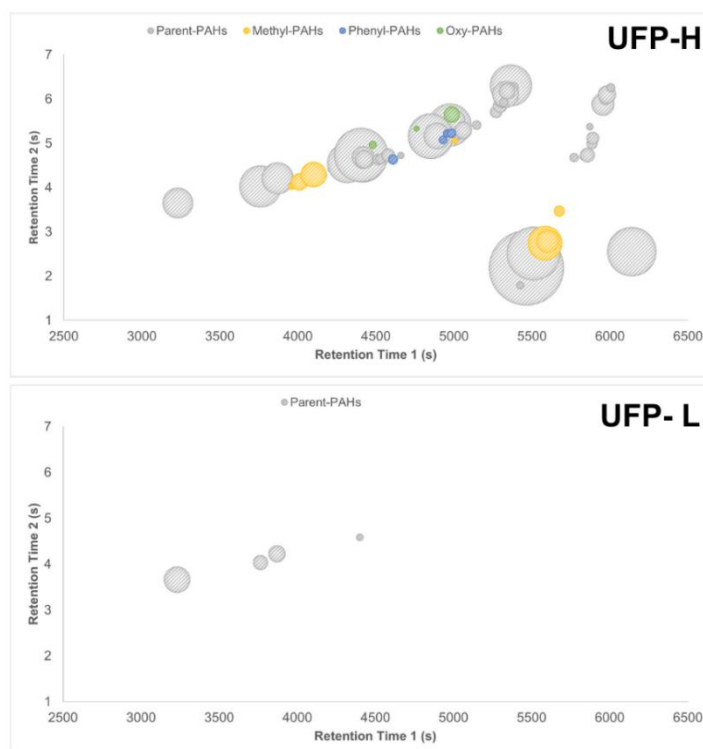


Figure 13. Chemical characterization of UFP-H (top) and UFP-L (bottom) was performed using DTD-GC × GC-TOFMS. The PAH content of the two samples is displayed within the two-dimensional separation space, with the peak area represented by the diameter of the "bubble." The plots are normalized to the area of the most abundant PAH found in UFP-H. Both samples were corrected using a measurement of purified air. Methyl-PAHs refer to methylated PAHs, Phenyl-PAHs to phenylated PAHs, and Oxy-PAHs to oxygenated PAHs.

stripper (CS) reported similar findings, observing primarily semi-volatile PAHs (m/z 176–242) and non-volatile PAHs ($m/z \geq 252$) at a λ of 0.805, with negligible amounts of volatile PAHs (m/z 78–166)¹⁴⁴. For UFP-L, the targeted non-volatile PAHs were consistently below the Limits of Quantification (LOQ) of 0.01 ng/m³.

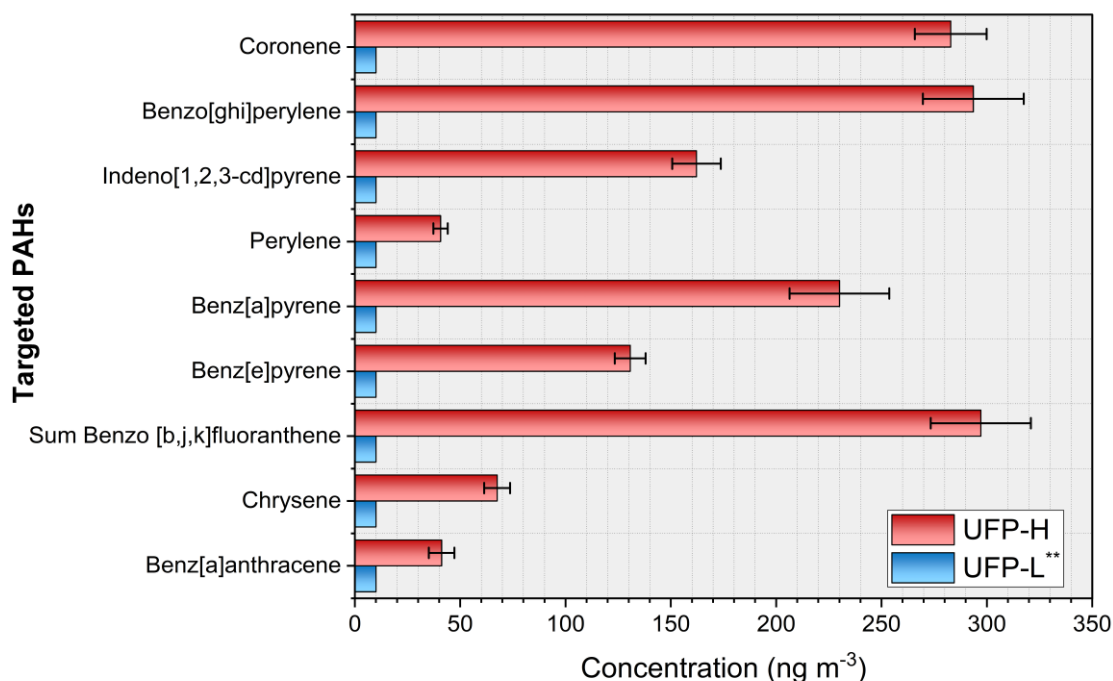


Figure 14. The concentration of PAHs in UFP-H (N=7) is shown, with error bars representing the standard deviation of each targeted PAH across all experiments.

**For UFP-L samples, all analyses were below the LOQ, which for our method is 0.01 ng/ m³

The Raman spectra of soot, used to investigate its nanostructure, feature two prominent overlapping bands at approximately 1350 1/cm (D or 'defect') and 1600 1/cm (G or 'graphite')^{145,146}. The height ratio I(D)/I(G) increase is associated with more significant structural order in amorphous and disordered carbons¹⁴⁷. Consequently, lower I(D)/I(G) values suggest more amorphous structures and are typically observed in soot samples with higher organic carbon (OC) content. The measured I(D)/I(G) ratios were 0.99 ± 0.05 (N = 3) for UFP-H and 1.05 ± 0.02 (N = 3) for UFP-L, indicating very similar structural order but with slightly higher amorphous carbon content in UFP-H. This is consistent with findings by another study, where the lowest OC soot (4%) had the highest I(D)/I(G) ratio of 1.19 ± 0.02 , while the highest OC soot (47%) had the lowest I(D)/I(G) ratio of 1.03 ± 0.03 ¹⁴⁸. Samples were collected and analyzed using a transmission electron microscope (TEM) to compare their morphology and assess the effect of thermal treatment in the catalytic stripper on the UFP structure (Figure 15). Both UFP samples exhibited soot agglomerates composed of primary particles with graphitic-layered structures, similar to soot from other combustion sources, such as diesel soot^{149,150}. The fractal aggregates of both UFP remained unchanged after thermal treatment. A geometric primary particle size of 22 ± 6 nm was measured for UFP-H (N = 54) and 22 ± 6 nm for UFP-L (N = 39). These findings align with another study on a near-stoichiometric diffusion flame using a miniCAST burner¹⁵¹. Despite the similar sizes of the primary particles, UFP-H displayed a more amorphous appearance with blurry boundaries between primary particles, suggesting a substantial presence of semi-volatile species.

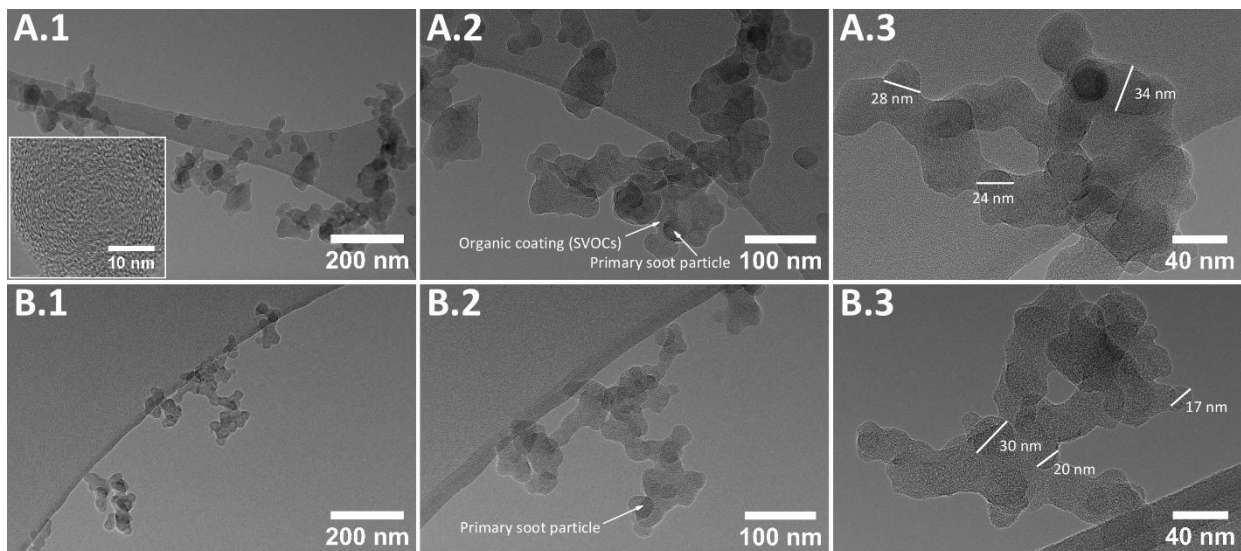


Figure 15. TEM images: A.1 UFP- H showing the graphitic structure, magnification at 50,000 \times ; A.2 UFP-H showing the primary soot particle and coating of SVOCs, magnification at 100,000 \times ; A.3 UFP- H magnification at 200,000 \times ; B.1 UFP- L magnification at 50,000 \times ; B.2 UFP-L showing the primary soot particle; B.3 UFP-L magnification at 200,000 \times .

4.1.3 TOXICOLOGICAL EFFECTS

The toxicological effects of two soot aerosol particles, UFP-H and UFP-L, were investigated in human alveolar epithelial cells (A549) using the Automated Exposure System at the air-liquid interface (ALI).

Cytotoxicity was assessed by measuring lactate dehydrogenase (LDH) release into the basolateral exposure medium, indicating cell membrane rupture and necrotic cell death. Both aerosols induced significant cytotoxicity, with cell death reaching approximately 27% compared to the clean air (CA) control (Figure 16). Similarly, cell viability analysis revealed a reduced metabolic activity to 56% for UFP-H and 50% for UFP-L, significantly lower than the CA control (82%) (Figure 16).

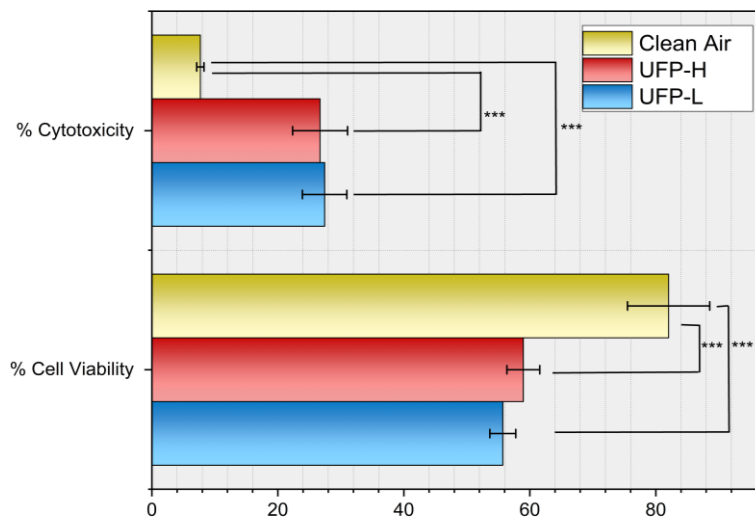


Figure 16. % Cytotoxicity and % Cell Viability. The percentage of cytotoxicity measured by LDH release in cell medium following four-hour exposure and the percentage of cell viability measured by the resazurin assay following four-hour exposure of A549 cells. Bars represent the average \pm s.e.m (N = 3). Statistically significant results with respect to CA are marked with asterisks (*, $p < 0.05$; **, $p < 0.01$; ***, $p < 0.001$)

These findings suggest that UFPs can trigger necrosis, potentially driving inflammation by releasing danger signals that activate the NLRP3 inflammasome, a key regulator of

inflammatory responses¹⁵². Previous studies have shown that UFPs impair cell viability and metabolism, often at higher concentrations than those used in our study^{153–155}. However, toxicity mechanisms depend highly on aerosol chemical composition, a factor frequently overlooked in setting regulatory limit values^{154, 156, 157}.

Despite no significant differences in cytotoxicity between the two aerosol types, a detailed analysis revealed distinct effects on oxidative stress, xenobiotic metabolism, and genotoxicity. After a 4-hour exposure, UFP-L (with lower organic content) induced a significant oxidative stress response, as evidenced by increased intracellular reactive oxygen species (ROS) generation (Figure 17). This response was seemingly balanced by the glutathione (GSH) antioxidant system, as indicated by elevated oxidized glutathione (GSSG) levels, which may also reflect reduced activity of oxidative stress-related enzymes, such as glutathione reductase, which facilitates GSSG-to-GSH recycling, a mechanism previously proposed for ambient PM toxicity¹⁵⁸. Disruptions in GSH regulation are critical in lung inflammatory processes and are associated with diseases such as cystic fibrosis and asthma¹⁵⁹.

The UFP types caused slight elevations in malondialdehyde (MDA), a marker of lipid peroxidation. This suggests that antioxidant defenses were partially overwhelmed, leading to oxidative damage to cell membrane phospholipids (Figure 16)¹⁶⁰. UFP-H exposure significantly increased EROD activity and modestly enhanced BROD activity (Figure 18), indicating the activation of phase I metabolic enzymes like CYP1A1^{157, 161, 162} and CYP3A4¹⁶³, which are typically induced by PAH

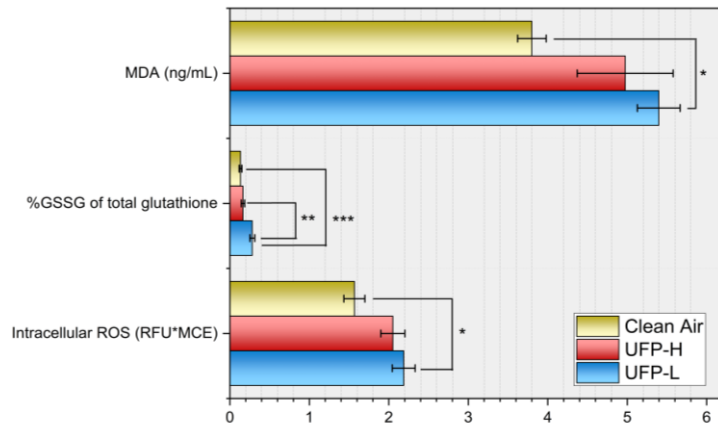


Figure 17. The potential of oxidative stress was investigated by detecting the amount of MDA [ng/mL] released into the sample medium, the percentage of intracellular oxidized glutathione (GSSG) to the total glutathione, as well as the formation of intracellular ROS (RFU*MCE) following a four-hour exposure of A549 cells. Bars represent the average \pm s.e.m (N = 3). Statistically significant results with respect to CA are marked with asterisks (*, $p < 0.05$; **, $p < 0.01$; ***, $p < 0.001$)

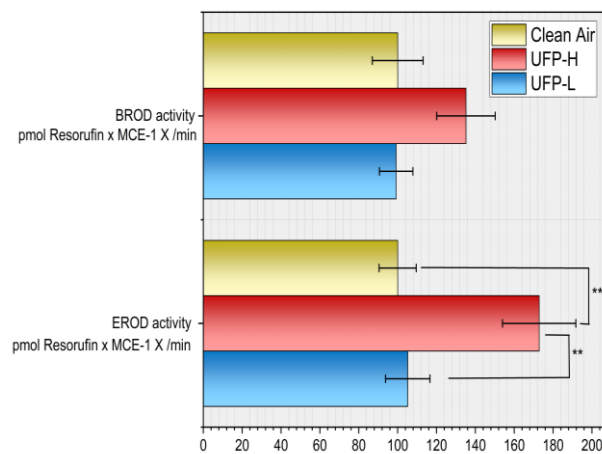


Figure 18. Induction of the resorufin intensity by increased activity of 7-ethoxyresorufin-O-deethylase (EROD) and 7-benzyloxyresorufin-O-debenzylase (BROD) normalized by the metabolic cell equivalent (MCE) following four-hour exposure of A549 cells. Bars represent the average \pm s.e.m (N = 3). Statistically significant results with respect to CA are marked with asterisks (*, $p < 0.05$; **, $p < 0.01$; ***, $p < 0.001$)

and are abundant in UFP-H, such as Benzo[a]pyrene and Benzofluoranthenes. In contrast, UFP-L did not activate these enzymes, confirming the chemical distinctions between the two aerosols.

Genotoxicity analysis highlighted differential DNA damage patterns. Both aerosols caused DNA strand breaks, but UFP-L induced more extensive damage. Particles with high organic content appeared to promote DNA modifications recognized by the base excision repair enzyme Fpg (Figure 19), consistent with previous findings linking increased Fpg-sensitive sites to PAHs exposure^{164,165}.

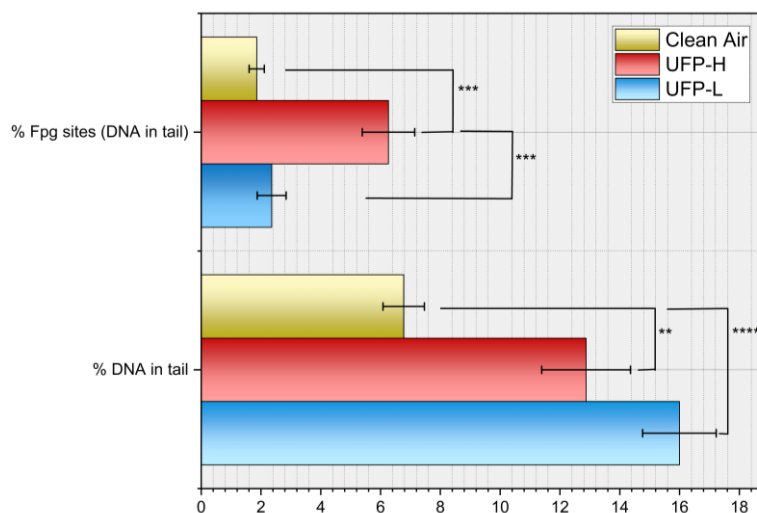


Figure 19. Percentage of DNA in tail and Fpg sites (% DNA in tail) detected by comet assay following four-hour exposure of A549 cells. Bars represent the average \pm s.e.m (N = 3). Statistically significant results with respect to CA are marked with asterisks (*, $p < 0.05$; **, $p < 0.01$; ***, $p < 0.001$)

4.1.4 INDICATORS OF UFP TOXICITY

With the two types of UFP soot generated (UFP-H and UFP-L), toxicological results showed similar effects in simpler assays assessing cytotoxicity. However, differences became more apparent when evaluating oxidative stress, metabolic indicators, and genotoxicity. These findings highlight the importance of chemical composition, as physical characteristics such as number and mass concentration were kept constant. This underscores the need to consider particle chemistry in future toxicological assessments and regulatory frameworks. Notably, the polycyclic aromatic hydrocarbons (PAHs) present in UFP-H can induce their own metabolism by upregulating xenobiotic-metabolizing enzymes such as cytochrome P450 monooxygenase 1A1 (CYP1A1), potentially via activation of the aryl hydrocarbon receptor (AHR)¹⁶⁶. Additionally, individual PAHs may also interact with the constitutive androstane receptor (CAR)¹⁶⁷. More detailed analyzes, such as transcriptomics and proteomics, should be considered to understand better the mechanisms driving toxicity.

4.2 CHARACTERIZATION OF LABORATORY-GENERATED COPPER UFP

4.2.1 ONLINE CHARACTERIZATION

The study utilized a spark discharge generator (SDG) to produce the copper ultrafine particles (UFP), specifically the Cu-UFP. During the experiment, the Cu-UFP were characterized by mobility size using the TSI Scanning Mobility Particle Sizer (SMPS) (Type 3082, TSI Incorporated, USA). Particle number concentrations and mobility size distributions were measured using a sheath flow rate of 10 L/min and an aerosol flow rate of 1 L/min. The size range selected for the operation was 5.94 nm to 224.7 nm, and the diffusion losses were accounted for by checking in the Aerosol Instrument Manager software, version 10.3. The size distributions were fitted to lognormal functions, and all the results presented in the subsequent sections are based on fitted data. The geometric mean mobility diameter of Cu-UFP was 33 ± 2 nm, slightly smaller than the UFP-H discussed in the previous section. The particle number concentration of Cu-UFP was approximately twice as high as that of UFP-H, likely due to its smaller mobility diameter. The primary particle size of Cu-UFP, generated via spark discharge, typically ranges from 1 to 9 nm, which is significantly smaller than that observed for UFP-H in TEM studies¹⁶⁸. Assuming a 1 g/cm^3 density, the SMPS mass concentrations for the Cu-UFP were approximately $90 \text{ }\mu\text{g/m}^3$. The particle number size and mass distributions for the Cu-UFP are given in Figure 20.

4.2.2 OFFLINE CHARACTERIZATION

The Cu-UFP were also collected on quartz fiber filters to quantify their mass concentration and validate the measurements obtained from the SMPS. The filter samples were analyzed using Atomic Absorption Spectroscopy (AAS), which determined a copper concentration of $80 \text{ }\mu\text{g/m}^3 \pm 10 \text{ }\mu\text{g/m}^3$ across all experiments (N=5). Additionally, the filters were examined for iron (Fe) to assess the purity of the Cu electrode used in the SDG. The Fe concentration was

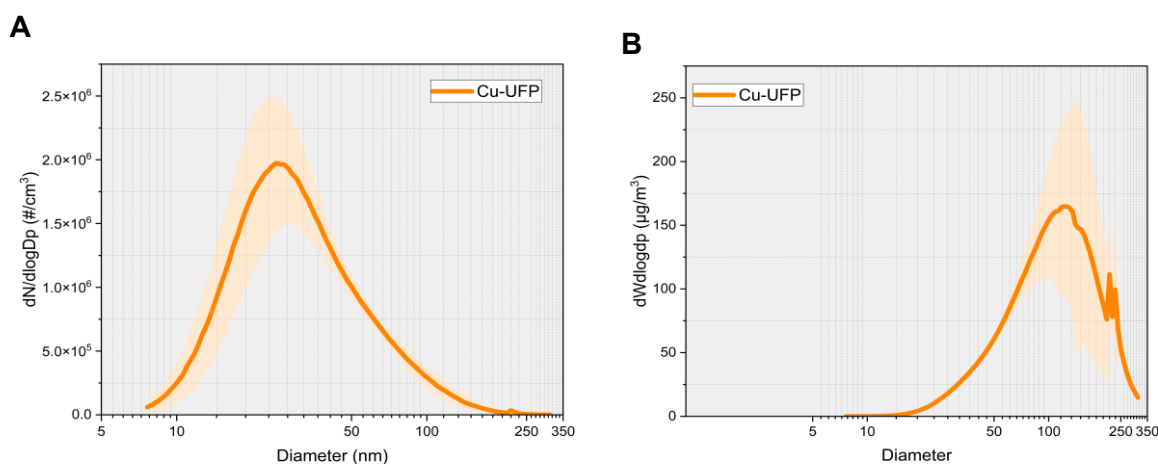


Figure 20. (A) Number size distribution and (B) Mass size distribution of Cu-UFP for all the experiments (N=5). The shaded area represents the standard deviation of the number concentration (#/cm³) and mass concentration ($\mu\text{g/m}^3$) in each size bin, respectively.

0.9%, potentially resulting from contamination during electrode manufacturing or using a stainless steel punch for aliquot punching.

4.3 TOWARD RELIABLE UFP MODELS FOR TOXICOLOGICAL ASSESSMENT

Studying UFP is crucial because, compared to larger particles, they exhibit significantly higher particle number concentrations and surface areas and greater levels of toxic substances like oxidant gases, organic compounds, and transition metals relative to their mass. Laboratory studies also show that UFP have substantially greater redox activity than larger particulate matter. However, conducting epidemiological studies on UFP health effects requires careful consideration of complex exposure assessment challenges, such as spatial variability, indoor emission sources, differences in how outdoor UFP infiltrate indoor environments, and seasonal changes influenced by weather and particle volatility.

To address the complexities of UFP toxicity and explore potential mechanisms of action, this thesis utilizes well-characterized surrogate UFP models. Three distinct types of UFP were developed, each with comparable number and mass concentrations but markedly different chemical compositions: one enriched in PAHs, one with low PAHs content, and one containing metals. These models serve as representative aerosols for key toxicants like soot, PAHs, and metals, providing a controlled framework to study their effects. While such models inherently simplify the vast variability of ambient air, they enable a more precise mechanistic investigation into UFP-induced toxicological responses. No standardized UFP model or in vitro testing protocol exists to assess toxicity or establish reference values applicable to real-world emissions. Thus, developing robust and validated surrogate UFP models is critical for linking toxicological outcomes to specific physical and chemical particle properties.

4.4 DOSIMETRY IN ALI SYSTEMS

Recent studies investigating the toxicity of UFP using ALI exposure systems have been increasing, particularly in the context of sources such as fuel exhaust emissions¹⁶⁹, aircraft turbine engines¹⁷⁰, printer emissions¹⁷¹, and the miniCAST burner^{56,172}. However, in many of these studies, the delivered aerosol dose to cells is often estimated using model calculations, extrapolated from submerged exposure dose–response relationships, or determined via electrostatic deposition combined with quartz crystal microbalance (QCM). These approaches are employed due to current limitations in online measurement techniques for deposited mass in ALI systems, e.g., QCM approaches its detection limit in the UFP size range. Electrostatic deposition can enhance particle delivery efficiency but may introduce artifacts by altering the physicochemical environment. Specifically, electric charging can affect the ionic composition of the culture media and potentially impact cell viability. Moreover, the charging process might modify aerosol properties, influencing toxicological outcomes¹⁷³.

Regarding dosimetry, most ALI studies rely on inert solid particles tagged with fluorescent markers, such as glycerol^{108,174}, or e-cigarette vapor^{109,175}, and mainstream tobacco smoke^{95,176}. Inert particles have also been widely used for developing and validating computational dosimetry models in these systems^{96,102,107,111,139}. However, a key limitation of these models is that they are often based on idealized particles and vary across different ALI platforms, raising questions about the accuracy and relevance of the predicted doses. There

remains uncertainty as to whether the modeled dose reflects the actual cellular exposure or merely serves as a theoretical estimate.

Therefore, in the context of this thesis, UFP generated from specific sources (UFP-H and Cu-UFP) were used to experimentally determine the deposited mass in an ALI system, specifically the Automated Exposure Station (AES; Vitrocell GmbH; Germany). These experimental results were then compared to predictions derived from computational modeling to assess the validity of the modeled doses.

4.4.1 MEASURED MASS DEPOSITION

For the UFP-H, three particulate-associated PAHs were selected as marker components to determine the total UFP mass deposited after the four-hour exposure. These PAHs included the Sum Benzo[b,j,k]fluoranthene, Benz[e]pyrene and Benz[a]pyrene. EMFAB filters were used for levels X and Y, with four positions from level X (X1, X2, X3, X4) and six positions from level Y (Y1, Y2, Y3, Y4, Y5, Y6) considered for the experiments. Figure 21 presents the PAHs deposited per filter area for each exposed insert. Statistical analysis using Welch's ANOVA showed no significant differences in individual PAH levels between inserts ($p > 0.05$). A correlation-based pattern analysis was performed to evaluate potential variations in PAHs composition across inserts. The lowest correlation value obtained was 0.92, indicating a consistent distribution of PAHs across all inserts. This high correlation suggests no alteration in the ALI system's PAHs profile and confirms the accuracy of the analytical quantification. In parallel with ALI exposure in the AES, particulate-phase filter samples were collected using QFF outside the AES to track PAHs concentrations and the amount deposited. Table 2. Summarizes the concentration obtained from the filter samples in the deposition experiments. The deposition of Cu-UFP on inserts exposed in the AES at the ALI was conducted at levels X (X1, X2, X3, X4) and Y (Y1, Y2, Y3, Y5, Y6) for four hours. The inserts were exposed for four hours, after which the Transwell membrane was extracted and analyzed to quantify the mass deposition of Cu-UFP. Figure 22 presents the measured Cu-UFP deposited in each exposed insert, as determined by AES at the ALI. Similar to the UFP-H analysis, a Welch ANOVA was performed for Cu-UFP, revealing no significant differences between inserts ($p > 0.05$).

Table 2. Concentration of PAHs obtained using DTD-GCMS from the particulate phase in UFP-H. Results are presented as mean \pm standard deviation ($n = 6$) for each PAH compound.

Sum Benzo[b,j,k]fluoranthene (ng/m ³)	Benzo[e]pyrene (ng/m ³)	Benzo[a]pyrene (ng/m ³)
70 \pm 4	66 \pm 5	71 \pm 7

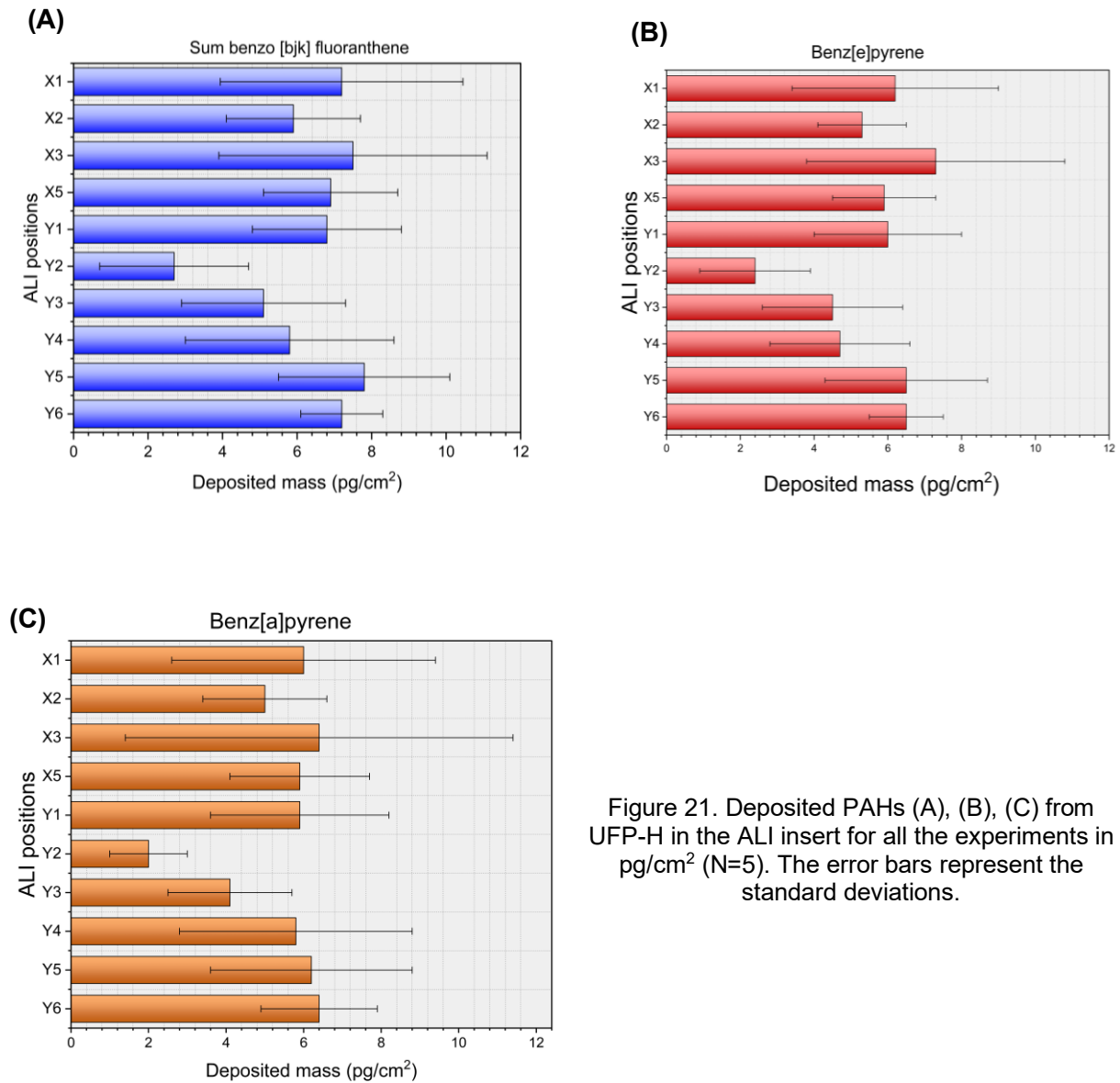


Figure 21. Deposited PAHs (A), (B), (C) from UFP-H in the ALI insert for all the experiments in pg/cm^2 (N=5). The error bars represent the standard deviations.

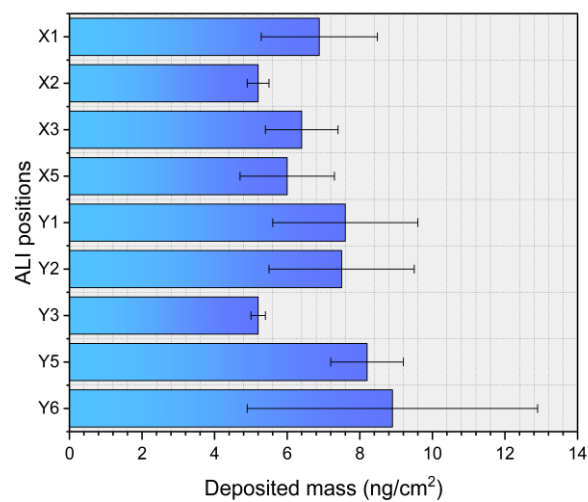


Figure 22. Deposited Cu-UFP in the ALI insert for all the experiments in ng/cm^2 (N=5). The error bars represent the standard deviations.

4.4.2 ESTIMATED MASS DEPOSITION

The quantified deposition was then compared to the model-estimated deposition. The deposited PM mass per area was calculated using the following equation: Equation (4),

$$\text{Deposited mass per area} \left(\frac{\text{ng}}{\text{cm}^2} \right) = \frac{\eta \times Q \times N \times t \times \rho_p \times V_p}{A} \quad \text{Equation 4}$$

where η is the deposition efficiency; Q is the aerosol flow; N is the particle number concentration (particle count per volume); t is the duration of the exposure; ρ_p is the particle density; V_p is the particle volume, assuming spherical particles; and A is the area of the insert.

The size-dependent deposition efficiency (η) in the ALI exposure system was calculated using the theoretical framework described in a previous study⁹⁶. In this model, particle deposition is primarily governed by size-dependent diffusion and sedimentation mechanisms: larger particles deposit predominantly by sedimentation, while smaller particles deposit via diffusion. The deposition efficiency is influenced by multiple factors, including particle size and density, aerosol flow rate, temperature, pressure, and system geometry. The particle number concentrations used in the model were obtained from SMPS measurements during the exposure period. The densities of UFP-H and Cu-UFP were set to 1.0 g/cm³ and 0.9 g/cm³, respectively. Density plays a crucial role in deposition calculations, as it affects the determination of deposition efficiency and the conversion of deposited particle number to deposited mass. The area of the insert was set to 4.67 cm² according to the surface area of the inserts used. The aerosol flow and temperature over each position were set to 100 mL/min and 37°C, respectively.

As estimated by the model, the deposited mass area for UFP-H and Cu-UFP was 1.0 ± 0.2 ng/cm² and 1.3 ± 0.2 ng/cm², respectively. Correspondingly, the deposition efficiency was calculated to be 0.22% ± 0.03% for UFP-H and 0.8% ± 0.1% for Cu-UFP. These modeled values were then compared to the experimentally measured UFP mass, revealing significant discrepancies. For UFP-H, the model underestimated the deposition of individual PAH markers compared to measured values. Specifically, the deposited mass of Benzo[b,j,k]fluoranthene, Benz[a]pyrene, and Benz[e]pyrene was found to be 7 to 8 times higher in the experimental data than in the model predictions. A similar trend was observed for Cu-UFP, where the model underestimated mass deposition by a factor of 5. These discrepancies may be related to assumptions regarding boundary layer thickness at the deposition plate. This theoretical model was developed based on the Vitrocell VC24/48 and AMES systems, using a sampling rate of 20 mL/min. It is assumed that the sampled particle flow rate physically constrains the theoretical maximum deposition, and therefore, actual deposition efficiency must be taken as the minimum of the two fluxes. However, this thesis employed the Automated Exposure Station, a structurally different system, with a significantly higher sampling flow rate of 100 mL/min. To address these differences, an alternative approach was employed in this study, estimating boundary layer thickness using Brownian displacement over a characteristic time¹⁷⁷. While this approach was acknowledged in the original paper from which the modeling was adapted, it was not implemented, as the Computational Fluid Dynamics (CFD) simulations in that study suggested that boundary layer thickness had a lower dependence on deposition efficiency in the diffusion regime. Their validation, which involved comparing modeled deposition with CFD results, demonstrated good agreement for particles larger than 0.3 µm; however, they noted that further refinements could improve accuracy in the ultrafine particle range. Applying the Brownian displacement

approach in this study resulted in higher estimated UFP mass deposition, bringing model predictions closer to experimental values. The revised model underestimated UFP-H deposition by only 2 to 3 times, from 7 to 8 times, and Cu-UFP deposition by a factor of 2, rather than 5. Thus, the recalculated deposition efficiency becomes 1% for UFP-H and 2% for Cu-UFP, as seen in previous studies^{177,178}. This suggests that boundary layer thickness plays a more significant role in UFP deposition than previously assumed, particularly for ALI systems that differ structurally, are exposed to varying flow rates, and encounter more complex aerosols.

These results underscore the need for system-specific modeling adjustments to accurately predict UFP deposition, as variations in sampling methods, airflow dynamics, and particle interactions can significantly impact the estimated deposition efficiency.

4.4.3 COMPARING ALI EXPERIMENTS WITH HUMAN EXPOSURE MODELS

ALI cellular exposures offer several advantages, including enhanced reproducibility, physiological relevance in respiratory toxicology, and suitability for short- to mid-term exposures. A key consideration is the comparability of ALI-based exposures with actual human inhalation scenarios. In this context, evaluating particle deposition in ALI systems concerning the human lung's tissue-delivered dose (TD) is essential.

Using the same ALI system as employed in this thesis, a previous study applying the Hygroscopic Particle Lung Deposition (HPLD) model identified a particle size range of 40–450 nm in which the ratio between deposition in human lung regions and in the ALI system varied by less than a factor of two. This range corresponds to the mobility diameters utilized in the present work, supporting the representativeness of the measured mass deposition. Moreover, HPLD model outputs suggest that deposition in ALI systems should be moderately increased for bronchial cell lines⁹⁷. In contrast, a tenfold reduction should be applied for alveolar cell lines to achieve comparable particle loads with *in vivo* exposures⁹⁷.

In evaluating the toxicological dose, clearance mechanisms in the tracheobronchial and alveolar regions, as well as inherent differences in cellular sensitivity between ALI-grown cells and native lung tissue, must also be considered. Another essential consideration in ALI exposures is the deposition of gas-phase molecules. Particles smaller than 1 nm lie within the transition zone between particles and gas or vapor molecules⁹⁷. As a result, the behavior of gas-phase deposition must be more carefully considered in model calculations at this scale. Typically, gas molecules, such as formaldehyde, do not adhere to tissue surfaces upon contact unless they are highly reactive. Moreover, after prolonged exposure, gases can exert a back pressure from the tissue side, further lowering their deposition probability⁹⁷. Since oxidative stress and DNA damage have been observed following gas-phase exposures, more attention should be directed toward understanding gas-phase interactions in ALI systems. Additional experimental work in this area is needed¹⁷⁹.

4.5 ENDPOINTS/ANALYTES FOR INTEGRATING ENVIRONMENTAL AND ALI MONITORING

The lungs are particularly vulnerable to inhalation exposure from airborne particles. In recent years, significant progress has been made in developing air–liquid interface (ALI) exposure systems to evaluate the potential toxicity of airborne particles¹⁷³. These systems offer more physiologically relevant and realistic exposure conditions than traditional submerged exposure via culture medium, which can alter particle characteristics and affect cell interaction¹⁸⁰.

In the context of this thesis, three types of UFP models were generated to support toxicological investigations and better understand the mechanistic pathways underlying the biological effects of UFP characteristics. However, in real-world environments, UFP are never isolated; they exist as part of complex mixtures with other atmospheric constituents. It has been suggested that even when the toxicity of individual compounds is well characterized, their mixtures can lead to unexpected effects, such as enhanced oxidative stress, inflammation, or DNA damage.

While short-term exposures using defined, single-dose pollutant applications help assess acute toxicity, investigate long-term effects at low pollutant concentrations requires continuous exposure systems. The automated ALI exposure system was adapted for long-term experiments to address this need. In three independent experiments, human bronchial epithelial cells (Calu-3) were continuously exposed to ambient urban air from a European city for 72 hours¹⁸¹. These exposures were accompanied by comprehensive toxicological assessments and detailed physical and chemical aerosol characterization. Common air pollutants identified included Benz[a]pyrene ($\leq 3 \text{ ng/m}^3$ per 24 h) and PM_{2.5} ($\leq 12 \text{ }\mu\text{g/m}^3$ per 24 h), with a maximum particle number concentration of $4.4 \times 10^{-3} \text{ particles/m}^3$ per 24 h¹⁸¹. Ambient air exposure led to increased cytotoxicity and a non-significant reduction in cell viability. However, upregulation of the proinflammatory cytokine IL1 β and the xenobiotic metabolism genes CYP1A1 and CYP1B1 was observed, particularly in response to elevated concentrations of PAHs.

Findings from both the UFP soot model and long-term ambient exposures highlighted PAHs as key inducers of xenobiotic-metabolizing enzymes such as CYP1A1. This response was triggered by high-dose UFP soot exposures (UFP-H) and prolonged exposure to low ambient PAH concentrations. These results suggest that PAHs can serve as effective analytes for toxicological assessment in environmental monitoring.

5 SUMMARY AND OUTLOOK

Ultrafine particles (UFP) are the smallest atmospheric particulate matter associated with diseases related to air pollution. In 2021, the World Health Organization (WHO) updated its air quality recommendations, highlighting the significance of UFP monitoring as a best practice and establishing stricter goal limits for particulate matter (PM, $\leq 2.5 \mu\text{m}$). Nonetheless, there is still a lack of epidemiological studies and experimental reference values for UFP. It is not entirely understood how the physical properties of UFP contribute to their toxicity or whether the particles primarily serve as carriers of biologically reactive chemicals responsible for biological responses. Therefore, addressing these questions in toxicological testing necessitates robust methods for generating and manipulating UFP, allowing for targeted and reproducible adjustments of the physical and chemical parameters of UFP. As a result, laboratory conditions are essential for assessing these processes and their significance concerning adverse health effects. Hence, producing reliable and reproducible data on UFP is vital.

This thesis presents the production and characterization of soot UFP with similar elemental carbon cores and similar physical properties, but differing chemical constituents. The primary soot particles were generated with a Mini CAST burner at fuel-rich conditions ($\lambda=0.80$) and immediately diluted by an adjustable porous tube diluter and 10-fold fixed ejector diluters to reduce agglomeration. A catalytic stripper, followed by a multichannel activated charcoal denuder, was used to strip off volatile and semi-volatile components. Depending on the temperature of the catalytic stripper, two types of UFP soot were produced: UFP with high semi-volatile organic content (UFP-H) and UFP with low semi-volatile organic content (UFP-L). Physical characterization revealed that both samples had similar mobility diameters ($\approx 45 \text{ nm}$), particle numbers ($\approx 50 \times 10^4 / \text{cm}^3$), and mass concentrations ($\approx 100 \mu\text{g}/\text{m}^3$), along with similar equivalent black carbon concentrations ($\approx 50 \mu\text{g}/\text{m}^3$) and the same morphology. Filter samples were taken to characterize the chemical composition. Untargeted analysis and targeted quantification of polycyclic aromatic hydrocarbons were performed. In the untargeted analysis, compared to UFP-L, UFP-H exhibited a significantly higher number of PAHs with m/z 178–300, including parent and alkylated four-, five-, and six-ring PAHs. Oxygenated PAHs were observed in relatively low concentrations exclusively for UFP-H. In the targeted quantification, the PAHs in UFP-H accounted for approximately 2.5% of the total UFP mass, indicating significantly high concentrations of PAHs. Among the PAHs detected in high concentrations in UFP-H was Benzo[a]pyrene, one of the most hazardous and well-characterized PAHs in terms of toxicity. It accounted for approximately 2 mg per gram of the total mass of UFP. The generated aerosols were further assessed for biological responses in human alveolar epithelial cells at the air-liquid interface. The toxicological assessments were investigated in an Automated Exposure Station at the air-liquid interface. Toxicological assessments included cellular metabolic activity, cytotoxicity, genotoxicity, and xenobiotic metabolism. Furthermore, repeated cell exposures were enabled to produce and adjust specific UFP attributes with demonstrated reproducibility for toxicological studies. Toxicological evaluations revealed that both types of UFP similarly affected cytotoxicity and cell viability, regardless of organic load. Higher xenobiotic metabolism was observed for UFP-H, whereas reactive oxidation markers increased when semi-volatile compounds were stripped off (UFP-L). Both UFP types caused DNA strand breaks, but only the UFP-H induced DNA oxidation.

Additionally, this thesis investigated the mass deposition of UFP in the ALI system using the UFP-H and copper UFP (Cu-UFP) generated via spark discharge. The physical properties of

both UFP types were closely matched to study their deposition behavior. PAHs were used as tracers to quantify UFP-H deposition via TD-GCMS, while Cu-UFP deposition was determined using AAS. Statistical analysis (Welch's ANOVA) confirmed that deposition levels were consistent across biological exposure inserts ($p > 0.05$). Interestingly, measured UFP deposition exceeded the values predicted by conventional models, highlighting discrepancies between theoretical predictions and the behavior of the ALI system using complex aerosol particles. This highlights the need to refine ALI system deposition models to enhance deposition accuracy, particularly in the UFP size regime. The thesis also explores the use of ALI monitoring in combination with real ambient exposures and emphasizes the shift from mass-based toxicants/endpoints to more specific indicators, such as PAHs. Additionally, it highlights the increasing focus on genomics and proteomics investigations to better understand UFP toxicity.

6 REFERENCES

- (1) Spurny, K. R. On the Physics, Chemistry and Toxicology of Ultrafine Anthropogenic, Atmospheric Aerosols (UAAA): New Advances. *Toxicol. Lett.* **1998**, *96–97*, 253–261. [https://doi.org/10.1016/S0378-4274\(98\)00080-0](https://doi.org/10.1016/S0378-4274(98)00080-0).
- (2) Yue, D. L.; Hu, M.; Wu, Z. J.; Wang, Z. B.; Guo, S.; Wehner, B.; Nowak, A.; Achtert, P.; Wiedensohler, A.; Jung, J.; Kim, Y. J.; Liu, S. Characteristics of Aerosol Size Distributions and New Particle Formation in the Summer in Beijing. *J Geophys Res–Atmos* **2009**, *114*.
- (3) Hinds, William C.; Zhu, Yifang. *Aerosol Technology: Properties, Behavior, and Measurement of Airborne Particles, 3rd Edition*; Wiley, 2022.
- (4) Cai, R.; Yang, D.; Fu, Y.; Wang, X.; Li, X.; Ma, Y.; Hao, J.; Zheng, J.; Jiang, J. Aerosol Surface Area Concentration: A Governing Factor in New Particle Formation in Beijing. *Atmospheric Chem. Phys.* **2017**, *17* (20), 12327–12340. <https://doi.org/10.5194/acp-17-12327-2017>.
- (5) Wu, T.; Boor, B. E. Urban Aerosol Size Distributions: A Global Perspective. *Atmospheric Chem. Phys.* **2021**, *21* (11), 8883–8914. <https://doi.org/10.5194/acp-21-8883-2021>.
- (6) Zhang, D.; Li, Z.; Wu, H.; Wu, T.; Ren, R.; Cai, Z.; Liang, C.; Chen, L. Analysis of Aerosol Particle Number Size Distribution and Source Attribution at Three Megacities in China. *Atmos. Environ.* **2022**, *279*, 119114. <https://doi.org/10.1016/j.atmosenv.2022.119114>.
- (7) Neukirchen, C.; Meiners, T.; Bendl, J.; Zimmermann, R.; Adam, T. Automated SEM/EDX Imaging for the in-Depth Characterization of Non-Exhaust Traffic Emissions from the Munich Subway System. *Sci. Total Environ.* **2024**, *915*, 170008. <https://doi.org/10.1016/j.scitotenv.2024.170008>.
- (8) Tiitta, P.; Leskinen, A.; Hao, L.; Yli-Pirilä, P.; Kortelainen, M.; Grigonyte, J.; Tissari, J.; Lamberg, H.; Hartikainen, A.; Kuusalo, K.; Kortelainen, A.-M.; Virtanen, A.; Lehtinen, K. E. J.; Komppula, M.; Pieber, S.; Prévôt, A. S. H.; Onasch, T. B.; Worsnop, D. R.; Czech, H.; Zimmermann, R.; Jokiniemi, J.; Sippula, O. Transformation of Logwood Combustion Emissions in a Smog Chamber: Formation of Secondary Organic Aerosol and Changes in the Primary Organic Aerosol upon Daytime and Nighttime Aging. *Atmospheric Chem. Phys.* **2016**, *16* (20), 13251–13269. <https://doi.org/10.5194/acp-16-13251-2016>.
- (9) Tomasi, C.; Lupi, A. Primary and Secondary Sources of Atmospheric Aerosol. In *Atmospheric Aerosols*; 2017; pp 1–86. <https://doi.org/10.1002/9783527336449.ch1>.
- (10) J.H Seinfeld; Pandis, S. N. *Atmospheric Chemistry and Physics*; John Wiley and Sons: New York, 1998.
- (11) Kwon, H.-S.; Ryu, M. H.; Carlsten, C. Ultrafine Particles: Unique Physicochemical Properties Relevant to Health and Disease. *Exp. Mol. Med.* **2020**, *52* (3), 318–328. <https://doi.org/10.1038/s12276-020-0405-1>.
- (12) Schraufnagel, D. E. The Health Effects of Ultrafine Particles. *Exp. Mol. Med.* **2020**, *52* (3), 311–317. <https://doi.org/10.1038/s12276-020-0403-3>.
- (13) Hofman, J.; Staelens, J.; Cordell, R.; Stroobants, C.; Zikova, N.; Hama, S. M. L.; Wyche, K. P.; Kos, G. P. A.; Van Der Zee, S.; Smallbone, K. L.; Weijers, E. P.; Monks, P. S.; Roekens, E. Ultrafine Particles in Four European Urban Environments: Results from a New Continuous Long-Term Monitoring Network. *Atmos. Environ.* **2016**, *136*, 68–81. <https://doi.org/10.1016/j.atmosenv.2016.04.010>.
- (14) McCormack, M. C.; Breyse, P. N.; Hansel, N. N.; Matsui, E. C.; Tonorezos, E. S.; Curtin-Brosnan, J.; Williams, D. L.; Buckley, T. J.; Eggleston, P. A.; Diette, G. B. Common Household Activities Are Associated with Elevated Particulate Matter Concentrations in Bedrooms of Inner-City Baltimore Pre-School Children. *Environ. Res.* **2008**, *106* (2), 148–155. <https://doi.org/10.1016/j.envres.2007.08.012>.
- (15) Luo, X.; Bing, H.; Luo, Z.; Wang, Y.; Jin, L. Impacts of Atmospheric Particulate Matter Pollution on Environmental Biogeochemistry of Trace Metals in Soil-Plant System: A Review. *Environ. Pollut.* **2019**, *255*, 113138. <https://doi.org/10.1016/j.envpol.2019.113138>.

- (16) YIN, Y.; LIU, Z.; HU, B.; WANG, Y. Recent Progress on the Mechanisms of New Particle Formation and Growth in Polluted Atmospheres. *J. Tsinghua Univ. Sci. Technol.* **2022**, 62 (12), 2043–2052. <https://doi.org/10.16511/j.cnki.qhdxxb.2022.25.049>.
- (17) Makkonen, R.; Asmi, A.; Kerminen, V.-M.; Boy, M.; Arneth, A.; Hari, P.; Kulmala, M. Air Pollution Control and Decreasing New Particle Formation Lead to Strong Climate Warming. *Atmospheric Chem. Phys.* **2012**, 12 (3), 1515–1524. <https://doi.org/10.5194/acp-12-1515-2012>.
- (18) Zhao, D.; Xu, M.; Liu, G.; Ma, L.; Zhang, S.; Xiao, T.; Peng, G. Effect of Vegetation Type on Microstructure of Soil Aggregates on the Loess Plateau, China. *Agric. Ecosyst. Environ.* **2017**, 242, 1–8. <https://doi.org/10.1016/j.agee.2017.03.014>.
- (19) Junkermann, W.; Hacker, J. Unprecedented Levels of Ultrafine Particles, Major Sources, and the Hydrological Cycle. *Sci. Rep.* **2022**, 12 (1), 7410. <https://doi.org/10.1038/s41598-022-11500-5>.
- (20) Gong, J.; Zhu, T.; Hu, M.; Wu, Z.; Zhang, J. (Jim). Different Metrics (Number, Surface Area, and Volume Concentration) of Urban Particles with Varying Sizes in Relation to Fractional Exhaled Nitric Oxide (FeNO). *J. Thorac. Dis. Vol 11 No 4 April 30 2019 J. Thorac. Dis.* **2019**.
- (21) Ostro Bart; Hu Jianlin; Goldberg Debbie; Reynolds Peggy; Hertz Andrew; Bernstein Leslie; Kleeman Michael J. Associations of Mortality with Long-Term Exposures to Fine and Ultrafine Particles, Species and Sources: Results from the California Teachers Study Cohort. *Environ. Health Perspect.* **2015**, 123 (6), 549–556. <https://doi.org/10.1289/ehp.1408565>.
- (22) Lin, S.; Ryan, I.; Paul, S.; Deng, X.; Zhang, W.; Luo, G.; Dong, G.-H.; Nair, A.; Yu, F. Particle Surface Area, Ultrafine Particle Number Concentration, and Cardiovascular Hospitalizations. *Environ. Pollut.* **2022**, 310, 119795. <https://doi.org/10.1016/j.envpol.2022.119795>.
- (23) Zhang, L.; Gong, S.; Padro, J.; Barrie, L. A Size-Segregated Particle Dry Deposition Scheme for an Atmospheric Aerosol Module. *Atmos. Environ.* **2001**, 35 (3), 549–560. [https://doi.org/10.1016/S1352-2310\(00\)00326-5](https://doi.org/10.1016/S1352-2310(00)00326-5).
- (24) Manigrasso, M.; Avino, P. Fast Evolution of Urban Ultrafine Particles: Implications for Deposition Doses in the Human Respiratory System. *Atmos. Environ.* **2012**, 51, 116–123. <https://doi.org/10.1016/j.atmosenv.2012.01.039>.
- (25) Kumar, P.; Wiedensohler, A.; Birmili, W.; Quincey, P.; Hallquist, M. Chapter 15 - Ultrafine Particles Pollution and Measurements. In *Comprehensive Analytical Chemistry*; de la Guardia, M., Armenta, S., Eds.; Elsevier, 2016; Vol. 73, pp 369–390. <https://doi.org/10.1016/bs.coac.2016.04.004>.
- (26) Kumar, P.; Patton, A. P.; Durant, J. L.; Frey, H. C. A Review of Factors Impacting Exposure to PM_{2.5}, Ultrafine Particles and Black Carbon in Asian Transport Microenvironments. *Atmos. Environ.* **2018**, 187, 301–316. <https://doi.org/10.1016/j.atmosenv.2018.05.046>.
- (27) Abdel-Shafy, H. I.; Mansour, M. S. M. A Review on Polycyclic Aromatic Hydrocarbons: Source, Environmental Impact, Effect on Human Health and Remediation. *Egypt. J. Pet.* **2016**, 25 (1), 107–123. <https://doi.org/10.1016/j.ejpe.2015.03.011>.
- (28) Kumar, P.; Ketzel, M.; Vardoulakis, S.; Pirjola, L.; Britter, R. Dynamics and Dispersion Modelling of Nanoparticles from Road Traffic in the Urban Atmospheric Environment—A Review. *J. Aerosol Sci.* **2011**, 42 (9), 580–603. <https://doi.org/10.1016/j.jaerosci.2011.06.001>.
- (29) Lu, S.; Hao, X.; Liu, D.; Wang, Q.; Zhang, W.; Liu, P.; Zhang, R.; Yu, S.; Pan, R.; Wu, M.; Yonemochi, S.; Wang, Q. Mineralogical Characterization of Ambient Fine/Ultrafine Particles Emitted from Xuanwei C1 Coal Combustion. *Atmospheric Res.* **2016**, 169, 17–23. <https://doi.org/10.1016/j.atmosres.2015.09.020>.
- (30) Moreno-Ríos, A. L.; Tejeda-Benítez, L. P.; Bustillo-Lecompte, C. F. Sources, Characteristics, Toxicity, and Control of Ultrafine Particles: An Overview. *Geosci. Front.* **2022**, 13 (1), 101147. <https://doi.org/10.1016/j.gsf.2021.101147>.

- (31) Kelly, F. J.; Fussell, J. C. Size, Source and Chemical Composition as Determinants of Toxicity Attributable to Ambient Particulate Matter. *Atmos. Environ.* **2012**, *60*, 504–526. <https://doi.org/10.1016/j.atmosenv.2012.06.039>.
- (32) Gasparotto, J.; Da Boit Martinello, K. Coal as an Energy Source and Its Impacts on Human Health. *Coal Energy Environ. Impacts* **2021**, *2* (2), 113–120. <https://doi.org/10.1016/j.engeos.2020.07.003>.
- (33) Ribeiro, J.; Flores, D. Occurrence, Leaching, and Mobility of Major and Trace Elements in a Coal Mining Waste Dump: The Case of Douro Coalfield, Portugal. *Coal Energy Environ. Impacts* **2021**, *2* (2), 121–128. <https://doi.org/10.1016/j.engeos.2020.09.005>.
- (34) Silva, L. F. O.; DaBoit, K.; Sampaio, C. H.; Jasper, A.; Andrade, M. L.; Kostova, I. J.; Waanders, F. B.; Henke, K. R.; Hower, J. C. The Occurrence of Hazardous Volatile Elements and Nanoparticles in Bulgarian Coal Fly Ashes and the Effect on Human Health Exposure. *Sci. Total Environ.* **2012**, *416*, 513–526. <https://doi.org/10.1016/j.scitotenv.2011.11.012>.
- (35) Zhang, Y.; Dong, S.; Wang, H.; Tao, S.; Kiyama, R. Biological Impact of Environmental Polycyclic Aromatic Hydrocarbons (ePAHs) as Endocrine Disruptors. *Environ. Pollut.* **2016**, *213*, 809–824. <https://doi.org/10.1016/j.envpol.2016.03.050>.
- (36) Lawal, A. T. Polycyclic Aromatic Hydrocarbons. A Review. *Cogent Environ. Sci.* **2017**, *3* (1), 1339841. <https://doi.org/10.1080/23311843.2017.1339841>.
- (37) Crone, T. J.; Tolstoy, M. Magnitude of the 2010 Gulf of Mexico Oil Leak. *Science* **2010**, *330* (6004), 634–634. <https://doi.org/10.1126/science.1195840>.
- (38) Abbas, I.; Badran, G.; Verdin, A.; Ledoux, F.; Roumié, M.; Courcot, D.; Garçon, G. Polycyclic Aromatic Hydrocarbon Derivatives in Airborne Particulate Matter: Sources, Analysis and Toxicity. *Environ. Chem. Lett.* **2018**, *16* (2), 439–475. <https://doi.org/10.1007/s10311-017-0697-0>.
- (39) Song, H.; Zhang, Y.; Luo, M.; Gu, J.; Wu, M.; Xu, D.; Xu, G.; Ma, L. Seasonal Variation, Sources and Health Risk Assessment of Polycyclic Aromatic Hydrocarbons in Different Particle Fractions of PM_{2.5} in Beijing, China. *Atmospheric Pollut. Res.* **2019**, *10* (1), 105–114. <https://doi.org/10.1016/j.apr.2018.06.012>.
- (40) Silva, L. F. O.; Milanés, C.; Pinto, D.; Ramirez, O.; Lima, B. D. Multiple Hazardous Elements in Nanoparticulate Matter from a Caribbean Industrialized Atmosphere. *Chemosphere* **2020**, *239*, 124776. <https://doi.org/10.1016/j.chemosphere.2019.124776>.
- (41) Silva, L. F. O.; Pinto, D.; Neckel, A.; Oliveira, M. L. S.; Sampaio, C. H. Atmospheric Nanocompounds on Lanzarote Island: Vehicular Exhaust and Igneous Geologic Formation Interactions. *Chemosphere* **2020**, *254*, 126822. <https://doi.org/10.1016/j.chemosphere.2020.126822>.
- (42) Sanderson, P.; Delgado-Saborit, J. M.; Harrison, R. M. A Review of Chemical and Physical Characterisation of Atmospheric Metallic Nanoparticles. *Atmos. Environ.* **2014**, *94*, 353–365. <https://doi.org/10.1016/j.atmosenv.2014.05.023>.
- (43) Miazgowiec, A.; Krennhuber, K.; Lanzerstorfer, C. Metals Concentrations in Road Dust from High Traffic and Low Traffic Area: A Size Dependent Comparison. *Int. J. Environ. Sci. Technol.* **2020**, *17* (7), 3365–3372. <https://doi.org/10.1007/s13762-020-02667-3>.
- (44) Ntziachristos, L.; Ning, Z.; Geller, M. D.; Sheesley, R. J.; Schauer, J. J.; Sioutas, C. Fine, Ultrafine and Nanoparticle Trace Element Compositions near a Major Freeway with a High Heavy-Duty Diesel Fraction. *Atmos. Environ.* **2007**, *41* (27), 5684–5696. <https://doi.org/10.1016/j.atmosenv.2007.02.043>.
- (45) Moreno, T.; Querol, X.; Martins, V.; Minguillón, M. C.; Reche, C.; Ku, L. H.; Eun, H. R.; Ahn, K. H.; Capdevila, M.; de Miguel, E. Formation and Alteration of Airborne Particles in the Subway Environment. *Environ. Sci. Process. Impacts* **2017**, *19* (1), 59–64. <https://doi.org/10.1039/C6EM00576D>.
- (46) Leikauf, G. D.; Kim, S.-H.; Jang, A.-S. Mechanisms of Ultrafine Particle-Induced Respiratory Health Effects. *Exp. Mol. Med.* **2020**, *52* (3), 329–337. <https://doi.org/10.1038/s12276-020-0394-0>.
- (47) Vallabani, N. V. S.; Gruzieva, O.; Elihn, K.; Juárez-Facio, A. T.; Steimer, S. S.; Kuhn, J.; Silvergren, S.; Portugal, J.; Piña, B.; Olofsson, U.; Johansson, C.; Karlsson, H. L.

- Toxicity and Health Effects of Ultrafine Particles: Towards an Understanding of the Relative Impacts of Different Transport Modes. *Environ. Res.* **2023**, *231*, 116186. <https://doi.org/10.1016/j.envres.2023.116186>.
- (48) Hoffmann, B.; Ogurtsova, K. Adding Pieces to the Puzzle: Ultrafine Particles and Lung Cancer. *Am. J. Respir. Crit. Care Med.* **2024**, *209* (3), 241–242. <https://doi.org/10.1164/rccm.202311-2098ED>.
- (49) Jones, R. R.; Fisher, J. A.; Hasheminassab, S.; Kaufman, J. D.; Freedman, N. D.; Ward, M. H.; Sioutas, C.; Vermeulen, R.; Hoek, G.; Silverman, D. T. Outdoor Ultrafine Particulate Matter and Risk of Lung Cancer in Southern California. *Am. J. Respir. Crit. Care Med.* **2024**, *209* (3), 307–315. <https://doi.org/10.1164/rccm.202305-0902OC>.
- (50) Wu, A. H.; Fruin, S.; Larson, T. V.; Tseng, C.-C.; Wu, J.; Yang, J.; Jain, J.; Shariff-Marco, S.; Inamdar, P. P.; Setiawan, V. W.; Porcel, J.; Stram, D. O.; Le Marchand, L.; Ritz, B.; Cheng, I. Association between Airport-Related Ultrafine Particles and Risk of Malignant Brain Cancer: A Multiethnic Cohort Study. *Cancer Res.* **2021**, *81* (16), 4360–4369. <https://doi.org/10.1158/0008-5472.CAN-21-1138>.
- (51) Jiang, Y.; Zhu, X.; Shen, Y.; He, Y.; Fan, H.; Xu, X.; Zhou, L.; Zhu, Y.; Xue, X.; Zhang, Q.; Du, X.; Zhang, L.; Zhang, Y.; Liu, C.; Niu, Y.; Cai, J.; Kan, H.; Chen, R. Mechanistic Insights into Cardiovascular Effects of Ultrafine Particle Exposure: A Longitudinal Panel Study. *Environ. Int.* **2024**, *187*, 108714. <https://doi.org/10.1016/j.envint.2024.108714>.
- (52) Downward George S.; van Nunen Erik J.H.M.; Kerckhoffs Jules; Vineis Paolo; Brunekreef Bert; Boer Jolanda M.A.; Messier Kyle P.; Roy Ananya; Verschuren W. Monique M.; van der Schouw Yvonne T.; Sluijs Ivonne; Gulliver John; Hoek Gerard; Vermeulen Roel. Long-Term Exposure to Ultrafine Particles and Incidence of Cardiovascular and Cerebrovascular Disease in a Prospective Study of a Dutch Cohort. *Environ. Health Perspect.* *126* (12), 127007. <https://doi.org/10.1289/EHP3047>.
- (53) Doiron, D.; de Hoogh, K.; Probst-Hensch, N.; Fortier, I.; Cai, Y.; De Matteis, S.; Hansell, A. L. Air Pollution, Lung Function and COPD: Results from the Population-Based UK Biobank Study. *Eur. Respir. J.* **2019**, *54* (1), 1802140. <https://doi.org/10.1183/13993003.02140-2018>.
- (54) Hopke, P. K.; Croft, D.; Zhang, W.; Lin, S.; Masiol, M.; Squizzato, S.; Thurston, S. W.; van Wijngaarden, E.; Utell, M. J.; Rich, D. Q. Changes in the Acute Response of Respiratory Diseases to PM_{2.5} in New York State from 2005 to 2016. *Sci. Total Environ.* **2019**, *677*, 328–339. <https://doi.org/10.1016/j.scitotenv.2019.04.357>.
- (55) Schwarze, P. E.; Øvreivik, J.; Hetland, R. B.; Becher, R.; Cassee, F. R.; Låg, M.; Løvik, M.; Dybing, E.; Refsnes, M. Importance of Size and Composition of Particles for Effects on Cells In Vitro. *Inhal. Toxicol.* **2007**, *19* (sup1), 17–22. <https://doi.org/10.1080/08958370701490445>.
- (56) Juarez-Facio, A. T.; Castilla, C.; Corbière, C.; Lavanant, H.; Afonso, C.; Morin, C.; Merlet-Machour, N.; Chevalier, L.; Vaugeois, J.-M.; Yon, J.; Monteil, C. Development of a Standardized in Vitro Approach to Evaluate Microphysical, Chemical, and Toxicological Properties of Combustion-Derived Fine and Ultrafine Particles. *J. Environ. Sci.* **2022**, *113*, 104–117. <https://doi.org/10.1016/j.jes.2021.06.001>.
- (57) Geiser, M.; Kreyling, W. G. Deposition and Biokinetics of Inhaled Nanoparticles. *Part. Fibre Toxicol.* **2010**, *7* (1), 2. <https://doi.org/10.1186/1743-8977-7-2>.
- (58) Pacheco-Blandino, I.; Vanner, R.; Buzea, C. Toxicity of Nanoparticles. In *Toxicity of Building Materials*; 2012; pp 427–475. <https://doi.org/10.1533/9780857096357.427>.
- (59) da Costa e Oliveira, J. R.; Base, L. H.; de Abreu, L. C.; Filho, C. F.; Ferreira, C.; Morawska, L. Ultrafine Particles and Children's Health: Literature Review. *Paediatr. Respir. Rev.* **2019**, *32*, 73–81. <https://doi.org/10.1016/j.prrv.2019.06.003>.
- (60) Martins, V.; Correia, C.; Cunha-Lopes, I.; Faria, T.; Diapouli, E.; Manousakas, M. I.; Eleftheriadis, K.; Almeida, S. M. Chemical Characterisation of Particulate Matter in Urban Transport Modes. *J. Environ. Sci.* **2021**, *100*, 51–61. <https://doi.org/10.1016/j.jes.2020.07.008>.
- (61) Zhang, Y.; Tu, B.; Jiang, X.; Xu, G.; Liu, X.; Tang, Q.; Bai, L.; Meng, P.; Zhang, L.; Qin, X.; Zou, Z.; Chen, C. Exposure to Carbon Black Nanoparticles during Pregnancy

- Persistently Damages the Cerebrovascular Function in Female Mice. *Toxicology* **2019**, *422*, 44–52. <https://doi.org/10.1016/j.tox.2019.04.014>.
- (62) Wahlang, B.; Jin, J.; Beier, J. I.; Hardesty, J. E.; Daly, E. F.; Schnegelberger, R. D.; Falkner, K. C.; Prough, R. A.; Kirpich, I. A.; Cave, M. C. Mechanisms of Environmental Contributions to Fatty Liver Disease. *Curr. Environ. Health Rep.* **2019**, *6* (3), 80–94. <https://doi.org/10.1007/s40572-019-00232-w>.
- (63) Hakkarainen, H.; Salo, L.; Mikkonen, S.; Saarikoski, S.; Aurela, M.; Teinilä, K.; Ihalainen, M.; Martikainen, S.; Marjanen, P.; Lepistö, T.; Kuittinen, N.; Saarnio, K.; Aakko-Saksa, P.; Pfeiffer, T. V.; Timonen, H.; Rönkkö, T.; Jalava, P. I. Black Carbon Toxicity Dependence on Particle Coating: Measurements with a Novel Cell Exposure Method. *Sci. Total Environ.* **2022**, *838*, 156543. <https://doi.org/10.1016/j.scitotenv.2022.156543>.
- (64) Chen, X.-C.; Cao, J.-J.; Ward, T. J.; Tian, L.-W.; Ning, Z.; Gali, N. K.; Aquilina, N. J.; Yim, S. H.-L.; Qu, L.; Ho, K.-F. Characteristics and Toxicological Effects of Commuter Exposure to Black Carbon and Metal Components of Fine Particles (PM_{2.5}) in Hong Kong. *Sci. Total Environ.* **2020**, *742*, 140501. <https://doi.org/10.1016/j.scitotenv.2020.140501>.
- (65) Lin, T.-C.; Chiueh, P.-T.; Hsiao, T.-C. Challenges in Observation of Ultrafine Particles: Addressing Estimation Miscalculations and the Necessity of Temporal Trends. *Environ. Sci. Technol.* **2025**, *59* (1), 565–577. <https://doi.org/10.1021/acs.est.4c07460>.
- (66) Wilson, J.; Pöschl, U.; Shiraiwa, M.; Berkemeier, T. Non-Equilibrium Interplay between Gas–Particle Partitioning and Multiphase Chemical Reactions of Semi-Volatile Compounds: Mechanistic Insights and Practical Implications for Atmospheric Modeling of Polycyclic Aromatic Hydrocarbons. *Atmospheric Chem. Phys.* **2021**, *21* (8), 6175–6198. <https://doi.org/10.5194/acp-21-6175-2021>.
- (67) Zoller, J.; Gulden, J.; Meyer, J.; Dittler, A. Loss of Nanoparticles in a Particulate Matter Sampling System Applied for Environmental Ultrafine Particle Measurements. *Aerosol Sci. Eng.* **2020**, *4* (2), 50–63. <https://doi.org/10.1007/s41810-020-00054-6>.
- (68) Wallace, L.; Fang, W.; Reed, C. Ultrafine Particles from 2 Nm to 64 Nm Generated by a Gas Stove and Electric Toaster Oven: Size-Resolved Coagulation, Deposition, and Emission Rates; Indoor Air 2008, Copenhagen, 1, DK, 2008.
- (69) Kumar, P.; Kalaiarasan, G.; Porter, A. E.; Pinna, A.; Klosowski, M. M.; Demokritou, P.; Chung, K. F.; Pain, C.; Arvind, D. K.; Arcucci, R.; Adcock, I. M.; Dillway, C. An Overview of Methods of Fine and Ultrafine Particle Collection for Physicochemical Characterisation and Toxicity Assessments. *Sci. Total Environ.* **2021**, *756*, 143553. <https://doi.org/10.1016/j.scitotenv.2020.143553>.
- (70) *Integrated Science Assessment (ISA) for Particulate Matter*; Center for Public Health and Environmental Assessment: USA, 2022. <https://www.epa.gov/isa/integrated-science-assessment-isa-particulate-matter#hero>.
- (71) Faccinetto, A.; Irimiea, C.; Minutolo, P.; Commodo, M.; D’Anna, A.; Nuns, N.; Carpentier, Y.; Pirim, C.; Desgroux, P.; Focsa, C.; Mercier, X. Evidence on the Formation of Dimers of Polycyclic Aromatic Hydrocarbons in a Laminar Diffusion Flame. *Commun. Chem.* **2020**, *3* (1), 112. <https://doi.org/10.1038/s42004-020-00357-2>.
- (72) Sabbah, H.; Commodo, M.; Picca, F.; De Falco, G.; Minutolo, P.; D’Anna, A.; Joblin, C. Molecular Content of Nascent Soot: Family Characterization Using Two-Step Laser Desorption Laser Ionization Mass Spectrometry. *Proc. Combust. Inst.* **2021**, *38* (1), 1241–1248. <https://doi.org/10.1016/j.proci.2020.09.022>.
- (73) Michelsen, H. A. Effects of Maturity and Temperature on Soot Density and Specific Heat. *Proc. Combust. Inst.* **2021**, *38* (1), 1197–1205. <https://doi.org/10.1016/j.proci.2020.06.383>.
- (74) Liu, C.; Singh, A. V.; Saggese, C.; Tang, Q.; Chen, D.; Wan, K.; Vinciguerra, M.; Commodo, M.; De Falco, G.; Minutolo, P.; D’Anna, A.; Wang, H. Flame-Formed Carbon Nanoparticles Exhibit Quantum Dot Behaviors. *Proc. Natl. Acad. Sci.* **2019**, *116* (26), 12692–12697. <https://doi.org/10.1073/pnas.1900205116>.
- (75) Tabrizi, N. S.; Ullmann, M.; Vons, V. A.; Lafont, U.; Schmidt-Ott, A. Generation of Nanoparticles by Spark Discharge. *J. Nanoparticle Res.* **2009**, *11* (2), 315–332. <https://doi.org/10.1007/s11051-008-9407-y>.

- (76) Meuller, B. O.; Messing, M. E.; Engberg, D. L. J.; Jansson, A. M.; Johansson, L. I. M.; Norlén, S. M.; Tureson, N.; Deppert, K. Review of Spark Discharge Generators for Production of Nanoparticle Aerosols. *Aerosol Sci. Technol.* **2012**, *46* (11), 1256–1270. <https://doi.org/10.1080/02786826.2012.705448>.
- (77) Efimov, A. A.; Arsenov, P. V.; Borisov, V. I.; Buchnev, A. I.; Lizunova, A. A.; Korniyushin, D. V.; Tikhonov, S. S.; Musaev, A. G.; Urazov, M. N.; Shcherbakov, M. I.; Spirin, D. V.; Ivanov, V. V. Synthesis of Nanoparticles by Spark Discharge as a Facile and Versatile Technique of Preparing Highly Conductive Pt Nano-Ink for Printed Electronics. *Nanomaterials* **2021**, *11* (1). <https://doi.org/10.3390/nano11010234>.
- (78) Giannakopoulos, K.; Lasithiotakis, M.; Karakasis, C.; Gini, M.; Gardelis, S.; Karakasiliotis, I.; Mouti, N.; Xesfyngi, Y.; Manolis, G. K.; Georgoutsou-Spyridonos, M.; Dimitriou, M.; Eleftheriadis, K. Spark Discharge Aerosol-Generated Copper-Based Nanoparticles: Structural & Optical Properties; Application on the Antiviral (SARS-CoV-2) and Antibacterial Improvement of Face Masks. *ChemPlusChem* **2024**, *89* (8), e202400194. <https://doi.org/10.1002/cplu.202400194>.
- (79) Chae, S.; Lee, D.; Kim, M.-C.; Kim, D. S.; Choi, M. Wire-in-Hole-Type Spark Discharge Generator for Long-Time Consistent Generation of Unagglomerated Nanoparticles. *Aerosol Sci. Technol.* **2015**, *49* (7), 463–471. <https://doi.org/10.1080/02786826.2015.1045444>.
- (80) Ajtai, T.; Kohut, A.; Raffai, P.; Szabó, G.; Bozóki, Z. Controlled Laboratory Generation of Atmospheric Black Carbon Using Laser Excitation-Based Soot Generator: From Basic Principles to Application Perspectives: A Review. *Atmosphere* **2022**, *13* (9). <https://doi.org/10.3390/atmos13091366>.
- (81) Ajtai, T.; Utry, N.; Pintér, M.; Kiss-Albert, G.; Puskás, R.; Tápai, Cs.; Kecskeméti, G.; Smausz, T.; Hopp, B.; Bozóki, Z.; Kónya, Z.; Szabó, G. Microphysical Properties of Carbonaceous Aerosol Particles Generated by Laser Ablation of a Graphite Target. *Atmospheric Meas. Tech.* **2015**, *8* (3), 1207–1215. <https://doi.org/10.5194/amt-8-1207-2015>.
- (82) *Compendium of Methods for the Determination of Inorganic Compounds in Ambient Air*; U.S. Environmental Protection Agency (EPA), 1978; pp 1–52. <https://nepis.epa.gov/Exe/ZyNET.exe/9100C5O9.TXT?ZyActionD=ZyDocument&Client=EPA&Index=1976+Thru+1980&Docs=&Query=&Time=&EndTime=&SearchMethod=1&TocRestrict=n&Toc=&TocEntry=&QField=&QFieldYear=&QFieldMonth=&QFieldDay=&IntQFieldOp=0&ExtQFieldOp=0&XmlQuery=&File=D%3A%5Czyfiles%5CIndex%20Data%5C76thru80%5CTxt%5C00000012%5C9100C5O9.txt&User=ANONYMOUS&Password=anonymous&SortMethod=h%7C-&MaximumDocuments=1&FuzzyDegree=0&ImageQuality=r75g8/r75g8/x150y150g16/i425&Display=hpfr&DefSeekPage=x&SearchBack=ZyActionL&Back=ZyActionS&BackDesc=Results%20page&MaximumPages=1&ZyEntry=1&SeekPage=x&ZyPURL>.
- (83) Li, N.; Georas, S.; Alexis, N.; Fritz, P.; Xia, T.; Williams, M. A.; Horner, E.; Nel, A. A Work Group Report on Ultrafine Particles (American Academy of Allergy, Asthma & Immunology): Why Ambient Ultrafine and Engineered Nanoparticles Should Receive Special Attention for Possible Adverse Health Outcomes in Human Subjects. *J. Allergy Clin. Immunol.* **2016**, *138* (2), 386.
- (84) Ohlwein, S.; Kappeler, R.; Kutlar Joss, M.; Künzli, N.; Hoffmann, B. Health Effects of Ultrafine Particles: A Systematic Literature Review Update of Epidemiological Evidence. *Int. J. Public Health* **2019**, *64* (4), 547–559. <https://doi.org/10.1007/s00038-019-01202-7>.
- (85) Long, E.; Schwartz, C.; Carlsten, C. Controlled Human Exposure to Diesel Exhaust: A Method for Understanding Health Effects of Traffic-Related Air Pollution. *Part. Fibre Toxicol.* **2022**, *19* (1), 15. <https://doi.org/10.1186/s12989-022-00454-1>.
- (86) Pedklang, N.; Navasumrit, P.; Chompoobut, C.; Promvijit, J.; Hunsonti, P.; Ruchirawat, M. Effects of Particulate Air Pollution on BPDE-DNA Adducts, Telomere Length, and Mitochondrial DNA Copy Number in Human Exhaled Breath Condensate and BEAS-2B Cells. *Int. J. Hyg. Environ. Health* **2025**, *263*, 114488. <https://doi.org/10.1016/j.ijheh.2024.114488>.

- (87) Araujo, J. A.; Barajas, B.; Kleinman, M.; Wang, X.; Bennett, B. J.; Gong, K. W.; Navab, M.; Harkema, J.; Sioutas, C.; Lusic, A. J.; Nel, A. E. Ambient Particulate Pollutants in the Ultrafine Range Promote Early Atherosclerosis and Systemic Oxidative Stress. *Circ. Res.* **2008**, *102* (5), 589–596. <https://doi.org/10.1161/CIRCRESAHA.107.164970>.
- (88) Rossi, S.; Buccarello, A.; Caffarra Malvezzi, C.; Pinelli, S.; Alinovi, R.; Guerrero Gerboles, A.; Rozzi, G.; Leonardi, F.; Bollati, V.; De Palma, G.; Lagonegro, P.; Rossi, F.; Lottici, P. P.; Poli, D.; Statello, R.; Macchi, E.; Miragoli, M. Exposure to Nanoparticles Derived from Diesel Particulate Filter Equipped Engine Increases Vulnerability to Arrhythmia in Rat Hearts. *Environ. Pollut.* **2021**, *284*, 117163. <https://doi.org/10.1016/j.envpol.2021.117163>.
- (89) Seagrave, J.; McDonald, J. D.; Mauderly, J. L. In Vitro versus in Vivo Exposure to Combustion Emissions. *Exp. Toxicol. Pathol.* **2005**, *57*, 233–238. <https://doi.org/10.1016/j.etp.2005.05.011>.
- (90) Bessa, M. J.; Brandão, F.; Fokkens, P. H. B.; Leseman, D. L. A. C.; Boere, A. J. F.; Cassee, F. R.; Salmatouidis, A.; Viana, M.; Vulpoi, A.; Simon, S.; Monfort, E.; Teixeira, J. P.; Fraga, S. In Vitro Toxicity of Industrially Relevant Engineered Nanoparticles in Human Alveolar Epithelial Cells: Air–Liquid Interface versus Submerged Cultures. *Nanomaterials* **2021**, *11* (12). <https://doi.org/10.3390/nano11123225>.
- (91) Bierkandt, F. S.; Leibrock, L.; Wagener, S.; Laux, P.; Luch, A. The Impact of Nanomaterial Characteristics on Inhalation Toxicity. *Toxicol. Res.* **2018**, *7* (3), 321–346. <https://doi.org/10.1039/c7tx00242d>.
- (92) Upadhyay, S.; Palmberg, L. Air-Liquid Interface: Relevant In Vitro Models for Investigating Air Pollutant-Induced Pulmonary Toxicity. *Toxicol. Sci.* **2018**, *164* (1), 21–30. <https://doi.org/10.1093/toxsci/kfy053>.
- (93) Singh, A. V.; Romeo, A.; Scott, K.; Wagener, S.; Leibrock, L.; Laux, P.; Luch, A.; Kerkar, P.; Balakrishnan, S.; Dakua, S. P.; Park, B.-W. Emerging Technologies for In Vitro Inhalation Toxicology. *Adv. Healthc. Mater.* **2021**, *10* (18), 2100633. <https://doi.org/10.1002/adhm.202100633>.
- (94) Paur, H.-R.; Cassee, F. R.; Teeguarden, J.; Fissan, H.; Diabate, S.; Aufderheide, M.; Kreyling, W. G.; Hänninen, O.; Kasper, G.; Riediker, M.; Rothen-Rutishauser, B.; Schmid, O. In-Vitro Cell Exposure Studies for the Assessment of Nanoparticle Toxicity in the Lung—A Dialog between Aerosol Science and Biology. *J. Aerosol Sci.* **2011**, *42* (10), 668–692. <https://doi.org/10.1016/j.jaerosci.2011.06.005>.
- (95) Thorne, D.; Adamson, J. A Review of in Vitro Cigarette Smoke Exposure Systems. *Exp. Toxicol. Pathol.* **2013**, *65* (7), 1183–1193. <https://doi.org/10.1016/j.etp.2013.06.001>.
- (96) Lucci, F.; Castro, N. D.; Rostami, A. A.; Oldham, M. J.; Hoeng, J.; Pithawalla, Y. B.; Kuczaj, A. K. Characterization and Modeling of Aerosol Deposition in Vitrocell® Exposure Systems - Exposure Well Chamber Deposition Efficiency. *J. Aerosol Sci.* **2018**, *123*, 141–160. <https://doi.org/10.1016/j.jaerosci.2018.06.015>.
- (97) Karg, E. W.; Ferron, G. A.; Bauer, S.; Di Bucchianico, S.; Zimmermann, R. Is the Particle Deposition in a Cell Exposure Facility Comparable to the Lungs? A Computer Model Approach. *Aerosol Sci. Technol.* **2020**, *54* (6), 668–684. <https://doi.org/10.1080/02786826.2020.1724868>.
- (98) Findeisen, W. Über Das Absetzen Kleiner, in Der Luft Suspendierter Teilchen in Der Menschlichen Lunge Bei Der Atmung. *Pflüg. Arch. Für Gesamte Physiol. Menschen Tiere* **1935**, *236* (1), 367–379. <https://doi.org/10.1007/BF01752351>.
- (99) Hofmann, W. Modelling Inhaled Particle Deposition in the Human Lung—A Review. *J. Aerosol Sci.* **2011**, *42* (10), 693–724. <https://doi.org/10.1016/j.jaerosci.2011.05.007>.
- (100) Mathis, C.; Poussin, C.; Weisensee, D.; Gebel, S.; Hengstermann, A.; Sewer, A.; Belcastro, V.; Xiang, Y.; Ansari, S.; Wagner, S.; Hoeng, J.; Peitsch, M. C. Human Bronchial Epithelial Cells Exposed in Vitro to Cigarette Smoke at the Air-Liquid Interface Resemble Bronchial Epithelium from Human Smokers. *Am. J. Physiol.-Lung Cell. Mol. Physiol.* **2013**, *304* (7), L489–L503. <https://doi.org/10.1152/ajplung.00181.2012>.

- (101) Hangal, S.; Willeke, K. Aspiration Efficiency: Unified Model for All Forward Sampling Angles. *Environ. Sci. Technol.* **1990**, *24* (5), 688–691. <https://doi.org/10.1021/es00075a012>.
- (102) Comouth, A.; Saathoff, H.; Naumann, K.-H.; Muelhopt, S.; Paur, H.-R.; Leisner, T. Modelling and Measurement of Particle Deposition for Cell Exposure at the Air–Liquid Interface. *J. Aerosol Sci.* **2013**, *63*, 103–114. <https://doi.org/10.1016/j.jaerosci.2013.04.009>.
- (103) Majeed, S.; Frentzel, S.; Wagner, S.; Kuehn, D.; Leroy, P.; Guy, P. A.; Knorr, A.; Hoeng, J.; Peitsch, M. C. Characterization of the Vitrocell® 24/48 in Vitroaerosol Exposure System Using Mainstream Cigarette Smoke. *Chem. Cent. J.* **2014**, *8* (1), 62. <https://doi.org/10.1186/s13065-014-0062-3>.
- (104) Kuczaj, A. K.; Nordlund, M.; Jayaraju, S.; Komen, E.; Krebs, T.; Peitsch, M. C.; Hoeng, J. Aerosol Flow in the Vitrocell 24/48 Exposure System: Flow Mixing and Aerosol Coalescence. *Appl. Vitro Toxicol.* **2016**, *2* (3), 165–174. <https://doi.org/10.1089/aivt.2016.0009>.
- (105) Ritter, D.; Knebel, J.; Niehof, M.; Loinaz, I.; Marradi, M.; Gracia, R.; te Welscher, Y.; van Nostrum, C. F.; Falciani, C.; Pini, A.; Strandh, M.; Hansen, T. In Vitro Inhalation Cytotoxicity Testing of Therapeutic Nanosystems for Pulmonary Infection. *Toxicol. In Vitro* **2020**, *63*, 104714. <https://doi.org/10.1016/j.tiv.2019.104714>.
- (106) Lenz, A.-G.; Stoeger, T.; Cei, D.; Schmidmeir, M.; Semren, N.; Burgstaller, G.; Lentner, B.; Eickelberg, O.; Meiners, S.; Schmid, O. Efficient Bioactive Delivery of Aerosolized Drugs to Human Pulmonary Epithelial Cells Cultured in Air–Liquid Interface Conditions. *Am. J. Respir. Cell Mol. Biol.* **2014**, *51* (4), 526–535. <https://doi.org/10.1165/rcmb.2013-0479OC>.
- (107) Fujitani, Y.; Sugaya, Y.; Hashiguchi, M.; Furuyama, A.; Hirano, S.; Takami, A. Particle Deposition Efficiency at Air–Liquid Interface of a Cell Exposure Chamber. *J. Aerosol Sci.* **2015**, *81*, 90–99. <https://doi.org/10.1016/j.jaerosci.2014.10.012>.
- (108) Steiner, S.; Majeed, S.; Kratzer, G.; Vuillaume, G.; Hoeng, J.; Frentzel, S. Characterization of the Vitrocell® 24/48 Aerosol Exposure System for Its Use in Exposures to Liquid Aerosols. *Toxicol. In Vitro* **2017**, *42*, 263–272. <https://doi.org/10.1016/j.tiv.2017.04.021>.
- (109) Adamson, J.; Thorne, D.; Zainuddin, B.; Baxter, A.; McAughey, J.; Gaça, M. Application of Dosimetry Tools for the Assessment of E-Cigarette Aerosol and Cigarette Smoke Generated on Two Different in Vitro Exposure Systems. *Chem. Cent. J.* **2016**, *10* (1), 74. <https://doi.org/10.1186/s13065-016-0221-9>.
- (110) Secondo, L. E.; Liu, N. J.; Lewinski, N. A. Methodological Considerations When Conducting in Vitro, Air–Liquid Interface Exposures to Engineered Nanoparticle Aerosols. *Crit. Rev. Toxicol.* **2017**, *47* (3), 225–262. <https://doi.org/10.1080/10408444.2016.1223015>.
- (111) Tippe, A.; Heinzmann, U.; Roth, C. Deposition of Fine and Ultrafine Aerosol Particles during Exposure at the Air/Cell Interface. *J. Aerosol Sci.* **2002**, *33* (2), 207–218. [https://doi.org/10.1016/S0021-8502\(01\)00158-6](https://doi.org/10.1016/S0021-8502(01)00158-6).
- (112) Jing, L. Standard Combustion Aerosol Generator (SCAG) for Calibration Purposes; ETH Hönggerberg Zürich, 1999.
- (113) CONSTANTINE, M. M.; RICHARD, A. D. Comparison of Soot Growth and Oxidation in Smoking and Non–Smoking Ethylene Diffusion Flames. *Combust. Sci. Technol.* **1989**, *66* (1–3), 1–16. <https://doi.org/10.1080/00102208908947136>.
- (114) Abdul-Khalek, Imad S.; Kittelson, David B. Real Time Measurement of Volatile and Solid Exhaust Particles Using a Catalytic Stripper. In *International Congress & Exposition*; SAE International, 1995. <https://doi.org/10.4271/950236>.
- (115) Khalek, Imad A. Sampling System for Solid and Volatile Exhaust Particle Size, Number, and Mass Emissions. In *SAE World Congress & Exhibition*; SAE International, 2007. <https://doi.org/10.4271/2007-01-0307>.

- (116) Stenitzer, Martin. Nano Particle Formation in the Exhaust of Internal Combustion Engines. Diploma Thesis, Technische Universität Wien, TU Wien, Österreich, 2003. http://purl.org/coar/resource_type/c_bdcc.
- (117) Zheng, Z.; Johnson, K. C.; Liu, Z.; Durbin, T. D.; Hu, S.; Huai, T.; Kittelson, D. B.; Jung, H. S. Investigation of Solid Particle Number Measurement: Existence and Nature of Sub-23nm Particles under PMP Methodology. *J. Aerosol Sci.* **2011**, *42* (12), 883–897. <https://doi.org/10.1016/j.jaerosci.2011.08.003>.
- (118) Swanson, J.; Kittelson, D. Evaluation of Thermal Denuder and Catalytic Stripper Methods for Solid Particle Measurements. *J. Aerosol Sci.* **2010**, *41* (12), 1113–1122. <https://doi.org/10.1016/j.jaerosci.2010.09.003>.
- (119) Amanatidis, S.; Ntziachristos, L.; Giechaskiel, B.; Katsaounis, D.; Samaras, Z.; Bergmann, A. Evaluation of an Oxidation Catalyst (“Catalytic Stripper”) in Eliminating Volatile Material from Combustion Aerosol. *J. Aerosol Sci.* **2013**, *57*, 144–155. <https://doi.org/10.1016/j.jaerosci.2012.12.001>.
- (120) Cheng, Y.; He, K. B.; Duan, F. K.; Zheng, M.; Ma, Y. L.; Tan, J. H. Positive Sampling Artifact of Carbonaceous Aerosols and Its Influence on the Thermal-Optical Split of OC/EC. *Atmospheric Chem. Phys.* **2009**, *9* (18), 7243–7256. <https://doi.org/10.5194/acp-9-7243-2009>.
- (121) Binder, S.; Rastak, N.; Karg, E.; Huber, A.; Kuhn, E.; Dragan, G. C.; Monsé, C.; Breuer, D.; Di Bucchianico, S.; Delaval, M. N.; Oeder, S.; Sklorz, M.; Zimmermann, R. Construction of an In Vitro Air–Liquid Interface Exposure System to Assess the Toxicological Impact of Gas and Particle Phase of Semi-Volatile Organic Compounds. *Toxics* **2022**, *10* (12). <https://doi.org/10.3390/toxics10120730>.
- (122) Schwyn, S.; Garwin, E.; Schmidt-Ott, A. Aerosol Generation by Spark Discharge. *J. Aerosol Sci.* **1988**, *19* (5), 639–642. [https://doi.org/10.1016/0021-8502\(88\)90215-7](https://doi.org/10.1016/0021-8502(88)90215-7).
- (123) Liu, Z.; Kim, S. C.; Wang, J.; Shin, W. G.; Fissan, H.; Pui, D. Y. H. Measurement of Metal Nanoparticle Agglomerates Generated by Spark Discharge Using the Universal Nanoparticle Analyzer (UNPA). *Aerosol Sci. Technol.* **2012**, *46* (3), 333–346. <https://doi.org/10.1080/02786826.2011.626002>.
- (124) Malmborg, V. B.; Eriksson, A. C.; Török, S.; Zhang, Y.; Kling, K.; Martinsson, J.; Fortner, E. C.; Gren, L.; Kook, S.; Onasch, T. B.; Bengtsson, P.-E.; Pagels, J. Relating Aerosol Mass Spectra to Composition and Nanostructure of Soot Particles. *Carbon* **2019**, *142*, 535–546. <https://doi.org/10.1016/j.carbon.2018.10.072>.
- (125) Liu, X.; Deming, B.; Pagonis, D.; Day, D. A.; Palm, B. B.; Talukdar, R.; Roberts, J. M.; Veres, P. R.; Krechmer, J. E.; Thornton, J. A.; de Gouw, J. A.; Ziemann, P. J.; Jimenez, J. L. Effects of Gas–Wall Interactions on Measurements of Semivolatile Compounds and Small Polar Molecules. *Atmospheric Meas. Tech.* **2019**, *12* (6), 3137–3149. <https://doi.org/10.5194/amt-12-3137-2019>.
- (126) Flagan, R. C. History of Electrical Aerosol Measurements. *Aerosol Sci. Technol.* **1998**, *28* (4), 301–380. <https://doi.org/10.1080/02786829808965530>.
- (127) Cunningham, E.; Larmor, J. On the Velocity of Steady Fall of Spherical Particles through Fluid Medium. *Proc. R. Soc. Lond. Ser. Contain. Pap. Math. Phys. Character* **1997**, *83* (563), 357–365. <https://doi.org/10.1098/rspa.1910.0024>.
- (128) Bond, T. C.; Doherty, S. J.; Fahey, D. W.; Forster, P. M.; Bernsten, T.; DeAngelo, B. J.; Flanner, M. G.; Ghan, S.; Kärcher, B.; Koch, D.; Kinne, S.; Kondo, Y.; Quinn, P. K.; Sarofim, M. C.; Schultz, M. G.; Schulz, M.; Venkataraman, C.; Zhang, H.; Zhang, S.; Bellouin, N.; Guttikunda, S. K.; Hopke, P. K.; Jacobson, M. Z.; Kaiser, J. W.; Klimont, Z.; Lohmann, U.; Schwarz, J. P.; Shindell, D.; Storelvmo, T.; Warren, S. G.; Zender, C. S. Bounding the Role of Black Carbon in the Climate System: A Scientific Assessment. *J. Geophys. Res. Atmospheres* **2013**, *118* (11), 5380–5552. <https://doi.org/10.1002/jgrd.50171>.
- (129) Savadkoobi, M.; Pandolfi, M.; Favez, O.; Putaud, J.-P.; Eleftheriadis, K.; Fiebig, M.; Hopke, P. K.; Laj, P.; Wiedensohler, A.; Alados-Arboledas, L.; Bastian, S.; Chazéau, B.; María, Á. C.; Colombi, C.; Costabile, F.; Green, D. C.; Hueglin, C.; Liakakou, E.; Luoma, K.; Listrani, S.; Mihalopoulos, N.; Marchand, N.; Močnik, G.; Niemi, J. V.; Ondráček, J.;

- Petit, J.-E.; Rattigan, O. V.; Reche, C.; Timonen, H.; Titos, G.; Tremper, A. H.; Vratolis, S.; Vodička, P.; Funes, E. Y.; Zíková, N.; Harrison, R. M.; Petäjä, T.; Alastuey, A.; Querol, X. Recommendations for Reporting Equivalent Black Carbon (eBC) Mass Concentrations Based on Long-Term Pan-European in-Situ Observations. *Environ. Int.* **2024**, *185*, 108553. <https://doi.org/10.1016/j.envint.2024.108553>.
- (130) Petzold, A.; Ogren, J. A.; Fiebig, M.; Laj, P.; Li, S.-M.; Baltensperger, U.; Holzer-Popp, T.; Kinne, S.; Pappalardo, G.; Sugimoto, N.; Wehli, C.; Wiedensohler, A.; Zhang, X.-Y. Recommendations for Reporting “Black Carbon” Measurements. *Atmospheric Chem. Phys.* **2013**, *13* (16), 8365–8379. <https://doi.org/10.5194/acp-13-8365-2013>.
- (131) Ångström, A. On the Atmospheric Transmission of Sun Radiation and on Dust in the Air. *Geogr. Ann.* **1929**, *11*, 156–166.
- (132) Liu, C.; Chung, C. E.; Yin, Y.; Schnaiter, M. The Absorption Ångström Exponent of Black Carbon: From Numerical Aspects. *Atmospheric Chem. Phys.* **2018**, *18* (9), 6259–6273. <https://doi.org/10.5194/acp-18-6259-2018>.
- (133) Russell, P. B.; Bergstrom, R. W.; Shinozuka, Y.; Clarke, A. D.; DeCarlo, P. F.; Jimenez, J. L.; Livingston, J. M.; Redemann, J.; Dubovik, O.; Strawa, A. Absorption Angstrom Exponent in AERONET and Related Data as an Indicator of Aerosol Composition. *Atmospheric Chem. Phys.* **2010**, *10* (3), 1155–1169. <https://doi.org/10.5194/acp-10-1155-2010>.
- (134) Schnelle-Kreis, J.; Welthagen, W.; Sklorz, M.; Zimmermann, R. Application of Direct Thermal Desorption Gas Chromatography and Comprehensive Two-Dimensional Gas Chromatography Coupled to Time of Flight Mass Spectrometry for Analysis of Organic Compounds in Ambient Aerosol Particles. *J. Sep. Sci.* **2005**, *28* (14), 1648–1657. <https://doi.org/10.1002/jssc.200500120>.
- (135) Orasche, J.; Schnelle-Kreis, J.; Abbaszade, G.; Zimmermann, R. Technical Note: In-Situ Derivatization Thermal Desorption GC-TOFMS for Direct Analysis of Particle-Bound Non-Polar and Polar Organic Species. *Atmospheric Chem. Phys.* **2011**, *11* (17), 8977–8993. <https://doi.org/10.5194/acp-11-8977-2011>.
- (136) R'mili, B.; Le Bihan, Olivier L. C.; Dutouquet, C.; Aguerre-Charriol, O.; and Frejafon, E. Particle Sampling by TEM Grid Filtration. *Aerosol Sci. Technol.* **2013**, *47* (7), 767–775. <https://doi.org/10.1080/02786826.2013.789478>.
- (137) Offer Svenja; Hartner Elena; Di Bucchianico Sebastiano; Bisig Christoph; Bauer Stefanie; Pantzke Jana; Zimmermann Elias J.; Cao Xin; Binder Stefanie; Kuhn Evelyn; Huber Anja; Jeong Seongho; Käfer Uwe; Martens Patrick; Mesceriakovas Arunas; Bendl Jan; Brejcha Ramona; Buchholz Angela; Gat Daniella; Hohaus Thorsten; Rastak Narges; Jakobi Gert; Kalberer Markus; Kanashova Tamara; Hu Yue; Ogris Christoph; Marsico Annalisa; Theis Fabian; Pardo Michal; Gröger Thomas; Oeder Sebastian; Orasche Jürgen; Paul Andreas; Ziehm Till; Zhang Zhi-Hui; Adam Thomas; Sippula Olli; Sklorz Martin; Schnelle-Kreis Jürgen; Czech Hendryk; Kiendler-Scharr Astrid; Rudich Yinon; Zimmermann Ralf. Effect of Atmospheric Aging on Soot Particle Toxicity in Lung Cell Models at the Air–Liquid Interface: Differential Toxicological Impacts of Biogenic and Anthropogenic Secondary Organic Aerosols (SOAs). *Environ. Health Perspect.* **2023**, *130* (2), 027003. <https://doi.org/10.1289/EHP9413>.
- (138) Pardo, M.; Czech, H.; Offer, S.; Sklorz, M.; Di Bucchianico, S.; Hartner, E.; Pantzke, J.; Kuhn, E.; Paul, A.; Ziehm, T.; Zhang, Z.-H.; Jakobi, G.; Bauer, S.; Huber, A.; Zimmermann, E. J.; Rastak, N.; Binder, S.; Brejcha, R.; Schneider, E.; Orasche, J.; Rüger, C. P.; Gröger, T.; Oeder, S.; Schnelle-Kreis, J.; Hohaus, T.; Kalberer, M.; Sippula, O.; Kiendler-Scharr, A.; Zimmermann, R.; Rudich, Y. Atmospheric Aging Increases the Cytotoxicity of Bare Soot Particles in BEAS-2B Lung Cells. *Aerosol Sci. Technol.* **2023**, *57* (5), 367–383. <https://doi.org/10.1080/02786826.2023.2178878>.
- (139) Oldham, M. J.; Castro, Nicolas; Zhang, Jingjie; Rostami, Ali; Lucci, Francesco; Pithawalla, Yezdi; Kuczaj, Arkadiusz K.; Gilman, I. Gene; Kosachevsky, Pasha; Hoeng, Julia; and Lee, K. M. Deposition Efficiency and Uniformity of Monodisperse Solid Particle Deposition in the Vitrocell® 24/48 Air–Liquid-Interface in Vitro Exposure System. *Aerosol Sci. Technol.* **2020**, *54* (1), 52–65. <https://doi.org/10.1080/02786826.2019.1676877>.

- (140) Romshoo, B.; Pöhlker, M.; Wiedensohler, A.; Pfeifer, S.; Saturno, J.; Nowak, A.; Ciupek, K.; Quincey, P.; Vasilatou, K.; Ess, M. N.; Gini, M.; Eleftheriadis, K.; Robins, C.; Gaie-Levrel, F.; Müller, T. Importance of Size Representation and Morphology in Modelling Optical Properties of Black Carbon: Comparison between Laboratory Measurements and Model Simulations. *Atmospheric Meas. Tech.* **2022**, *15* (23), 6965–6989. <https://doi.org/10.5194/amt-15-6965-2022>.
- (141) Virkkula, A. Modeled Source Apportionment of Black Carbon Particles Coated with a Light-Scattering Shell. *Atmospheric Meas. Tech.* **2021**, *14* (5), 3707–3719. <https://doi.org/10.5194/amt-14-3707-2021>.
- (142) Schneider, E.; Giocastro, B.; Rüger, C. P.; Adam, T. W.; Zimmermann, R. Detection of Polycyclic Aromatic Hydrocarbons in High Organic Carbon Ultrafine Particle Extracts by Electrospray Ionization Ultrahigh-Resolution Mass Spectrometry. *J. Am. Soc. Mass Spectrom.* **2022**, *33* (11), 2019–2023. <https://doi.org/10.1021/jasms.2c00163>.
- (143) Hussar, E.; Richards, S.; Lin, Z.-Q.; Dixon, R. P.; Johnson, K. A. Human Health Risk Assessment of 16 Priority Polycyclic Aromatic Hydrocarbons in Soils of Chattanooga, Tennessee, USA. *Water, Air, Soil Pollut.* **2012**, *223* (9), 5535–5548. <https://doi.org/10.1007/s11270-012-1265-7>.
- (144) Ngo, L. D.; Duca, D.; Carpentier, Y.; Noble, J. A.; Ikhenazene, R.; Vojkovic, M.; Irimiea, C.; Ortega, I. K.; Lefevre, G.; Yon, J.; Faccinetto, A.; Therssen, E.; Ziskind, M.; Chazallon, B.; Pirim, C.; Focsa, C. Chemical Discrimination of the Particulate and Gas Phases of miniCAST Exhausts Using a Two-Filter Collection Method. *Atmospheric Meas. Tech.* **2020**, *13* (2), 951–967. <https://doi.org/10.5194/amt-13-951-2020>.
- (145) Cuesta, A.; Dhamelinourt, P.; Laureyns, J.; Martínez-Alonso, A.; Tascón, J. M. D. Raman Microprobe Studies on Carbon Materials. *Carbon* **1994**, *32* (8), 1523–1532. [https://doi.org/10.1016/0008-6223\(94\)90148-1](https://doi.org/10.1016/0008-6223(94)90148-1).
- (146) Tuinstra, F.; Koenig, J. L. Raman Spectrum of Graphite. *J. Chem. Phys.* **1970**, *53* (3), 1126–1130. <https://doi.org/10.1063/1.1674108>.
- (147) Ferrari, A. C.; Robertson, J. Interpretation of Raman Spectra of Disordered and Amorphous Carbon. *Phys. Rev. B* **2000**, *61* (20), 14095–14107. <https://doi.org/10.1103/PhysRevB.61.14095>.
- (148) Ess, M. N.; Ferry, D.; Kireeva, E. D.; Niessner, R.; Ouf, F.-X.; Ivleva, N. P. In Situ Raman Microspectroscopic Analysis of Soot Samples with Different Organic Carbon Content: Structural Changes during Heating. *Carbon* **2016**, *105*, 572–585. <https://doi.org/10.1016/j.carbon.2016.04.056>.
- (149) Vander Wal, R. L.; Yezerets, A.; Currier, N. W.; Kim, D. H.; Wang, C. M. HRTEM Study of Diesel Soot Collected from Diesel Particulate Filters. *Carbon* **2007**, *45* (1), 70–77. <https://doi.org/10.1016/j.carbon.2006.08.005>.
- (150) Vander Wal, R. L.; Tomasek, A. J. Soot Nanostructure: Dependence upon Synthesis Conditions. *Combust. Flame* **2004**, *136* (1), 129–140. <https://doi.org/10.1016/j.combustflame.2003.09.008>.
- (151) Ess, M. N.; Bertò, M.; Keller, A.; Gysel-Beer, M.; Vasilatou, K. Coated Soot Particles with Tunable, Well-Controlled Properties Generated in the Laboratory with a miniCAST BC and a Micro Smog Chamber. *J. Aerosol Sci.* **2021**, *157*, 105820. <https://doi.org/10.1016/j.jaerosci.2021.105820>.
- (152) Øvrevik, J.; Refsnes, M.; Låg, M.; Holme, J. A.; Schwarze, P. E. Activation of Proinflammatory Responses in Cells of the Airway Mucosa by Particulate Matter: Oxidant- and Non-Oxidant-Mediated Triggering Mechanisms. *Biomolecules* **2015**, *5* (3), 1399–1440. <https://doi.org/10.3390/biom5031399>.
- (153) Andreau, K.; Leroux, M.; Bouharrou, A. Health and Cellular Impacts of Air Pollutants: From Cytoprotection to Cytotoxicity. *Biochem. Res. Int.* **2012**, *2012*, 493894. <https://doi.org/10.1155/2012/493894>.
- (154) Hammond, J.; Maher, B. A.; Gonet, T.; Bautista, F.; Allsop, D. Oxidative Stress, Cytotoxic and Inflammatory Effects of Urban Ultrafine Road-Deposited Dust from the UK and Mexico in Human Epithelial Lung (Calu-3) Cells. *Antioxidants* **2022**, *11* (9). <https://doi.org/10.3390/antiox11091814>.

- (155) Salinas, M. E.; Gutiérrez, D. A.; Varela-Ramírez, A.; Garza, K. M. Continuous Exposure to Low Doses of Ultrafine Black Carbon Reduces the Vitality of Immortalized Lung-Derived Cells and Activates Senescence. *J. Toxicol.* **2020**, *2020*, 5702024. <https://doi.org/10.1155/2020/5702024>.
- (156) Bonetta, Sa.; Gianotti, V.; Bonetta, Si.; Gosetti, F.; Oddone, M.; Gennaro, M. C.; Carraro, E. DNA Damage in A549 Cells Exposed to Different Extracts of PM2.5 from Industrial, Urban and Highway Sites. *Chemosphere* **2009**, *77* (7), 1030–1034. <https://doi.org/10.1016/j.chemosphere.2009.07.076>.
- (157) Borgie, M.; Dagher, Z.; Ledoux, F.; Verdin, A.; Cazier, F.; Martin, P.; Hachimi, A.; Shirali, P.; Greige-Gerges, H.; Courcot, D. Comparison between Ultrafine and Fine Particulate Matter Collected in Lebanon: Chemical Characterization, in Vitro Cytotoxic Effects and Metabolizing Enzymes Gene Expression in Human Bronchial Epithelial Cells. *Environ. Pollut.* **2015**, *205*, 250–260. <https://doi.org/10.1016/j.envpol.2015.05.027>.
- (158) Hatzis, C.; Godleski, J. J.; González-Flecha, B.; Wolfson, J. M.; Koutrakis, P. Ambient Particulate Matter Exhibits Direct Inhibitory Effects on Oxidative Stress Enzymes. *Environ. Sci. Technol.* **2006**, *40* (8), 2805–2811. <https://doi.org/10.1021/es0518732>.
- (159) Rahman, I.; MacNee, W. Oxidative Stress and Regulation of Glutathione in Lung Inflammation. *Eur. Respir. J.* **2000**, *16* (3), 534. <https://doi.org/10.1034/j.1399-3003.2000.016003534.x>.
- (160) Tsikas, D. Assessment of Lipid Peroxidation by Measuring Malondialdehyde (MDA) and Relatives in Biological Samples: Analytical and Biological Challenges. *Lipid Methodol.* **2017**, *524*, 13–30. <https://doi.org/10.1016/j.ab.2016.10.021>.
- (161) Shimada, T.; Fujii-Kuriyama, Y. Metabolic Activation of Polycyclic Aromatic Hydrocarbons to Carcinogens by Cytochromes P450 1A1 and 1B1. *Cancer Sci.* **2004**, *95* (1), 1–6. <https://doi.org/10.1111/j.1349-7006.2004.tb03162.x>.
- (162) Wohak, L. E.; Krais, A. M.; Kucab, J. E.; Stertmann, J.; Øvrebø, S.; Seidel, A.; Phillips, D. H.; Arlt, V. M. Carcinogenic Polycyclic Aromatic Hydrocarbons Induce CYP1A1 in Human Cells via a P53-Dependent Mechanism. *Arch. Toxicol.* **2016**, *90* (2), 291–304. <https://doi.org/10.1007/s00204-014-1409-1>.
- (163) Oeder, S.; Kanashova, T.; Sippula, O.; Sapcariu, S. C.; Streibel, T.; Arteaga-Salas, J. M.; Passig, J.; Dilger, M.; Paur, H.-R.; Schlager, C.; Mülhopt, S.; Diabaté, S.; Weiss, C.; Stengel, B.; Rabe, R.; Harndorf, H.; Torvela, T.; Jokiniemi, J. K.; Hirvonen, M.-R.; Schmidt-Weber, C.; Traidl-Hoffmann, C.; BéruBé, K. A.; Włodarczyk, A. J.; Prytherch, Z.; Michalke, B.; Krebs, T.; Prévôt, A. S. H.; Kelbg, M.; Tiggesbäumker, J.; Karg, E.; Jakobi, G.; Scholtes, S.; Schnelle-Kreis, J.; Lintelmann, J.; Matuschek, G.; Sklorz, M.; Klingbeil, S.; Orasche, J.; Richthammer, P.; Müller, L.; Elsasser, M.; Reda, A.; Gröger, T.; Weggler, B.; Schwemer, T.; Czech, H.; Rüger, C. P.; Abbaszade, G.; Radischat, C.; Hiller, K.; Buters, J. T. M.; Dittmar, G.; Zimmermann, R. Particulate Matter from Both Heavy Fuel Oil and Diesel Fuel Shipping Emissions Show Strong Biological Effects on Human Lung Cells at Realistic and Comparable In Vitro Exposure Conditions. *PLOS ONE* **2015**, *10* (6), e0126536. <https://doi.org/10.1371/journal.pone.0126536>.
- (164) Andersen, M. H. G.; Saber, A. T.; Clausen, P. A.; Pedersen, J. E.; Løhr, M.; Kermanizadeh, A.; Loft, S.; Ebbenhøj, N.; Hansen, Å. M.; Pedersen, P. B.; Koponen, I. K.; Nørskov, E.-C.; Møller, P.; Vogel, U. Association between Polycyclic Aromatic Hydrocarbon Exposure and Peripheral Blood Mononuclear Cell DNA Damage in Human Volunteers during Fire Extinction Exercises. *Mutagenesis* **2018**, *33* (1), 105–115. <https://doi.org/10.1093/mutage/gex021>.
- (165) Genies, C.; Maître, A.; Lefèbvre, E.; Jullien, A.; Chopard-Lallier, M.; Douki, T. The Extreme Variety of Genotoxic Response to Benzo[a]Pyrene in Three Different Human Cell Lines from Three Different Organs. *PLOS ONE* **2013**, *8* (11), e78356. <https://doi.org/10.1371/journal.pone.0078356>.
- (166) Zimmermann, E. J.; Candeias, J.; Gawlitta, N.; Bisig, C.; Binder, S.; Pantzke, J.; Offer, S.; Rastak, N.; Bauer, S.; Huber, A.; Kuhn, E.; Buters, J.; Groeger, T.; Delaval, M. N.; Oeder, S.; Di Bucchianico, S.; Zimmermann, R. Biological Impact of Sequential Exposures to Allergens and Ultrafine Particle-Rich Combustion Aerosol on Human Bronchial

- Epithelial BEAS-2B Cells at the Air Liquid Interface. *J. Appl. Toxicol.* **2023**, *43* (8), 1225–1241. <https://doi.org/10.1002/jat.4458>.
- (167) Goedtke, L.; Sprenger, H.; Hofmann, U.; Schmidt, F. F.; Hammer, H. S.; Zanger, U. M.; Poetz, O.; Seidel, A.; Braeuning, A.; Hessel-Pras, S. Polycyclic Aromatic Hydrocarbons Activate the Aryl Hydrocarbon Receptor and the Constitutive Androstane Receptor to Regulate Xenobiotic Metabolism in Human Liver Cells. *Int. J. Mol. Sci.* **2021**, *22* (1). <https://doi.org/10.3390/ijms22010372>.
- (168) Roth, C.; Ferron, G. A.; Karg, E.; Lentner, B.; Schumann, G.; Takenaka, S.; and Heyder, J. Generation of Ultrafine Particles by Spark Discharging. *Aerosol Sci. Technol.* **2004**, *38* (3), 228–235. <https://doi.org/10.1080/02786820490247632>.
- (169) Hakkarainen, H.; Järvinen, A.; Lepistö, T.; Salo, L.; Kuittinen, N.; Laakkonen, E.; Yang, M.; Martikainen, M.-V.; Saarikoski, S.; Aurela, M.; Barreira, L.; Teinilä, K.; Ihalainen, M.; Aakko-Saksa, P.; Timonen, H.; Rönkkö, T.; Jalava, P. Toxicity of Exhaust Emissions from High Aromatic and Non-Aromatic Diesel Fuels Using in Vitro ALI Exposure System. *Sci. Total Environ.* **2023**, *890*, 164215. <https://doi.org/10.1016/j.scitotenv.2023.164215>.
- (170) Jonsdottir, H. R.; Delaval, M.; Leni, Z.; Keller, A.; Brem, B. T.; Siegerist, F.; Schönenberger, D.; Durdina, L.; Elser, M.; Burtcher, H.; Liati, A.; Geiser, M. Non-Volatile Particle Emissions from Aircraft Turbine Engines at Ground-Idle Induce Oxidative Stress in Bronchial Cells. *Commun. Biol.* **2019**, *2* (1), 90. <https://doi.org/10.1038/s42003-019-0332-7>.
- (171) Kim, B.; Shin, J. H.; Kim, H. P.; Jo, M. S.; Kim, H. S.; Lee, J. S.; Lee, H. K.; Kwon, H. C.; Han, S. G.; Kang, N.; Gulumian, M.; Bello, D.; Yu, I. J. On-Site Deployment of an Air-Liquid-Interphase Device to Assess Health Hazard Potency of Airborne Workplace Contaminants: The Case of 3-D Printers. *Front. Toxicol.* **2022**, *4*.
- (172) Das, A.; Pantzke, J.; Jeong, S.; Hartner, E.; Zimmermann, E. J.; Gawlitta, N.; Offer, S.; Shukla, D.; Huber, A.; Rastak, N.; Meščeriakovas, A.; Ivleva, N. P.; Kuhn, E.; Binder, S.; Gröger, T.; Oeder, S.; Delaval, M.; Czech, H.; Sippula, O.; Schnelle-Kreis, J.; Di Bucchianico, S.; Sklorz, M.; Zimmermann, R. Generation, Characterization, and Toxicological Assessment of Reference Ultrafine Soot Particles with Different Organic Content for Inhalation Toxicological Studies. *Sci. Total Environ.* **2024**, *951*, 175727. <https://doi.org/10.1016/j.scitotenv.2024.175727>.
- (173) Lacroix, G.; Koch, W.; Ritter, D.; Gutleb, A. C.; Larsen, S. T.; Loret, T.; Zanetti, F.; Constant, S.; Chortarea, S.; Rothen-Rutishauser, B.; Hiemstra, P. S.; Frejafon, E.; Hubert, P.; Gribaldo, L.; Kearns, P.; Aublant, J.-M.; Diabaté, S.; Weiss, C.; de Groot, A.; Kooter, I. Air–Liquid Interface In Vitro Models for Respiratory Toxicology Research: Consensus Workshop and Recommendations. *Appl. Vitro Toxicol.* **2018**, *4* (2), 91–106. <https://doi.org/10.1089/aivt.2017.0034>.
- (174) Bannuscher, A.; Schmid, O.; Drasler, B.; Rohrbasser, A.; Braakhuis, H. M.; Meldrum, K.; Zwart, E. P.; Gremmer, E. R.; Birk, B.; Rissel, M.; Landsiedel, R.; Moschini, E.; Evans, S. J.; Kumar, P.; Orak, S.; Doryab, A.; Erdem, J. S.; Serchi, T.; Vandebriel, R. J.; Cassee, F. R.; Doak, S. H.; Petri-Fink, A.; Zienolddiny, S.; Clift, M. J. D.; Rothen-Rutishauser, B. An Inter-Laboratory Effort to Harmonize the Cell-Delivered in Vitro Dose of Aerosolized Materials. *NanoImpact* **2022**, *28*, 100439. <https://doi.org/10.1016/j.impact.2022.100439>.
- (175) Neilson, L.; Mankus, C.; Thorne, D.; Jackson, G.; DeBay, J.; Meredith, C. Development of an in Vitro Cytotoxicity Model for Aerosol Exposure Using 3D Reconstructed Human Airway Tissue; Application for Assessment of e-Cigarette Aerosol. *Toxicol. In Vitro* **2015**, *29* (7), 1952–1962. <https://doi.org/10.1016/j.tiv.2015.05.018>.
- (176) Aufderheide, M.; Heller, W.-D.; Krischenowski, O.; Möhle, N.; Hochrainer, D. Improvement of the CULTEX® Exposure Technology by Radial Distribution of the Test Aerosol. *Exp. Toxicol. Pathol.* **2017**, *69* (6), 359–365. <https://doi.org/10.1016/j.etp.2017.02.004>.
- (177) Grabinski, C. M.; Hussain, S. M.; Mohan Sankaran, R. Simulations of Submicron Aerosol Deposition at an Air–Liquid Interface for in Vitro Toxicology. *J. Aerosol Sci.* **2015**, *90*, 87–102. <https://doi.org/10.1016/j.jaerosci.2015.08.005>.

- (178) Bitterle, E.; Karg, E.; Schroepel, A.; Kreyling, W. G.; Tippe, A.; Ferron, G. A.; Schmid, O.; Heyder, J.; Maier, K. L.; Hofer, T. Dose-Controlled Exposure of A549 Epithelial Cells at the Air–Liquid Interface to Airborne Ultrafine Carbonaceous Particles. *Chemosphere* **2006**, *65* (10), 1784–1790. <https://doi.org/10.1016/j.chemosphere.2006.04.035>.
- (179) Delaval, M. N.; Czech, H.; Almasaleekh, M.; Offer, S.; Ihalainen, M.; Yli-Pirilä, P.; Hohaus, T.; Kalberer, M.; Bucchianico, S. D.; Sippula, O.; Rudich, Y.; Zimmermann, R.; all members of aeroHEALTH consortium. 127 Photochemical Aging Increases Toxicity of EURO 6 Gasoline Car Exhaust in Lung Epithelial Cells at the Air-Liquid Interface. *Ann. Work Expo. Health* **2023**, *67* (Supplement_1), i69–i69. <https://doi.org/10.1093/annweh/wxac087.166>.
- (180) Loret, T.; Peyret, E.; Dubreuil, M.; Aguerre-Chariol, O.; Bressot, C.; le Bihan, O.; Amodeo, T.; Trouiller, B.; Braun, A.; Egles, C.; Lacroix, G. Air-Liquid Interface Exposure to Aerosols of Poorly Soluble Nanomaterials Induces Different Biological Activation Levels Compared to Exposure to Suspensions. *Part. Fibre Toxicol.* **2016**, *13* (1), 58. <https://doi.org/10.1186/s12989-016-0171-3>.
- (181) Zimmermann, E. J.; Das, A.; Huber, A.; Gawlitta, N.; Kuhn, E.; Schlager, C.; Gutmann, B.; Krebs, T.; Schnelle-Kreis, J.; Delaval, M. N.; Zimmermann, R. Toxicological Effects of Long-Term Continuous Exposure to Ambient Air on Human Bronchial Epithelial Calu-3 Cells Exposed at the Air-Liquid Interface. *Environ. Res.* **2025**, *269*, 120759. <https://doi.org/10.1016/j.envres.2025.120759>.

CURRICULUM VITAE

Personal Information

Date of Birth 26.08.1994
Place of Birth Guwahati (India)
Nationality Indian

Contact Details

Address Steinhauser Straße 2 81677 Munich
Email anusmita.das@uni-rostock.de

Education

08/2022- present PhD candidate
 Chair of Analytical Chemistry at the University of Rostock
 Group of Prof. Dr. Ralf Zimmermann
 07/2015- 12/2017 Master of Science (GPA: 8.24)
 Department of Environmental Science
 Tezpur University, India
 07/2012- 06/2015 Bachelor of Science (GPA: 7.3)
 Botany (Honors), Chemistry, Zoology
 Gauhati University, India

Working Experience

05/2021- present PhD researcher
 Comprehensive Molecular Analytics
 Helmholtz Munich
 07/2020- 05/2021 Guest Researcher
 Atmospheric Microphysics Department
 Leibniz Institute for Tropospheric Research
 02/2018- 12/2019 Junior Research Fellow
 Aerosol Characterization and Receptor modEling
 Indian Institute of Science Education and Research Bhopal

Munich, 13.05.2025

Anusmita Das

CONTRIBUTION TO CONFERENCES

- 1) **Das A**, Pantzke J, Hartner E, Jeong S, Jakobi G, Gröger T, Öder S, Di Bucchianico S, Sklorz M, Zimmermann R. (2022). Generation and characterization of ultrafine soot particles with similar physical but varying chemical properties, enabling differential toxicological assessment in human lung cells. 24th ETH-Conference on Combustion Generated Nanoparticles. Online. 22-24 June. Conference Talk. Recipient of the **Trojan Horse Award 2022**.
- 2) **Das A**, Pantzke J, Meščeriakovas A, Gawlitta N, Jeong S, Ivleva N, Delaval M, Schmitz-Spanke S, Di Bucchianico S, Schnelle-Kreis J, Sklorz M, Zimmermann R. (2023). Generation and Characterization of Reference Ultrafine Soot Particles to Carry Out Toxicological Assessments at the Air-Liquid Interface System. 41st Annual Conference, AAAR, Portland, USA. 02-06 October. Poster Presentation.
- 3) **Das A**, Pantzke J, Gawlitta N, Ivleva N, Meščeriakovas A, Di Bucchianico S, Schnelle-Kreis J, Sklorz M, Zimmermann R. (2024). Generation, Characterization, and Toxicological Assessment of Reference Ultrafine Particles with Different Organic Loading for Air-Liquid Interface Exposure. European Aerosol Conference, Tampere, Finland. 25-30 September. Conference Talk.
- 4) **Das A**, Delaval M, Zimmermann E.J, Huber A, Koponen H, Sippula O, Schnelle-Kreis J, Sklorz M, Zimmermann R. (2024). Determination of Ultrafine Particles Number and Mass Deposited at the Air-Liquid Interface in an *in vitro* Exposure System. European Aerosol Conference, Tampere, Finland. 25-30 September. Poster Presentation